

THE INVOLVEMENT OF STRESS IN  
URANIUM CORROSION  
PHENOMENA

A thesis submitted to The University of  
Manchester for the degree of Doctor of  
Engineering in the Faculty of Engineering  
and Physical Sciences

2015

Stephen Blaxland

School of Materials

# Contents

<b>1</b>	<b>Introduction</b>	<b>22</b>
1.1	Context . . . . .	22
1.2	Commercial application . . . . .	25
1.3	Uranium Hydride System . . . . .	26
1.4	Uranium Hydride Reaction . . . . .	34
1.5	Observations regarding sites of nucleation of UH <sub>3</sub> . . . . .	37
1.5.1	Grain boundaries . . . . .	37
1.5.2	Carbide inclusions . . . . .	40
1.6	Observations regarding dimensions and number densities of sub-surface sites . . . . .	44
1.6.1	Observations on dimensions and shape in section of sub-surface UH <sub>3</sub> . . . . .	44
1.6.2	Observations regarding observed diameters in sub-surface UH <sub>3</sub> . . . . .	48
1.6.3	Observations on the relative numbers of sub-surface UH <sub>3</sub> versus growth centres . . . . .	50
1.7	Concept . . . . .	54
1.8	Previous modelling work . . . . .	56
1.9	Zirconium hydride . . . . .	59
1.10	Project Aims . . . . .	61
<b>2</b>	<b>Nano-indentation of uranium hydride</b>	<b>63</b>
2.1	Overview of experiment . . . . .	63

2.2	Experimental procedure . . . . .	65
2.2.1	Film preparation . . . . .	65
2.2.2	X-Ray Diffraction . . . . .	71
2.2.3	Tomography . . . . .	71
2.2.4	Nano-indentation . . . . .	71
2.3	Results and discussion . . . . .	74
2.3.1	Film preparation . . . . .	74
2.3.2	XRD . . . . .	75
2.3.3	Tomography . . . . .	77
2.3.4	Nano-indentation . . . . .	78
2.4	Summary . . . . .	85
<b>3</b>	<b>Model development</b>	<b>86</b>
3.1	Modelling the oxide-layer . . . . .	86
3.1.1	Oxide stress relaxation mechanisms . . . . .	88
3.1.2	Failure of the oxide . . . . .	92
3.1.3	Summary: Modelling the oxide . . . . .	98
3.2	Modelling the uranium hydride . . . . .	99
3.2.1	Summary: Modelling the hydride . . . . .	102
3.3	Uranium metal . . . . .	102
3.3.1	Plasticity . . . . .	103
3.3.2	Summary: Modelling the uranium metal . . . . .	106
3.4	Finite Element Analysis . . . . .	106
3.5	COMSOL Calculations . . . . .	107
3.5.1	Stress calculations . . . . .	107

3.5.2	Solving double dogleg non-linear static equations	108
3.6	Construction of the Model	109
3.7	Mesh optimisation	111
3.8	Post processing Calculations	114
3.9	Simulation uncertainty	115
3.10	Modelling conditions	116
<b>4</b>	<b>Stresses induced by the nucleation of UH<sub>3</sub></b>	<b>117</b>
4.1	Modelling of stress from a nucleated hydride with isotropic material properties	117
4.2	Modelling of stress from a nucleated hydride with anisotropic material properties	122
4.3	Modelling different depths of nucleated hydrides	125
4.4	Discussion	132
4.4.1	Diffusion argument	132
4.4.2	Solubility argument	132
4.4.3	Phase change argument	133
4.4.4	Hydride development	133
4.5	Summary	135
<b>5</b>	<b>Stress induced by different shaped hydrides and multiple hydride precipitates</b>	<b>137</b>
5.1	Stress induced by different shaped hydride precipitates	138
5.2	Stress profiles of two UH <sub>3</sub> precipitates nucleated in close proximity	145

5.3	Comparison of the deformation of the oxide to AFM surface protrusion data . . . . .	151
5.4	Summary . . . . .	155
<b>6</b>	<b>Factors that could influence the hydride stress profile and the transformation into growth centres</b>	<b>157</b>
6.1	The size of the precipitate beneath the oxide surface . . . . .	157
6.2	Influence of plasticity on hydride development for different sized hydrides . . . . .	159
6.3	Influence of oxide thickness and stress on hydride transforma- tion into growth centres . . . . .	163
6.4	Influence of grain orientation on the stress profile of a hydride precipitate . . . . .	167
6.5	Work Hardened Layer . . . . .	169
6.6	Summary . . . . .	171
<b>7</b>	<b>Conclusions</b>	<b>173</b>
7.1	Nano-indentation . . . . .	173
7.2	Stresses induced by the nucleation of $\text{UH}_3$ . . . . .	173
7.3	Stress induced by different shaped hydrides and multiple hy- dride precipitates . . . . .	174
7.4	Factors that could influence the hydride stress profile and the transformation into growth centres . . . . .	175
<b>8</b>	<b>Further work recommendations</b>	<b>178</b>
8.1	Experimental . . . . .	178

8.1.1	Further nano-indentation studies on $\beta$ -UH <sub>3</sub>	178
8.1.2	Flexure bending experiment UO <sub>2</sub>	178
8.1.3	Other material properties	179
8.2	Modelling	179
8.2.1	Undulations in the metal/oxide interface	179
8.2.2	Diffusion	179
8.2.3	Inclusions and Grain boundaries	180
8.2.4	Work hardened layer	180
<b>9</b>	<b>Appendix A</b>	<b>197</b>
9.1	Materials properties sensitivity analysis	197
<b>10</b>	<b>Appendix B</b>	<b>199</b>
10.1	Weirick Simulation	199
10.2	Simulation	200
<b>11</b>	<b>Appendix C</b>	<b>201</b>
11.1	Temperature Simulations	201
11.2	Model	201
11.3	Results and discussion	202
<b>12</b>	<b>Appendix D</b>	<b>205</b>
12.1	Comparison to AFM data	205
	Word Count 39,234	

## List of Figures

1	Pourbaix diagram for uranium with hydride present [3]	23
2	Phase diagram of U-H system [8]	26
3	The solubility of hydrogen in uranium. Adapted from Powell. [9].	27
4	The $\alpha$ -UH <sub>3</sub> and $\beta$ -UH <sub>3</sub> crystallographic structures [11].	28
5	The four reaction stages in the uranium-hydrogen reaction.	34
6	Micrograph showing the precipitation and growth of UH <sub>3</sub> on U-0.1% Cr alloy (398 K, under 10 <sup>5</sup> Pa H <sub>2</sub> ). Images are at times 0, 20, 40, 60, 70 and 80 seconds [39].	36
7	Optical brightfield and polarised light micrographs of U con- taining 4 ppm H (same region). Arrows indicate precipitated UH <sub>3</sub> at the grain boundary (angular precipitates are assigned as carbides) [41].	38
8	Transmission electron microscopy image of U containing 0.5 ppm hydrogen. The white holes illustrate the positions occu- pied by hydride precipitates [45].	39
9	A carbide on the surface showing the UH <sub>3</sub> formation around the edges (mechanically polished 240°C, 525 mbar H <sub>2</sub> ) [47].	41
10	FIB image of a surface protrusion on depleted uranium surface (70°C 600-650 Torr, 60 s)[42]	45
11	FIB image of two hydride sites a) on a grain boundary b) multiple hydride sites [44]	46

12	Micrograph of a sub-surface hydride feature with failure of the over-layer [9]. . . . .	49
13	A SEM micrograph of C <sup>+</sup> implanted uranium a feature with failure of the oxide overlayer (1000 mbar 100°C H <sub>2</sub> 120 minutes) [53]. . . . .	49
14	A 15 μm diameter surface protrusion which has ruptured above the surface [9]. . . . .	50
15	Shows the evolution of the hydride sites. a) Uranium before the reaction b)The first sites c) Increase in number of the hydride sites d) Some sites continue to grow [51] (240°C 900 Torr H <sub>2</sub> ). . . . .	51
16	e the dense formation of the small hydride sites and a few growth centres that have ruptured on the Gadolinium surface [52]. . . . .	53
17	a) H <sub>2</sub> is present above U with a UO <sub>2</sub> over layer b) Hydrogen diffuses through the oxide and enters the bulk metal c) Hydrogen increases in concentration and hydride precipitates at specific sites d) Hydride precipitates grow rapidly at first but ultimately slow in their growth rate as the material around them deforms e) a small proportion of the precipitates grow to a size where the over layer fails due to the deformation: these become GCs. . . . .	55

18	The normalised elastic energy as a function of the aspect ratio of a precipitate at the free surface in hetrogenous systems. a) Hydride has a stiffness of 5% of the bulk metal b)Hydride has a stiffness of 40% of the bulk metal stiffness c) Hydride has a stiffness of 200% of the bulk metal[56] . . . . .	56
19	Greenbaum's pressure stress map of a Pd <sub>H</sub> hydride site on the free surface with an oxide-layer 40% the thickness of the hydride and anisotropic FCC material properties [57]. . . . .	58
20	Optical micrograph of the section of the hydride blister, showing the changing orientation around the blister 20. . . . .	60
21	Optical micrograph of the section of the hydride blister, showing the changing orientation around the blister[59]. . . . .	61
22	The Sn-U phase diagram [67]. . . . .	65
23	A photograph of an as-set 2 mm length uranium wire surrounded by tin with a diameter of 19 mm (Sample 10). . . . .	66
24	Photograph taken of the hydrogenation experimental set-up. The argon and hydrogen enter from the left hand side and flow through the aluminium chamber where the sample is placed. The chamber is heated by heating tape, the gas exits through the tube on the right. . . . .	67
25	Time temperature profile identical to that used for Sample 9. .	69

26	Photograph of the temperature stage used in nano-indentation experiments. The sample is placed in the centre of the base (1). The top of the stage is placed on the base forming a seal and the nano-indenter tip reaches the sample through the hole shown (2) . . . . .	72
27	Optical image of Sample 10 whilst in the nanoindenter. Area of interested is indicated. . . . .	73
28	An example of a load-displacement graph with important features highlighted. . . . .	74
29	a) x-ray diffraction pattern of Sample 9 with blue positions indicating $\beta$ -UH <sub>3</sub> and red positions indicating the Sn matrix; b) diffraction pattern collected by Bussiba et al [69]. . . . .	76
30	Tomographic image of Sample 8 with the hydrided surfaces indicated by a dotted white line. . . . .	78
31	The load-displacement graphs for the indentations (Sample 10). . . . .	79
32	Indent 2 of Sample 10. A flaw that is highlighted by the red circle . . . . .	80
33	The bulk modulus calculation with different Poisson values, values found from DFT calculations are also plotted on the graph . . . . .	83
34	Calculated stress on the oxide surface for a 64 nm oxide assuming i) isotropic growth and anisotropic growth based on anisotropic strain tensors derived from data of ii) Parise for ZrO iii) Weirick for ThO <sub>x</sub> and iv) Chernia for UO <sub>2</sub> . . . . .	91

35	The compressive yield stress of $\text{UO}_2$ against the grain size, a fitted line to the data is calculated by Rice [30]. . . . .	93
36	Schematic showing delamination as a potential failure mechanism for the oxide-layer . . . . .	94
37	Image showing delamination as a potential failure mechanism for the oxide-layer [77] . . . . .	96
38	$\text{UO}_2$ flexure failure for different grain sizes from work by Canon, Evans and Knudsen [32] [29] [88]. . . . .	97
39	An image which indicates hydride growth is isotropic a)metal b) hydride growth c)initial hydride [38] . . . . .	100
40	Anisotropic Strain Matrix . . . . .	103
41	Simplified stress strain behaviour showing the inclusion of perfect and isotropic plasticity. . . . .	104
42	Stress-strain curve for uranium [96] . . . . .	105
43	Splitting the geometry to exploit symmetry. The model was split in half at the centre as shown in (a), then the model was split in half again (b) and finally sliced down the middle in (c). . . . .	110
44	The boundary conditions on the model. . . . .	111
45	A tetrahedral mesh element, the black dots indicate the integration points. . . . .	112
46	Mesh sensitivity analysis where the maximum stress of the oxide is plotted against the number of degrees of freedom within the model. . . . .	113
47	Final mesh used in the simulations. . . . .	114

48	Images showing the pressure generated due to a $0.5 \mu\text{m}$ diameter spherical $\text{UH}_3$ nucleated at a $2 \mu\text{m}$ depth, assuming isotropic material properties. a) Cross section of the whole model; b) bird's-eye view of the oxide surface. . . . .	118
49	Images showing the pressure generated due to a $0.5 \mu\text{m}$ diameter spherical $\text{UH}_3$ nucleated at a $0.5 \mu\text{m}$ depth, assuming isotropic material properties. a) Cross section of the whole model; b) bird's-eye view of the oxide surface. . . . .	119
50	Stress map of (a) a $\text{U}/\text{UH}_3$ with no oxide, isotropic uranium properties with no plasticity and at a depth of $0.1 \mu\text{m}$ (b) semi-spherical $\text{Pd-PdH}_x$ hydride particle tangent to the free surface with no oxide, isotropic with no plasticity [57]. . . . .	121
51	Images showing the pressure generated due to a $0.5 \mu\text{m}$ diameter spherical $\text{UH}_3$ nucleated at a $2 \mu\text{m}$ depth, assuming anisotropic material properties. a) Cross section of the whole model; b) bird's-eye view of the oxide surface. . . . .	123
52	Images showing the pressure generated due to a $0.5 \mu\text{m}$ diameter spherical $\text{UH}_3$ nucleated at a $0.5 \mu\text{m}$ depth, assuming anisotropic material properties. a) Cross section of the whole model; b) bird's-eye view of the oxide surface. . . . .	124
53	Image showing the tensile region generated due to a $0.5 \mu\text{m}$ diameter spherical $\text{UH}_3$ nucleated at a $2 \mu\text{m}$ depth, assuming anisotropic material properties. . . . .	125

54	The pressure within the oxide-layer taken from the centre of the simulation to a distance of 3 $\mu\text{m}$ in the x direction for precipitate depths of 0 $\mu\text{m}$ , 0.25 $\mu\text{m}$ , 0.5 $\mu\text{m}$ , 1 $\mu\text{m}$ , 1.5 $\mu\text{m}$ and 2 $\mu\text{m}$ . . . . .	126
55	The deformation of the oxide-layer taken from the centre of the hydride to a distance of 3 $\mu\text{m}$ in the x direction for various depths in $\mu\text{m}$ . Positions of peak oxide tensile stress are indicated.	129
56	The total energy and the total elastic strain energy density plotted against the depth of the $\text{UH}_3$ precipitate. . . . .	130
57	The displacement of the uranium bulk for depths of a) 2 $\mu\text{m}$ b) 1 $\mu\text{m}$ and c) 0.5 $\mu\text{m}$ . The colours indicate the displacement of the material occurring with red indicating the largest amount of displacement . . . . .	131
58	The possible growth mechanism for an initial hydride nucleation site. The hydride grows upwards and to the sides with the possibility of forming streamers below. . . . .	134
59	The different dimensions of an ellipsoidal hydride precipitate with (A) representing the height and (B) the width. . . . .	138
60	Images showing the pressure generated due to $\text{UH}_3$ nucleated at a 2 $\mu\text{m}$ depth, assuming isotropic material properties:a) cross section of the whole model; b) bird's-eye view of the oxide surface. . . . .	139
61	The percentage change in TESE from the normalised TESE value (when spherical) against the A:B ratio of the hydride. Greenbaums work [56] is compared to work for this thesis. . .	142

62	The percentage change in total energy from the normalised total energy value (when spherical) against the A:B ratio of the hydride. Greenbaums work [56] is compared to work for this thesis. . . . .	144
63	Three stress maps of two sub-surface precipitates at distances of a) 1.5 $\mu\text{m}$ b) 2.5 $\mu\text{m}$ and 3.5) $\mu\text{m}$ . . . . .	147
64	The pressure on the surface for different distances between two hydrides at a depth of 0.5 $\mu\text{m}$ . . . . .	148
65	The total energy for different distances between two hydrides at a depth of 0.5 $\mu\text{m}$ for a) 0.5 diameter circular and b) 1:2 ellipse with the same area. . . . .	149
66	Two AFM images, the dotted lines indicate the line the AFM data was taken from. On the left are surface protrusions #1 and #2 which are 3.5 $\mu\text{m}$ apart and on the right are surface protrusions #3 and #4 which are 5.1 $\mu\text{m}$ apart [15]. . . . .	152
67	A two dimensional profile of two hydride sites from a) AFM sites and b) simulated results of two spherical hydrides at a depth of 0.5 $\mu\text{m}$ . . . . .	154
68	The deformation of the oxide surface for $\text{UH}_3$ precipitates of diameter 0.08, 0.2, 0.5 and 0.8 $\mu\text{m}$ , the depth of the hydride is kept constant at 0.5 $\mu\text{m}$ . . . . .	158
69	Plastically deformed regions surrounding the $\text{UH}_3$ precipitate are shown with the colours representing the amount of effective plastic strain. Precipitate diameter a)0.08 $\mu\text{m}$ b)0.2 $\mu\text{m}$ c)0.5 $\mu\text{m}$ at a depth of 0.5 $\mu\text{m}$ . . . . .	160

70	Plastic dissipation per unit volume for the different diameter precipitates. . . . .	162
71	The minimum stress within the oxide-layer for a sub-surface hydride diameter 0.5 and 0.8 $\mu\text{m}$ at a depth of 0.5 $\mu\text{m}$ as a function of the oxide layer thickness. . . . .	164
72	The minimum tensile stress within the oxide-layer for a 0.5 $\mu\text{m}$ hydride plotted against the compressive stress of the oxide for a thickness of 64 nm. . . . .	166
73	An inverse pole map of $\alpha$ -U grain orientation with preferential [001] orientation [102]. . . . .	167
74	Image on the left the [010] $\alpha$ -U grain orientation and on the right is the [100] orientation a) Cross section of the whole model; b) bird's-eye view of the oxide surface. . . . .	168
75	The total energy of the system was plotted against the % change in the yield stress on the work hardened layer. . . . .	170
76	Sensitivity analysis of the six material properties that will be used for the simulations. . . . .	198
77	The experimental material dimensions used by Weirick. . . . .	199
78	Temperature variation of the hydride/metal over 3 seconds . .	203
79	A mesh plot of the AFM data, two surface protrusions can be seen . . . . .	205
80	Comparison of the model results with experimental AFM results. . . . .	206

## List of Tables

1	Uranium Material Properties . . . . .	30
2	Uranium Material Properties . . . . .	33
3	Observations from different hydriding experiments showing the variation in material, preparation and hydrogen induc- tion and if the work has substantially linked hydrides to grain boundaries or inclusions. . . . .	43
4	Comparison of surface protrusion size and shape. . . . .	48
5	Hydride site density for small sites and for growth centres . .	53
6	Temperature and hydrogen flow rated for the hydriding pro- cedure . . . . .	70
7	Nanoindentation results . . . . .	81
8	Mesh Element Properties . . . . .	114
9	Deformation and total energy for different grain orientations .	169

## Abstract

Sub-surface precipitations of  $\text{UH}_3$  have been modelled with Finite Element methods. The model includes a pre-stressed oxide layer, metal anisotropy, metal plasticity and a hyper elastic coherent hydride. The model was used to investigate  $\text{UH}_3$  precipitating at a variety of depths from 0 to  $2\mu\text{m}$  (spherical shape), with a variety of sizes from  $0.08$  to  $0.8\mu\text{m}$  diameter (spherical shape) and with a variety of shapes from horizontal ellipsoid to vertical ellipsoid (depth  $0.5\mu\text{m}$ ).

$\text{UH}_3$  precipitation close to the surface was found to be energetically favourable as observed in experiments. Simulations on the shape of the precipitate found that the vertical ellipsoidal precipitates were found to be energetically favoured in contrast to what has been experimentally observed. In all cases the system could not accommodate the phase change by elastic deformation alone but by a combination of elastic and plastic deformation.

When anisotropy is introduced into the metal matrix, the precipitate is surrounded by compressive and tensile regions. Tensile regions are found in the x-y plane adjacent to the precipitate and it is suggested that these regions are more likely to transform into further  $\text{UH}_3$  (through increased hydrogen diffusion, solubility or ease of phase change). Such precipitate development in the lateral direction would result in the experimentally observed horizontal ellipsoids.

Multiple sub-surface precipitates were simulated ( $0.5\mu\text{m}$  depth) and it is suggested that compressive regions that develop between the precipitates could act as a barrier to coalescence. The surrounding stress regions and energetic factors suggest that there is a barrier to amalgamation for a distance of  $1.5\mu\text{m}$ . Whereas for precipitates closer than  $1.5\mu\text{m}$  there is an energetic benefit to coalescence. The transformation from sub-surface  $\text{UH}_3$  precipitates into growth centres (exposed  $\text{UH}_3$  on the surface) was examined by monitoring the oxide stress. This work also suggests that the transformation of sub-surface  $\text{UH}_3$  to growth centres could be retarded by an increased oxide thickness and the presence of a work hardened layer.

To aid confidence in the model nano-indentation experiments were carried out on constrained  $\text{UH}_3$  surface films in the absence of air. Collected data shows a bulk modulus of  $180 +/- \text{GPa}$  which is more in line with DFT calculated results as compared to Diamond Anvil Cell experimental work. The nano-indentation work represents the first time this type of data has been derived for  $\text{UH}_3$  in this way.

## **Declaration**

No portion of the work referred to in this thesis has been submitted in support or an application for another degree or qualification of this or any other university or other institute of learning.

## Copyright Statement

COPYRIGHT STATEMENT The following four notes on copyright and the ownership of intellectual property rights must be included as written below:

- The author of this thesis (including any appendices and/or schedules to this thesis) owns certain copyright or related rights in it (the Copyright) and s/he has given The University of Manchester certain rights to use such Copyright, including for administrative purposes.
- Copies of this thesis, either in full or in extracts and whether in hard or electronic copy, may be made only in accordance with the Copyright, Designs and Patents Act 1988 (as amended) and regulations issued under it or, where appropriate, in accordance with licensing agreements which the University has from time to time. This page must form part of any such copies made.
- The ownership of certain Copyright, patents, designs, trade marks and other intellectual property (the Intellectual Property) and any reproductions of copyright works in the thesis, for example graphs and tables (Reproductions), which may be described in this thesis, may not be owned by the author and may be owned by third parties. Such Intellectual Property and Reproductions cannot and must not be made available for use without the prior written permission of the owner(s) of the relevant Intellectual Property and/or Reproductions.
- Further information on the conditions under which disclosure, publication and commercialisation of this thesis, the Copyright and any Intellectual Property and/or Reproductions described in it may take place is available in the University IP Policy (see <http://documents.manchester.ac.uk/DocuInfo.aspx?DocID=487>), in any relevant Thesis restriction declarations deposited in the University Library, The University Library's regulations (see <http://www.manchester.ac.uk/library/aboutus/regulations>) and in The University's policy on Presentation of Theses.

## Acknowledgements

First I would like to acknowledge my supervisors Robert Harker, Nick Stevens and Andrew Willets who have been diligent and helpful throughout the project.

I would also like to thank the AWE and specially to their employees who have been incredibly helpful with particular mention to Wayne Lake, James Petherbridge, Phil Monks, Mark Storr, Dave Wheeler and Giles Aldrich-Smith.

I would like to thank the many people that have helped me at the University of Manchester. Among these Steve Blatch, Gary Harrison and Andrew Forrest, through many hour of work managed to successfully traverse the obstacles of working with radioactive material.

I am also very grateful to the EPSRC for giving me this brilliant opportunity and funding to complete this EngD. With a special mention to David Stanley who has constantly been supportive throughout.

Also I would like to thank all of the people in A11 who have helped me along the way and kept me calm all these years.

I would finally like to personally thank my family, especially my mum, and fiance Lizzie. With their constant support and encouragement over the last four years, with many ups and downs, helped made it the best of my life.

## Abbreviations

AFM = Atomic Force Microscope

AWE = Atomic Weapons Establishment

DFT = Density functional theory

EBSD = Electron backscatter diffraction

FE = Finite element

FIB = Focused ion beam

GC = Growth centre

LANL = Los Alamos National Lab

LDA = Local-density approximation

LDA+U = Local-density approximation + U-value

NMR = Nuclear Magnetic Resonance

PBR = Pitting Bedworth Ratio

RT = Room Temperature

SEM = Scanning electron microscope

SIM = Secondary Ion Mass spectrometry

SPL = Surface Passivation Layer

TEM = Transmission electron microscopy

TESE = Total Elastic Strain Energy

XRD= X-Ray Diffraction

# 1 Introduction

## 1.1 Context

Engineered uranium metal components are widely used within the nuclear industry, primarily in pellet form to fuel nuclear reactors. To ensure optimum performance and safety, the structural integrity of these parts must be maintained. This integrity can be compromised by a variety of corrosion mechanisms which can occur throughout the life cycle of the component.

The corrosion of uranium is of particular interest to the UK industry as uranium has been of significant importance since the start of the nuclear industry. The material was often stored in old outdated facilities, with the main example of this at Sellafield. The study of the corrosion mechanisms of uranium will allow a greater understanding of the legacy waste, enabling a safer and more comprehensive programme of decommissioning. Furthermore, the nuclear industry can learn from a greater understanding of the corrosion processes leading to safer storage. This is especially important since corrosion of waste within a geological repository is a key research and development topic for the nuclear decommissioning authority [1].

Important to the nuclear industry and especially to Sellafield is the aqueous corrosion of uranium. The chemical thermodynamics have been extensively reviewed by Grenthe et al in 1992 [2] and the complexity is shown in the eh-ph diagram created by Lyons et al in Figure 1 [3].

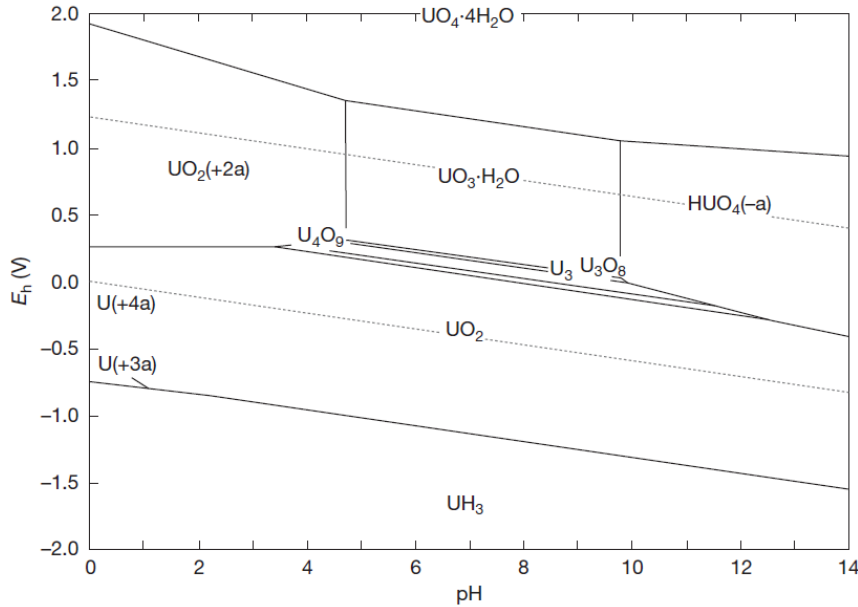


Figure 1: Pourbaix diagram for uranium with hydride present [3]

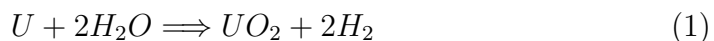
The formation of  $\text{UO}_2$  creates a region of passivity through a highly exothermic reaction which has an enthalpy of reaction of -513.2 kcal/mole of uranium [4]. This  $\text{UO}_2$  layer though is not protective and continues to react at both low and high pH, furthermore the oxide layer spalls easily encouraging further corrosion. The inclusion of  $\text{UH}_3$  (shown in Figure 2 is also found to be stable although the reaction is exothermic in humid air.

This reaction of uranium with hydrogen is a particularly damaging corrosion mechanism for uranium as is often referred to as the hydriding reaction. The reaction is localised, in the form of pitting, which can cause the bulk metal to fracture and spall. The reaction itself is exothermic and produces a pyrophoric [5], toxic corrosion product that can often be loose, these properties make hydrogen corroded uranium difficult to handle. Further to this,

even if the metal is still intact, the dissolved hydrogen can modify material properties through embrittlement and stress corrosion cracking.

The U-H<sub>2</sub> reaction has been studied for many years and there has been important advances in understanding, but it is still very difficult to predict where the corrosion starts, when the corrosion starts and how much uranium hydride will be produced over time. The degradation mechanism itself is also of interest in its own right as a model metal-hydrogen system since there is a low solubility of hydrogen in the metal and only stoichiometric UH<sub>3</sub> is formed.

During storage of uranium, H<sub>2</sub> can be produced by radiolytic ageing of hydrogen containing materials, such as polymers, greases, oils as well as through chemical reactions of materials in contact with the uranium. For example, cement is used to encapsulate uranium, and water is one of cement's principle components [6]. This can be a problem since uranium is capable of reducing water present in the gaseous atmosphere through Equation 1.



This reaction creates an oxide-layer on the uranium surface and surface hydrogen, some of this hydrogen combines to form gaseous H<sub>2</sub> whilst another portion migrates into the metal. The gaseous H<sub>2</sub> generated from the reaction in Equation 1 will eventually build up to a measurable pressure before reacting further with U to produce UH<sub>3</sub> as seen in Equation 2.



The mechanism of corrosion that will be considered in this thesis is the direct reaction of uranium and hydrogen. Specifically, the study is interested in conditions that relate to storage which are close to room temperature and partial pressures of H<sub>2</sub> in the mbar region. Relevant data is available from recent work at AWE (Atomic Weapons Establishment) undertaken at 80°C and 10 mbar H<sub>2</sub> and it is this temperature that will be focussed on in this research.

## 1.2 Commercial application

This EngD project was launched in collaboration with the Atomic Weapons Establishment in Aldermaston, Reading. This work has focused on the examination of the role stress has in the nucleation and growth mechanisms of uranium hydride within bulk uranium. The core focus of this project is to build models that AWE can use to increase their understanding on stress levels both within uranium and at the oxide surface. With the focus on three main aims:

- What are the stresses induced by the nucleation of UH<sub>3</sub>?
- Does stress effect the shape of the hydrides?
- Why do some hydrides transform into growth centres?

The results and models from this work could be used within larger models to understand and simulate corrosion damage of long term stored uranium. This will help the nuclear industry to understand how to store uranium effectively and to predict the corrosion damage caused to uranium from hydrogen.

### 1.3 Uranium Hydride System

Uranium is a silver coloured metal which has three distinct crystalline phases  $\alpha$  ( $< 666^\circ\text{C}$ ),  $\beta$  ( $666\text{-}774^\circ\text{C}$ ) and  $\gamma$  ( $774\text{-}1133^\circ\text{C}$ ) [7]. The phase that shall be examined in this study is the most common phase encountered during storage conditions and this is the  $\alpha$  phase which has an orthorhombic crystal structure ( $a=2.854$ ;  $b=5.865$ ;  $c=4.955$ ) [7]. This structure adds extra complexity since it means the uranium exhibits anisotropic material properties.

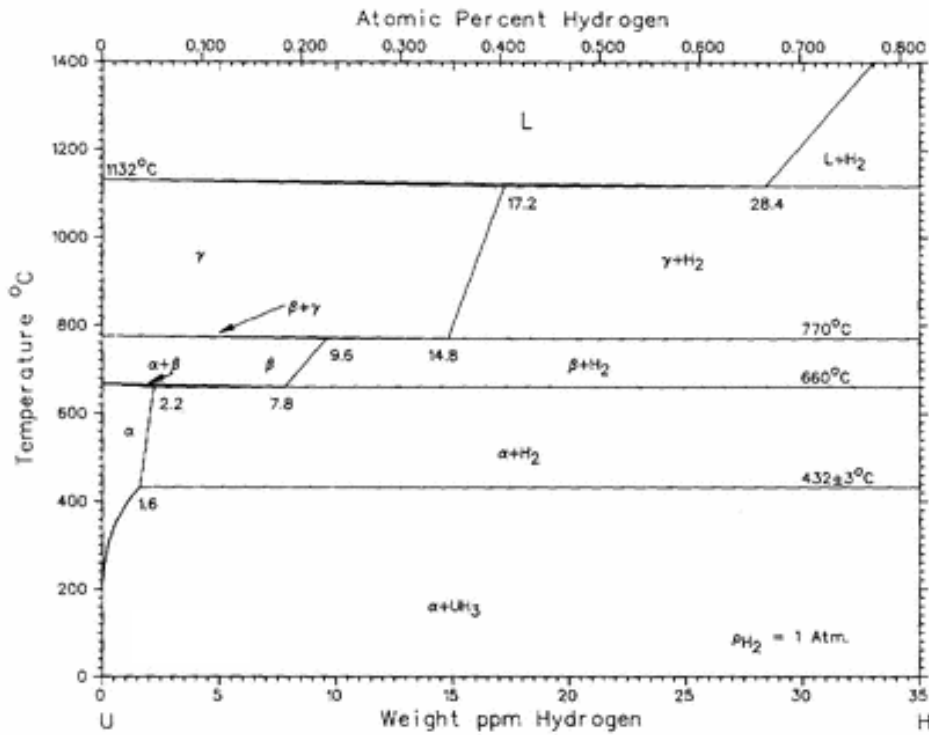


Figure 2: Phase diagram of U-H system [8]

The phase diagram of the U-H system (Figure 2) shows that at lower temperatures only a very small amount of hydrogen can be dissolved in  $\alpha$ -U.

Above this solubility level the system will exist as a two-phase  $\alpha$ -U + UH<sub>3</sub> system with the UH<sub>3</sub> coexisting in the  $\alpha$ -U matrix.

Powell [9] recently reviewed the solubility limit of hydrogen in uranium and his data can be seen below in Figure 3.

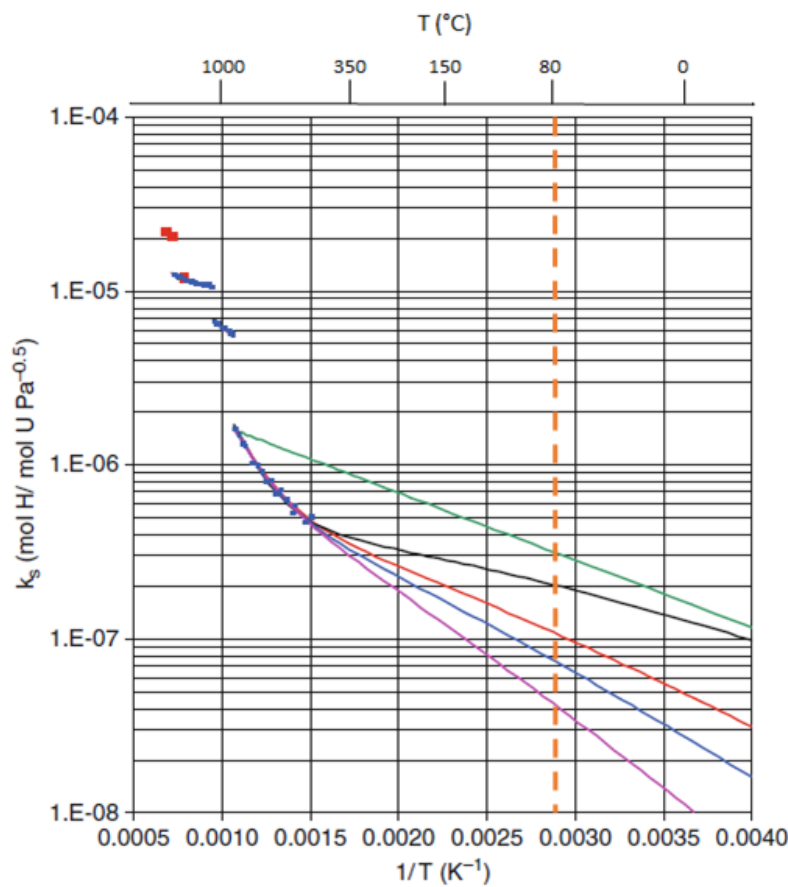


Figure 3: The solubility of hydrogen in uranium. Adapted from Powell. [9].

The blue points on the graph indicate solubility measurements undertaken at Y-12 national security complex [7]. Using this data Powell fitted these points to the bound proton model shown in Equation 3,

$$k_s = \frac{A(1 + Be^{-C/T})/(1 - e^{-1680/T})^3 e^{(E-25997.5)T}}{0.02072T^{-1.75}/(1 - e^{-5986/T})^{0.5}} \quad (3)$$

where  $k_s$  is the solubility and A, B, C and E are parameters. Each coloured line indicates a different set of parameters and each line fits the experimental data, however, when approaching room temperature there is a large uncertainty in the solubility. The specific temperature of interest is related to the experimental conditions described earlier of 353K (80°C) which is indicated on the graph and is between  $3.92e^{-08}$  and  $3.01e^{-07}$  molH/molU Pa $^{-0.5}$ [7].

Uranium hydride itself was first reported to have been discovered by Driggs in 1929 [10] and has two distinct stoichiometric UH<sub>3</sub> cubic phases  $\alpha$  and  $\beta$ . The structure of these two phases can be seen below in Figure 4 [11]:

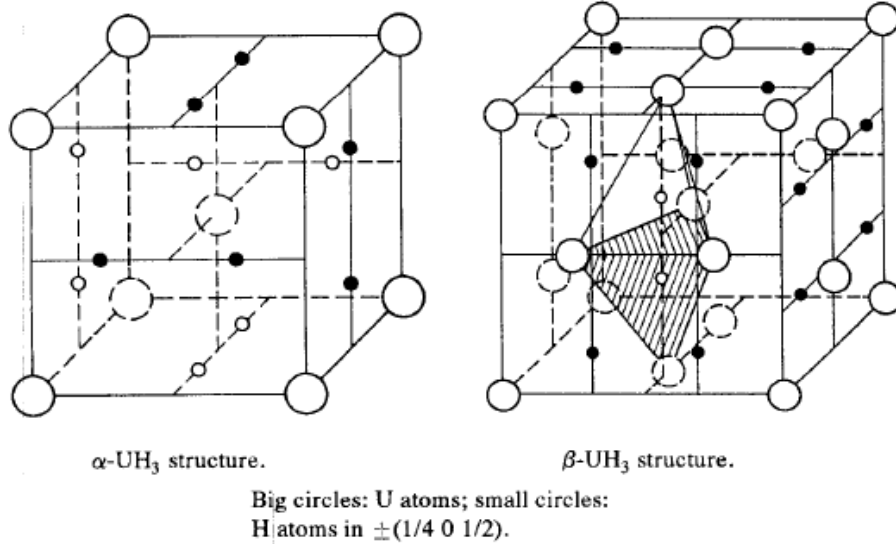


Figure 4: The  $\alpha\text{-UH}_3$  and  $\beta\text{-UH}_3$  crystallographic structures [11].

The  $\alpha$ -UH<sub>3</sub> phase is difficult to form exclusively and is often formed as a mixture with  $\beta$ -UH<sub>3</sub> as noted by Abraham and Flotow [12]. These workers report that only a small amount of heat of transition is required to transform  $\alpha$  to  $\beta$  [12]. The alpha phase has therefore been postulated to be a metastable phase between the orthorhombic uranium phase and the  $\beta$ -UH<sub>3</sub> phase, with a greater concentration of  $\alpha$ -UH<sub>3</sub> formed at lower reaction temperatures. Taylor [13] argued that the alpha phase has a lower moduli and therefore will form more readily within the metal under high compression since less energy is required to form it. Taylor's work complemented previous work by Condon [14] who argued that the symmetry of the  $\alpha$ -phase means that it is intermediate before the stable beta phase.

This work attempts to model the U-UH<sub>3</sub> system under conditions that were used in experimental studies at 80°C [15]. Within those studies it was shown that  $\beta$ -UH<sub>3</sub> was the only positively identified UH<sub>3</sub> compound formed. For this reason the modelling work will focus on the formation of  $\beta$ -UH<sub>3</sub>.

Material properties are of particular importance for the accuracy of simulations in the future models. Therefore, a comprehensive list of the material properties for uranium, uranium dioxide and uranium hydride were collated from different sources and this data can be seen in Table 1. To simplify the model this work has used materials properties for as-cast uranium metal, stoichiometric UO<sub>2.0</sub> and  $\beta$ -UH<sub>3</sub>.

Table 1: Uranium Material Properties

Material Properties	U	UO <sub>2</sub>	$\beta$ -UH <sub>3</sub>
Bulk Modulus (GPa)	101.4 [16]	213.0 [17]	33 [18]
	121.3 [16]	183.4 [19]	144 [13]
	97.9 [20]	203.2 [21]	120 [22]
	111.5 [23]	209.0 [24]	128 [22]
	114 [25]		
Shear Modulus (GPa)	83.4 [16]	87.0 [17]	60 [13]
	77.9 [24]	75.0 [19]	58 [22]
	83.4 [20]	82.1 [21]	
	80.6 [23]	83.0 [24]	
	69.1 [25]		
	75.8 [16]		
Young's Modulus (GPa)	184.8 [16]	231.0 [17]	163 [22]
	205.4 [16]	204.7 [19]	146 [22]
	190 [24]	217.2 [21]	158 [26]
	203.3 [20]	221.0 [24]	
	195.1 [23]	214.0 [27]	
	172 [25]		
Poisson Ratio	0.19 [25]	0.319 [17]	0.317 [13]
	0.23 [25]	0.314 [19]	0.3 [22]
	0.220 [24]	0.323 [21]	
	0.22 [20]	0.324 [24]	
	0.2087 [23]		
	0.247 [25]		

There are two ways you can simulate stress in mechanical models, these two ways use four parameters which are interrelated, for example you can use the bulk modulus with the shear modulus or you can use the Young's modulus with the Poisson ratio. Early work in the project not included here tested the viability of the two methods and they gave similar results. However, as the bulk modulus was the only parameter with experimental data for  $\beta$ -UH<sub>3</sub> it was decided to continue the rest of the project with that parameter pair (bulk modulus and shear modulus). In addition to this approach the project looked

at ways to generate additional experimental data for the elastic moduli of  $\beta$ -UH<sub>3</sub> (see Section 2).

For the project has we have used the average of the values found for the bulk modulus and the shear modulus as shown in Table 1; these being 109 GPa and 78 GPa. For the uranium dioxide a similar approach has been taken and the average numbers these numbers are; 202 GPa and 82 GPa. For the uranium hydride only one value was available for the shear modulus during the early stages of the project this was by Taylor [13] at 60 GPa and this has been used throughout.

For bulk modulus properties of  $\beta$ -UH<sub>3</sub> at the start of the project two values existed in the literature. Halevy [18] studied the change in unit cell parameter in  $\beta$ -UH<sub>3</sub> in a diamond anvil cell (over 0-29 GPa pressure and at 300°C) and then he extracted from this data the bulk modulus to be 33±5 GPa. More recently Taylor [13] carried out DFT calculations (Density Functional Theory) and he calculated it to be 144 GPa. Whilst this project was ongoing Zhang [22] used DFT methods to calculate the bulk modulus to be 128 GPa and 120 GPa, the difference being due to different computational methods LDA (Local-density approximation) and LDA+U (Local-density approximation + U-value) respectivel). Early stages of the work described in this thesis used an average of the Halevy and Taylor number for the bulk Modulus (89 GPa) and this is used for the work in all of the Appendices. However, experimental work as described in Section 2 has suggested a higher number for bulk modulus than 89 GPa and this along with new modelling results by Zhang has led to more confidence in Taylor's assessment: therefore 144 GPa was used for UH<sub>3</sub> bulk modulus in Sections 3-6.

A sensitivity analysis was carried out in early work and this is detailed in Appendix A. This work showed that the uncertainty in the bulk modulus of the hydride varies the stress calculation at a given point of the model perhaps by as much as 35% stress for a 50% change in bulk modulus. As can be seen the uncertainty in bulk modulus when considering only the Halevy and Taylor work ( $89 \pm 60\%$ ) suggests a considerable uncertainty in calculated stress on account of this single parameter. The next most influential parameters are the shear modulus of the metal (22%) and hydride (12%) respectively for a 50% change in parameter. In both these cases the literature values are in closer agreement (within  $\pm 20\% \pm 3\%$ ). These uncertainties correspond to an uncertainty in stress of only 7.5% and 1% respectively.

Further material properties are needed when the anisotropy and plasticity of the metal are included; these have been collated and can be seen in Table 2. The first of these properties is the yield strength, which is the point when the material starts to deform plastically. The yield strength of  $\alpha$  uranium has been measured by different authors and three similar results have been found, therefore an average of these results shall be used in these models of 230 GPa. Since the uranium metal is anisotropic the elastic constants shall be used in an anisotropic matrix to simulate the metal deformation.

At lower temperatures (below 800°C) it is expected from the work of Shunk [28] that when UO<sub>2</sub> reaches a yield stress no plastic deformation takes place and the UO<sub>2</sub> fractures. There are a few articles which have concluded the yield stress of uranium dioxide. Evans [29] showed there could be a variation of between 105-1200 MPa in tension. Whilst in compression [30] it could be up to 20 GPa if the data is extrapolated from large to small grain

size, however, this value is extremely high and this is examined in more detail in Section 3. It is assumed in this work that the failure point of the oxide is only in tension and a value of 105 MPa or 1.1 GPa was used. All of these effects shall be discussed in more detail in Section 3.

For  $\beta\text{-UH}_3$  there are no known yield stresses so it was assumed for simplicity that the hydride does not fail during nucleation. For the system modelled here:  $\beta\text{-UH}_3$  contained under a  $\text{UO}_2$  or  $\text{UO}_2/\text{U}$  over layer this is a fair assumption

Table 2: Uranium Material Properties

Material Properties	U	$\text{UO}_2$	$\beta\text{-UH}_3$
Yield Stress Tension(MPa)	280 [31] 206.8 [16] 200 [24]	105 [32] 180 [29]	1200*
Yield Stress Compression(MPa)	N/A	20000* [30] 820 [33]	
Elastic Constants (GPa)	$C_{11}$ 214 [23] $C_{12}$ 46 [23] $C_{13}$ 22 [23] $C_{22}$ 198 [23] $C_{23}$ 107 [23] $C_{33}$ 267 [23] $C_{44}$ 124 [23] $C_{55}$ 73 [23] $C_{66}$ 74 [23]	$C_{11}$ 401 [34] $C_{11}$ 396 [17] $C_{11}$ 389.3 [24] $C_{12}$ 92 [22] $C_{12}$ 70 [22] $C_{12}$ 102 [13] $C_{44}$ 58 [22] $C_{44}$ 57 [22] $C_{44}$ 60 [13]	$C_{11}$ 222 [22] $C_{11}$ 201 [22] $C_{11}$ 227 [13] $C_{12}$ 92 [22] $C_{12}$ 70 [22] $C_{12}$ 102 [13] $C_{44}$ 58 [22] $C_{44}$ 57 [22] $C_{44}$ 60 [13]
Density ( $\text{gcm}^{-3}$ )	19.1	10.97	10.91

\* This value is extrapolated from large grain size to the grain size in this work, more detail can be found in Section 3.2.

## 1.4 Uranium Hydride Reaction

For a hypothetical reaction of uranium with an excess of hydrogen gas the reaction has been described in terms of four reaction stages (Figure 5). Each stage shall be briefly described below.

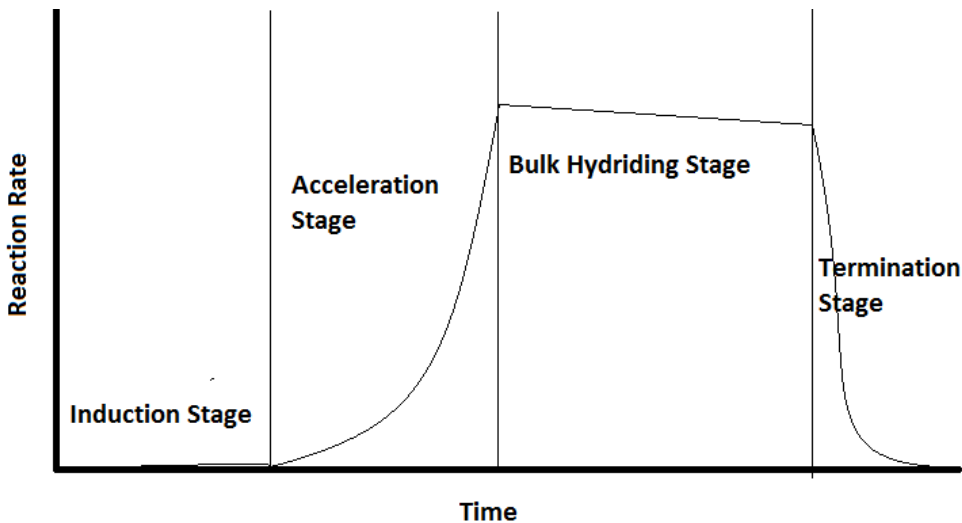


Figure 5: The four reaction stages in the uranium-hydrogen reaction.

The first stage of the reaction is the induction stage. In this stage, the hydrogen first diffuses through the oxide-layer which is thought by many to form a barrier to the hydrogen [35] [36] [37]. Some researchers (for example Bloch and Mintz and co-workers) refer to a Surface Passivation Layer (SPL), by which they mean both the oxide and additional chemical contamination and inclusions that would influence its hydrogen barrier properties [38]. Once the hydrogen diffuses through the oxide-layer, it nucleates at discrete points forming  $\text{UH}_3$ . The identity of precipitation points is the matter of some debate and will be discussed further in this section. Similarly, the depth

of nucleation, whether at the U/UO<sub>2</sub> interface or below it is still a topic of discussion.

The site of formation of the UH<sub>3</sub> plays an important role in determining the stresses within the system, and is probably also important to the hydride growth. This phase has often been linked to the development of sub-surface sites that are observed on the surface as protrusions. The fact that the nucleation occurs below the surface means that it is not directly observable and is most often inferred with post reaction sectioning and microscopy techniques.

The next, acceleration phase, is observed as the stage where H<sub>2</sub> consumption dramatically increases. This increase in the quantity of hydrogen consumed is dominated by an increasing number of hemispherical open attack sites (Growth Centres) on the sample all growing at a linear rate. Figure 6 illustrates this well, it shows that many precipitate sites are evenly spread out over the uranium metal: with a proportion of them becoming Growth Centre's (GCs). These growth centres continue to increase in size at a linear rate. The acceleration phase ends when the entire surface of the uranium is covered in a layer of hydride and after this point the overall H<sub>2</sub> consumption rate enters an approximately linear phase.

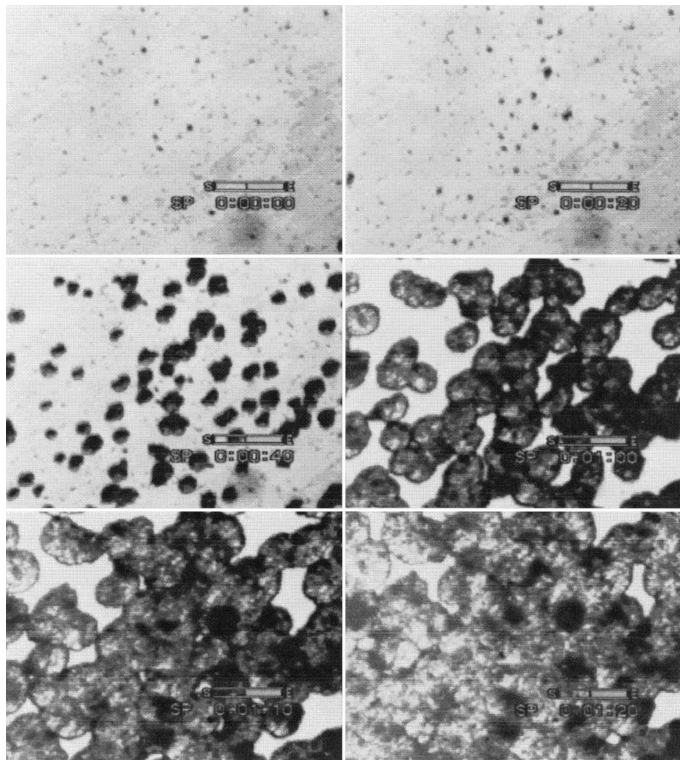


Figure 6: Micrograph showing the precipitation and growth of UH<sub>3</sub> on U-0.1% Cr alloy (398 K, under 10<sup>5</sup> Pa H<sub>2</sub>). Images are at times 0, 20, 40, 60, 70 and 80 seconds [39].

Once the entire surface of the uranium is enclosed with UH<sub>3</sub> the acceleration phase ends and the final bulk hydriding phase occurs. The hydride reaction front then reacts with the U-UH<sub>3</sub> interface , and this has been called the 'contracting envelope morphology' [40]. This front moves at constant velocity related to the speed at which the hydrogen can diffuse through the adherent UH<sub>3</sub> layer. The slow reduction in overall rate during this phase is due to a slow reduction in the available surface area of uranium.

The final stage of the hydriding process is the termination stage. This stage occurs when the available uranium with which to react (and its surface

are) is decreasing. This causes the reaction rate to decrease rapidly until there is no more unreacted uranium left.

This thesis is specifically interested in the induction stage of the reaction and the point the reaction undergoes a transition from induction to acceleration phases.

## 1.5 Observations regarding sites of nucleation of $\text{UH}_3$

A number of studies have attempted to understand the identity of hydride nucleation sites. These studies have differentiated between large scale observable defects (grain boundaries, inclusions) as compared to difficult to observe defects (dislocations, atomic scale impurities, vacancies). It should be noted that some have modelled this second category [13] [26] but experimental data is scarce.

### 1.5.1 Grain boundaries

There have been a number of studies investigating whether  $\text{UH}_3$  forms preferentially at grain boundaries. Beevers [41] introduced hydrogen into uranium wire at 540-800°C and 70-760 Torr  $\text{H}_2$  over 30 minutes then quenched in silicon oil to provide a range of hydrogen concentrations. With TEM (Transmission electron microscopy) and optical microscopy the study reports that "in specimens containing 2.5-15 ppm the hydride precipitates were always observed to be associated with grain boundaries." An example is shown in Figure 7 for a 4 ppm sample (30 min 695°C, 160 Torr and quenched).

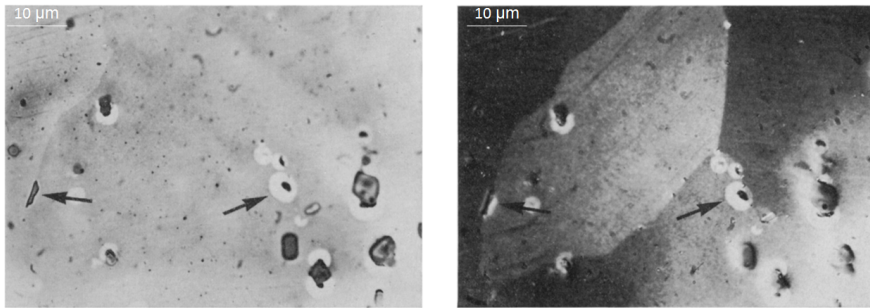


Figure 7: Optical brightfield and polarised light micrographs of U containing 4 ppm H (same region). Arrows indicate precipitated  $\text{UH}_3$  at the grain boundary (angular precipitates are assigned as carbides) [41].

Bingert [42] used EBSD (Electron backscatter diffraction) to come to a similar conclusion ( $\alpha$ -U hydrided at  $70^\circ\text{C}$  10 mins 500-650 Torr). Some preference for grain boundary precipitation was observed. Bingert reported that out of the 101 hydride sites investigated, 77% of them had nucleated on twin boundaries or high/low angle grain boundaries (identified using EBSD). Further to this Bingert could not rule out that the other hydrides could have formed at unresolved twins. Scott [43] also found preferential formation on high orientation grain boundaries for U exposed to  $\text{D}_2$  ( $320^\circ\text{C}/500 \text{ mbar}/215 \text{ seconds}$ ). Scott [44] carried out further experiments ( $240\text{-}320^\circ\text{C}/500 \text{ mbar}$ ) and found that not only is there a preference for nucleation at grain boundaries but also when there is a higher misorientation angle between the boundaries. At lower temperatures the preference for nucleation at high misorientation grain boundaries was not observed.

Grain boundary precipitation of hydrides was disputed by Adamson et al [45] for U exposed to  $\text{H}_2$  at  $600^\circ\text{C}$  for 1 hour to give 0.1-20 ppm concentrations (cooling in this case was in a switched off furnace). Adamson

maintained from TEM work that hydrides were not preferentially associated with grain boundaries. An example transmission electron micrograph is shown in Figure 8 where the white patches are assumed to be locations of  $\text{UH}_3$  particles that could not be retained during the thinning preparation. In this example 3 of 8 sites were situated on a grain boundary (37.5%).



Figure 8: Transmission electron microscopy image of U containing 0.5 ppm hydrogen. The white holes illustrate the positions occupied by hydride precipitates [45].

In conclusion all but one piece of work has suggested that hydrides could form at grain boundary preferentially. The work by Adamson that claims no preferential formation at grain boundaries still found 37.5% formation at grain boundaries and as the image shown is of poor quality the other hydrides could also have been formed at the grain boundary. This suggests

that it is likely that grain boundaries allow preferential formation of hydride precipitates.

### 1.5.2 Carbide inclusions

A common view that has been developed, is that carbide inclusions could be an important factor in the nucleation of hydrides, this has been hypothesised to occur through two different mechanisms. Firstly, if the inclusion is near the surface it could affect the oxide-layer above it [46]. Owen and Scudamore [37] suggested that inclusions cause a discontinuity in the micro structure which influences the integrity of the oxide-layer above increasing the rate of diffusion of the hydrogen which encourages hydriding. Harker et al [47] have shown that  $\text{UH}_3$  can form at the perimeter of carbides at the surface (mechanical polished), a micrograph can be seen in Figure 9. They argue that the primary factor is that edges of these inclusions allow for "the most rapid diffusion and build-up of hydrogen in the metal" and this significantly increases the hydriding rate. However, when the surface is electro polished they found no correlation of hydride formation to inclusions.

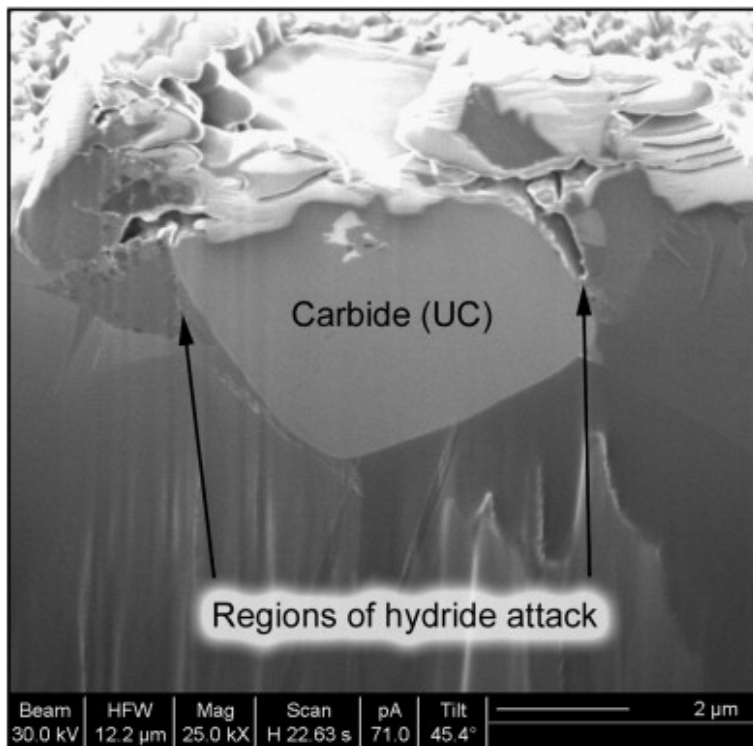


Figure 9: A carbide on the surface showing the  $\text{UH}_3$  formation around the edges (mechanically polished  $240^\circ\text{C}$ , 525 mbar  $\text{H}_2$ ) [47] .

Secondly, if the inclusion is deeper within the bulk metal it could cause a stress concentration which could allow for preferential nucleation. These residual stresses are known as Cottrell clouds and are noted by Kartal [48] who studied inclusions within a superalloy (MAR-M-002). Kartal found that there are significant residual stresses surrounding the inclusion. Arkush [49] found for uranium that carbides above a size of  $3 \mu\text{m}$  can cause stress regions which encourage hydride precipitation. With both arguing that the difference in thermal strains between the inclusion and the surrounding metal cause stress concentrations leading to preferential hydride nucleation.

Recent work by Siekhaus [50] used Secondary Ion Mass Spectrometry (SIMS) to examine the hydrogen concentration near inclusions on sectioned uranium metal samples. Siekhaus found that there is a higher hydrogen density of hydrogen near the inclusions, although, he cannot specifically attribute the higher density to hydride formation. In this case the hydrogen present is residual from the manufacturing process.

Contrary to these observations, Bingert [42] found that inclusions were not a significant site for precipitation of hydrogen. It should be noted that Bingert also prepared his samples with electro polishing techniques. Scott [43] studied the formation of deuterium hydrides and stated that deuteride growths were not able to be associated with any obvious type of inclusion (e.g. carbide) although association with pre-existing hydride inclusions could not be ruled out.

Overall there is a consensus that inclusions could cause preferential precipitation of hydrides, with the observations summarized in Table 3, but it should be noted that there is no clear picture from literature. Given this, it would appear that there may be different nucleation patterns which become dominant by changes in a) metallurgical considerations, b) preparation of uranium, c) conditions of hydrogen introduction.

Table 3: Observations from different hydriding experiments showing the variation in material, preparation and hydrogen induction and if the work has substantially linked hydrides to grain boundaries or inclusions.

Reference	Material	Sample preparation (pre-H <sub>2</sub> )	Hydrogen introduction	Grain boundaries	Inclusions
Adamson [45]	Cross rolled 145 ppm C	Pickled nitric acid	600°C mbar	N	n/a
Arkush [49]	U and U(0.1% Cr)	Polished 1 μm	50-75°C H 1000 mbar	Y	Y
Beever [41]	Drawn wire 140 ppm C	Electropolished	800°C	Y	n/a
Bingert [42]	As cast 100-300 ppm C	Polished and electropolished	70°C 800 mbar	Y	N
Bloch [51]	U and U (0.1% Cr)	Polished	130-190° mbar	n/a	n/a
Scott 06 [43]	Depleted U	Polished 3 μm	320°C	Y	N
Scott 13 [44]	Uranium 50 ppm C	μm paste	240-320°C 500 mbar	Y	Y
Owen and Scudmore [37]	Cast 500 ppm impurities	Electropolished	170°C 930 mbar	n/a	Y
Sielhaus [50]	Cast	n/a	n/a	n/a	Y*(not specifically UH <sub>3</sub> )

## 1.6 Observations regarding dimensions and number densities of sub-surface sites

There are a number of observations of sub-surface precipitates that could be useful in understanding how these precipitates develop. Some quantification (despite being of different preparations and reaction conditions) of these features will be useful to check against the model. The observations are related to their dimensions and shape in section, their observed diameters in both pre-cracked and cracked state, and the relative numbers of sub-surface protrusions versus growth centres.

### 1.6.1 Observations on dimensions and shape in section of sub-surface $\text{UH}_3$

When hydride is formed within the uranium metal it is accompanied by a large volume change. This volume change known as the Pilling-Bedworth ratio (PBR) is 71% in the bulk metal causes the surrounding metal to compressive together through the hydride's expansion. This compressive force will then interact with the uranium surface causing the surface to be under plane tension and compression. If the hydride is small enough than  $1 \mu\text{m}$  then theoretically it could be elastically accommodated by the metal itself [46]. When the hydride surpasses the elastic limit of the metal, however, the stresses produced will cause the metal to deform plastically.

A sub-surface precipitate close to the surface will deform the surface to form a blister or surface protrusion.

Bingert [42] reported these protrusions on the uranium surface and one

of his FIB (Focused ion beam) section is shown in Figure 10. In this case the  $\text{UH}_3$  was lenticular with a width of  $11\ \mu\text{m}$  and a height of  $2.36\ \mu\text{m}$  suggesting a width to height ratio of 4.6:1. Bingert argued that his oxide was removed by electro polishing. It does, however, appear that the nucleation site is still intact. This suggests that the  $\text{UH}_3$  nucleation precipitate is constrained either by an oxide or a metal overlayer.

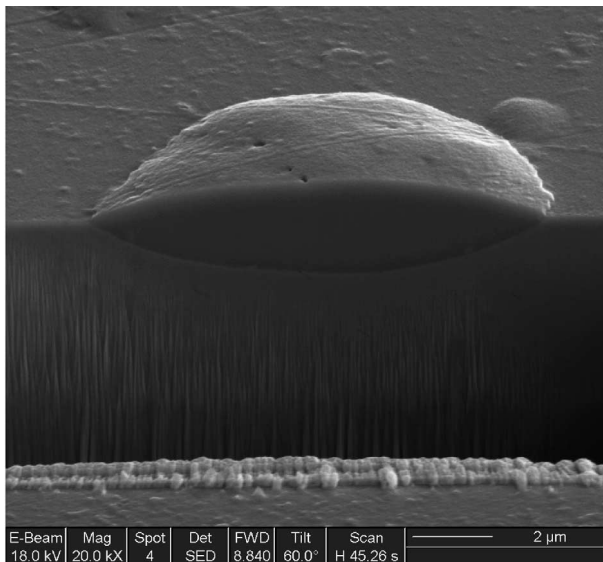


Figure 10: FIB image of a surface protrusion on depleted uranium surface (70°C 600-650 Torr, 60 s)[42]

Similar FIB-section techniques have subsequently been used by Jones et al [44] and images are shown in in Figure 11.

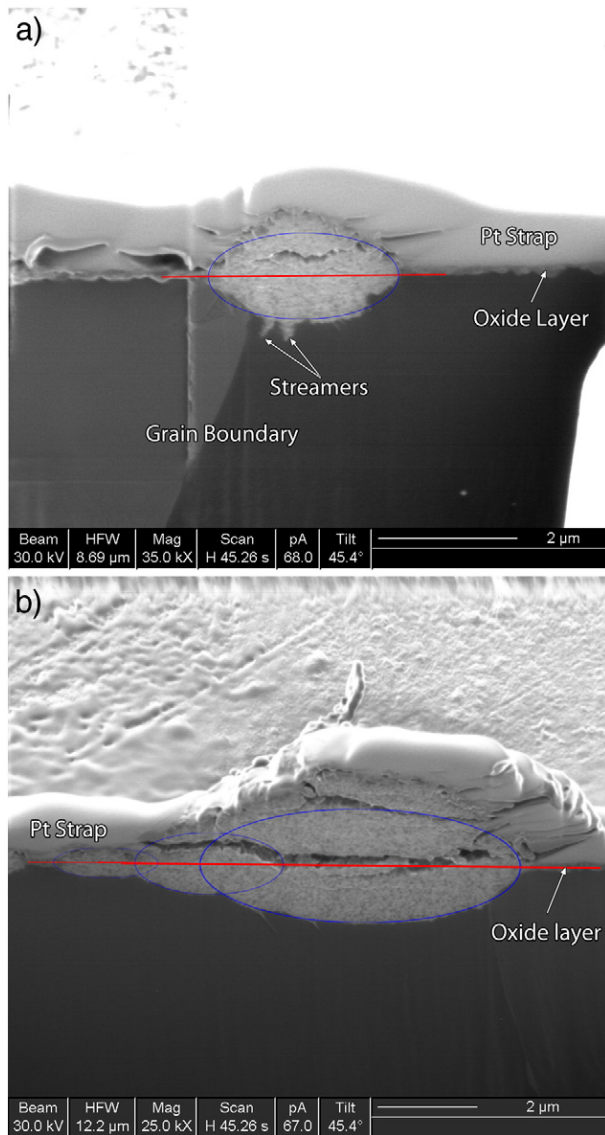


Figure 11: FIB image of two hydride sites a) on a grain boundary b) multiple hydride sites [44]

In the two examples given, presumably of protrusions that were no longer intact, the shape of the precipitates were again lenticular with width of 2.8  $\mu\text{m}$  and 4.6  $\mu\text{m}$  and a height of 1.45  $\mu\text{m}$  and 1.6  $\mu\text{m}$  respectively. These dimensions give a width to height ratio of 1.9-2.9:1. The authors also fitted

ellipses to the precipitate by eye and these were shown to have a width:height ratio of 2-2.8:1. The study came to the conclusion that for the sample polished to give minimal surface damage the hydride nucleation takes place at the metal/oxide interface or just below the interface. This work also noted the presence of streamers in both of these images: they are largest in Figure 11a where they are 80 nm long and 35 nm wide and parallel with the grain boundary.

The fact that both of these studies have found precipitates close to the surface is not surprising since FIB sectioning was carried out on features observable from the surface. It is entirely possible that other nucleation sites exist deeper in the bulk that have not been observed using these methods.

These observations are summarised in Table 4. In conclusion it can be seen that the hydride sites have a width to height ratio of 1.3-2.3:1. When tilt of the images are included the fact that Bingert's work shows a ratio of 2.3:1 as compared to Jones et al's of 1.3-2:1 may be related to sample preparation, reaction conditions (Bingert 70°C, Jones et al 240/320°C) or perhaps due to the fact that Bingerts section appears to be of a site pre-break through where as Jones et al's would appear to be post-break through.

Table 4: Comparison of surface protrusion size and shape.

	U [42] Fig. 10	U [44] Fig. 11	U [44] Fig. 11	U [51]	Gd [52]
Hydride axis ratio X:Y (from image)	4.6:1	1.9:1	2.9:1	n/a	n/a
Hydride axis ratio X:Y (include tilt)	2.3:1	1.3:1	2:1	n/a	n/a
Hydride diameter $\mu\text{m}$ (from image)	11	2.76	4.62	0.5-1	1.5

### 1.6.2 Observations regarding observed diameters in sub-surface $\text{UH}_3$

We can assume that once the hydride precipitates grow past a specific point they will influence the oxide on the surface. The oxide is a ceramic so it can deform plastically under limited compressive stress conditions and when the thickness of the oxide reaches a critical flaw size (Griffiths criteria) the oxide will fracture. A supposed example of the fracture of the uranium surface layer (which must include the oxide) can be seen in Figure 12 [9] which is of a surface protrusion feature at an inclusion. This image suggests the point at which the oxide surface begins to crack is when a surface protrusion is in the region of 4  $\mu\text{m}$  diameter.

In this example it would appear that the surface layer has already failed by the time the diameter of the fracture has reached 4  $\mu\text{m}$ . The effect of the inclusion on this result is not understood. In addition this sample was subject to a dehydrating procedure prior to SEM (Scanning electron microscope) examination the effect of this thermal cycle also cannot be discounted.

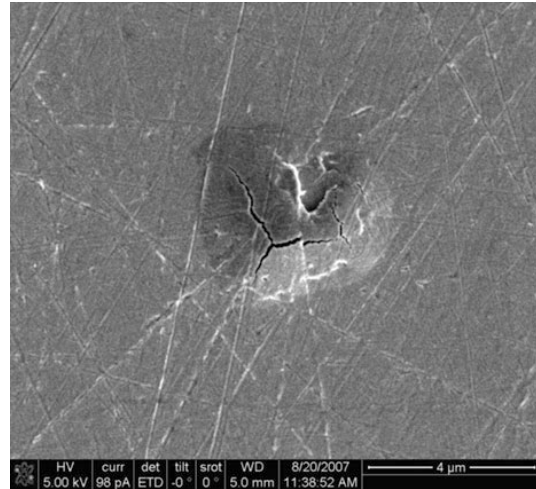


Figure 12: Micrograph of a sub-surface hydride feature with failure of the over-layer [9].

Arkush et al [53] have published a similar image of a cracked surface protrusion. In this case the example is of a 1000 mbar, 100°C exposure (120 minutes H<sub>2</sub> exposure) of C<sup>+</sup> implanted U. Despite these differences the size of the feature in its cracked state is surprisingly similar with a diameter of around 4 μm.

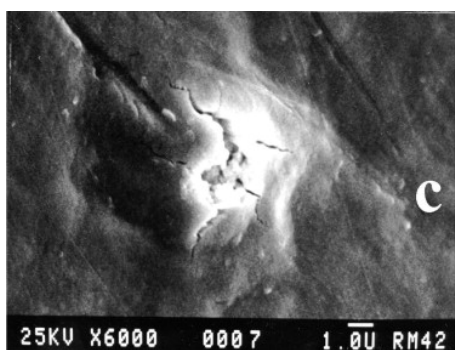


Figure 13: A SEM micrograph of C<sup>+</sup> implanted uranium a feature with failure of the oxide overlayer (1000 mbar 100°C H<sub>2</sub> 120 minutes) [53].

An example of a site which has passed the initial cracking point and has continued to grow and rupture the surface can be seen in Figure 14 this was captured by Siekhaus [9].

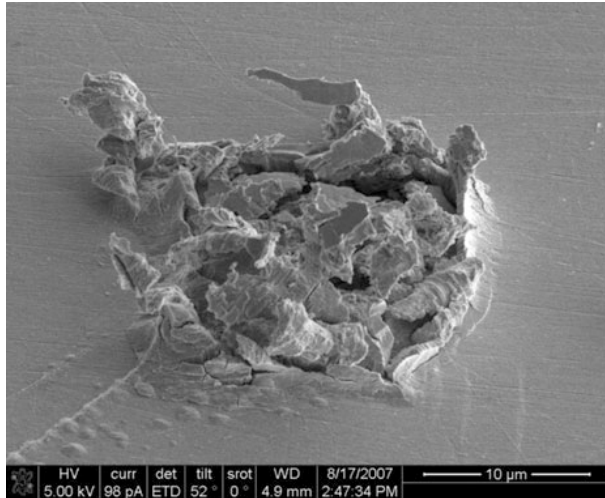


Figure 14: A  $15 \mu\text{m}$  diameter surface protrusion which has ruptured above the surface [9].

The image shows an eruption from below the surface, with the metal bending and rolling up. As the oxide is a brittle ceramic and would not be able to roll over it is likely that above the sub-surface hydride was a thin layer of metal. However, in these experiments the hydride was oxidised to enable the imaging of the sites, this could influence the reliability of the image.

### 1.6.3 Observations on the relative numbers of sub-surface $\text{UH}_3$ versus growth centres

Several studies report a fast nucleation of small reaction sites (sub-surface  $\text{UH}_3$ ) and at a triggering point some of these sites evolve into growth centres. One theory is that once the oxide-layer fractures the site transforms into a

growth centre. These growth centres are points which continue to grow and these can be seen in Figure 15 in work by Bloch et al [51]. Referring to Figure 15 a) shows the surface before the reaction has taken place b) shows the first few sites appearing c) shows the development of many sites on the uranium surface and finally d) shows that only some of the hydrides start to grow in size.

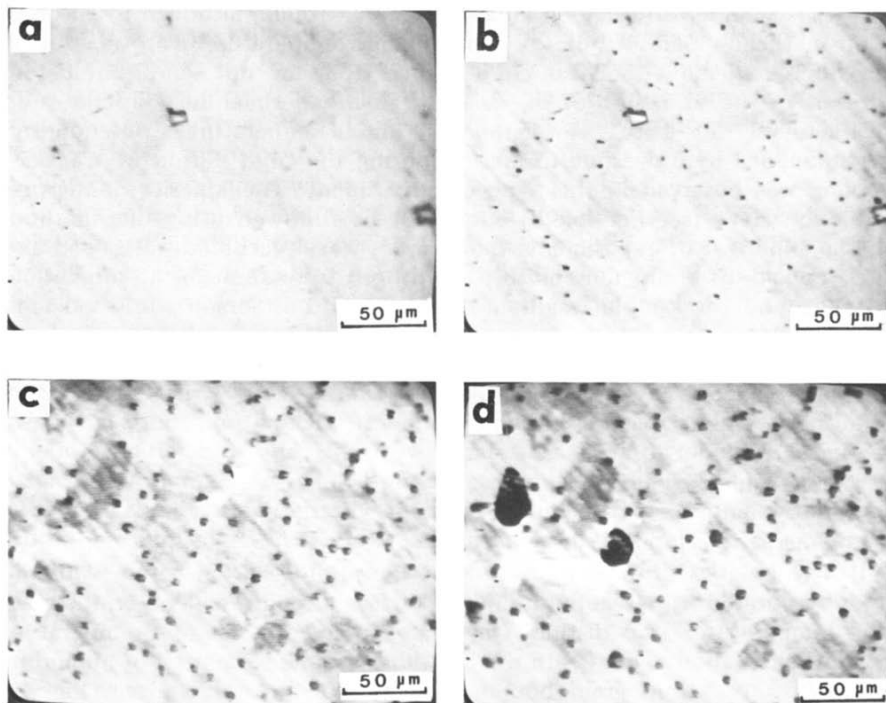


Figure 15: Shows the evolution of the hydride sites. a) Uranium before the reaction b) The first sites c) Increase in number of the hydride sites d) Some sites continue to grow [51] (240°C 900 Torr H<sub>2</sub>).

This transformation of particular hydrides sites are noted by Harker and Chohollo [15]. They observed 3125 mm<sup>-1</sup> sub-surface nucleation sites in a recent study where uranium was exposed to 10 mbar H<sub>2</sub> for a short period

of 180 seconds, whereas a similarly (but not identically) prepared sample exposed to 100 mbar of H<sub>2</sub> for 40 minutes developed  $\sim$ 4 exposed reaction sites (GCs) mm<sup>-1</sup> [15].

Work has also been carried out by Benamar [52] [54] on hydride formation on gadolinium, with Figure 16 showing the dense formation of small hydride sites and some large growth centres. This current project used ImageJ (version 1.47) to count the number of small hydride sites; finding it to be  $\sim$ 15000 mm<sup>-2</sup>. Benamar et al [54] found there was a strong dependence of hydride sites with grain boundaries, and there was a significant time delay between the initial formation of sub micron diameter hydride sites and further growth of some of these sites into growth centres, this time delay is known as an induction period. Finally, Benamar reported that the compressive stresses within the oxide-layer influence the growth of the hydrides beneath the surface [52]. The study found that for the hydride to transform into a growth centre the oxide-layer above needs to rupture so that the hydride is not constrained by the oxide-layer.

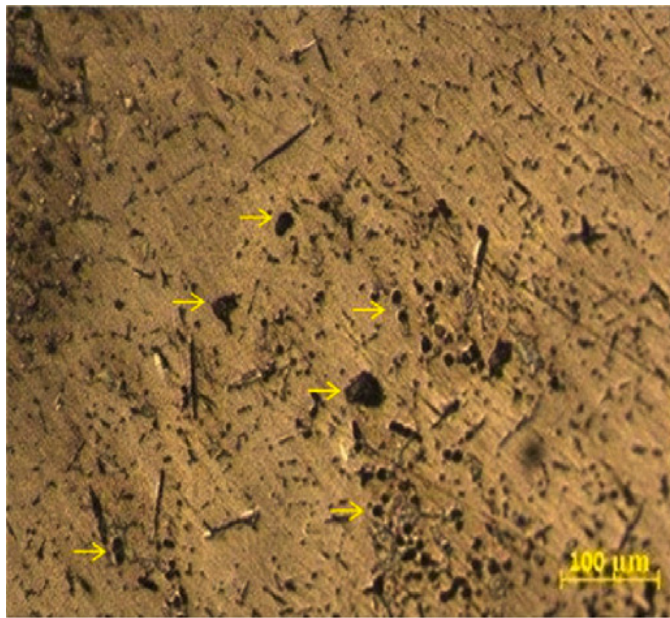


Figure 16: e the dense formation of the small hydride sites and a few growth centres that have ruptured on the Gadolinium surface [52].

Table 5 summarises hydride site densities for small sites, larger growth centres from a number of studies. There is large variation in the number of sites, from  $800\text{-}15000\text{ mm}^{-1}$ , which could relate to the material properties or sample preparation, with inclusion density and other factors having a significant effect. The relative proportion of small sites to growth centres suggest that either they represent two families of sites where one is far more common than the other, or only a small proportion of small nucleation sites transform into growth centres.

Table 5: Hydride site density for small sites and for growth centres

	Gd [52]	U [15]	U [51]	U [55]
Small hydride sites $\text{mm}^{-1}$	15000	3125	800	13000
Growth Centres%	1	0.1	n/a	n/a

## 1.7 Concept

This review leads us to a theory of how the early hydriding process occurs as shown in Figure 17. Despite the fact that both inclusions and grain boundaries have been identified as likely nucleation sites, these introduce too much complexity and will be put aside for this project. A thin coherent oxide-layer is assumed to be present before exposure to H<sub>2</sub>. The radiolysis of materials surrounding the uranium produces hydrogen gas which builds up around the uranium and the hydrogen diffuses first through the oxide and then into the metal Figure 17(a,b). Once the concentration of hydrogen reaches a high enough level, UH<sub>3</sub> precipitates, and given the spot-wise distribution of precipitated UH<sub>3</sub>, this is expected to be at chemical or metallurgical inhomogeneities Figure 17(c). These sites grow and approach an ultimate size of the order of 1-2  $\mu\text{m}$  Figure 17(d) and this limited dimension is attributed to the build up of stress surrounding the hydride . After some period (possibly related to the induction time) some of these sites grow to a point sufficient to fracture the surface that constrains them. Once exposed directly to the gas these sites transition into growth centres where the growth is both more rapid and linear.

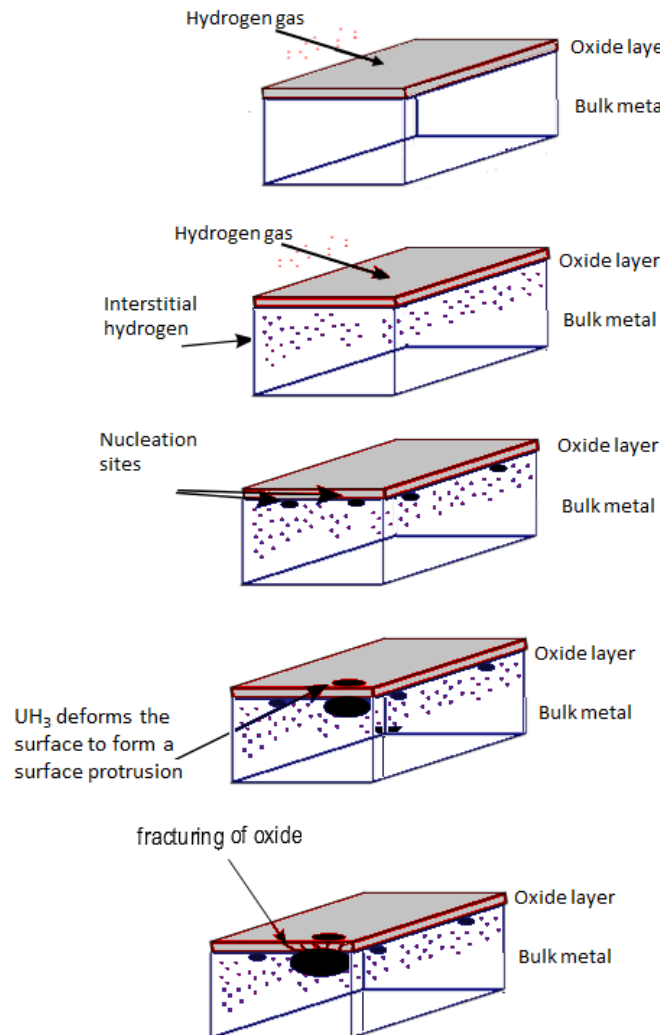


Figure 17: a)  $\text{H}_2$  is present above U with a  $\text{UO}_2$  over layer b) Hydrogen diffuses through the oxide and enters the bulk metal c) Hydrogen increases in concentration and hydride precipitates at specific sites d) Hydride precipitates grow rapidly at first but ultimately slow in their growth rate as the material around them deforms e) a small proportion of the precipitates grow to a size where the over layer fails due to the deformation: these become GCs.

## 1.8 Previous modelling work

Relevant finite element modelling work has been carried out by Greenbaum et al [56] looking at the effect the shape  $\text{GdH}_x$  precipitates have on the total elastic strain energy (TESE) within the Gd. One aim of this work was to indicate the preferred shape of the hydride. Greenbaum examined various shapes of hydride from platelet to rod shaped and some of his results can be seen in Figure 18 with a variation in stiffness defined as the ratio of bulk modulus of the precipitate ( $C_{pre}$ ) to the bulk metal ( $C_{mat}$ ). Calculations made for this thesis suggest a stiffness for the U:UH<sub>3</sub> system could be 30-120% (i.e.  $C_{pre} = 0.3\text{-}1.2 C_{mat}$ ) depending on bulk modulus. For our system we would then expect Figure 18b to be most relevant.

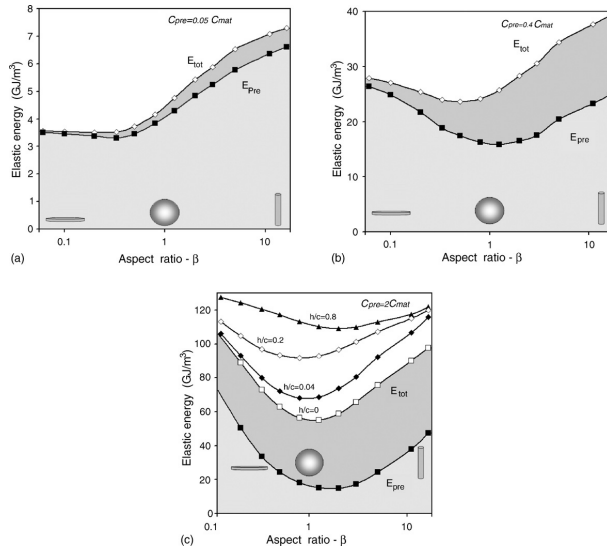


Figure 18: The normalised elastic energy as a function of the aspect ratio of a precipitate at the free surface in heterogeneous systems. a) Hydride has a stiffness of 5% of the bulk metal b) Hydride has a stiffness of 40% of the bulk metal stiffness c) Hydride has a stiffness of 200% of the bulk metal[56]

Looking at Figure 18b, which is identified as the most relevant case, this suggests that as the hydride changes shape from horizontal platelet to spherical the total energy decreases slightly, thereafter when the shape becomes more a vertical platelet the energy required increases significantly. The energy results from Greenbaum suggests that a spherical hydride would be preferential in a bulk environment and when placed near the surface with the inclusion of plasticity vertical ellipsoid (vertical ellipsoid is when the precipitate is perpendicular to the surface and horizontal ellipsoid is when the precipitate is parallel to the surface). This is different from what has been observed experimentally by Jones [44] and Bingert [42], who observe horizontal ellipsoid aspect ratios of 1.3-2.3:1 (Section 1.6.2). This may suggest that there could be other factors, that influence the total energy related to the  $\beta$ -UH<sub>3</sub> shape. These could include proximity to the surface, a pre-stressed oxide-layer, work hardened near surface layer, or perhaps the shape could be the result of precipitate growth rates responding to the local stress profile.

An example of the effect stress can have on the U-H reaction has been suggested with density functional theory calculations at LANL (Los Alamos National Lab) [46]. They found that when tensile stress is imparted on the system that, unsurprisingly, the U-U distance increases and this increases the number of hydrogen atoms that can accumulate. The effect of this is that the tensile stress could increase the hydrogen solubility limit and diffusion rate [46]. This would have the overall effect of tensile stress aiding and compressive stress limiting hydride precipitation and growth.

Later work by Greenbaum examined the stresses created by the formation of palladium hydride [57] on the surface of a FE modelled Pd coupon.

Greenbaum modelled the expansion of semi spherical hydrides on the free surface through dilatational strain. The work focused on the stresses formed in the surrounding metal and an intact oxide, an image of this can be seen in Figure 19. Although Greenbaum modelled the oxide no stress was introduced into the oxide prior to  $\text{PdH}_x$  being introduced: i.e. the oxide was not pre-stressed.

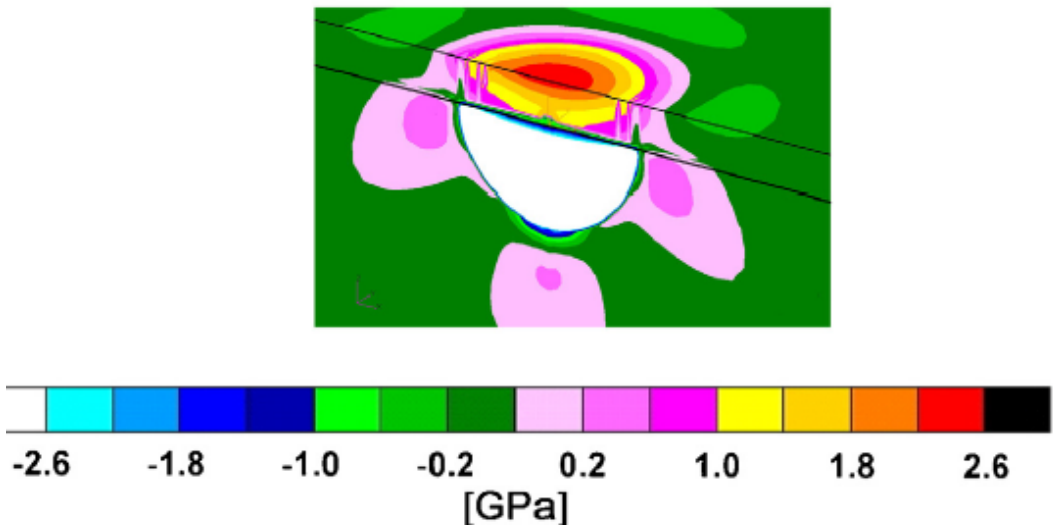


Figure 19: Greenbaum's pressure stress map of a  $\text{Pd}_H$  hydride site on the free surface with an oxide-layer 40% the thickness of the hydride and anisotropic FCC material properties [57].

Greenbaum came to a number of conclusions. Firstly, he concluded that precipitation of the hydride created regions of tensile and compressive stress that could influence the growth of existing and the nucleation of new hydrides. Secondly he concluded that the hydride growth would eventually

fracture the oxide-layer but this was not quantitatively modelled.

Greenbaums work is extremely useful in comparing to this study however there are limitations in using Greenbaums work to consider the U-UO<sub>2</sub>-UH<sub>3</sub> system:

- There is no incorporation of a interactive pre-stressed oxide. This is known to be an important factor for U (see Section 3.3).
- The hydride modelled is a semi spherical hydride at the free surface. The shapes observed in the literature are horizontal ellipsoids.
- The Pd system modelled is a highly symmetrical fcc structure. Uranium has a more complicated orthorhombic structure with anisotropic material properties and plasticity. This means that the uranium matrix orientation will have a significant effect on the surface energy of the hydride and the U:UH<sub>3</sub> interface.

## 1.9 Zirconium hydride

Some aspects of hydride expansion have been examined by Singh [58] on Zirconium and can be seen in Figure 20. Beneath the blister hydrides form radially, but elsewhere the hydrides are of a different orientation. Singh found through calculations that the region below the blister was tensile and therefore affect the hydrides orientation.

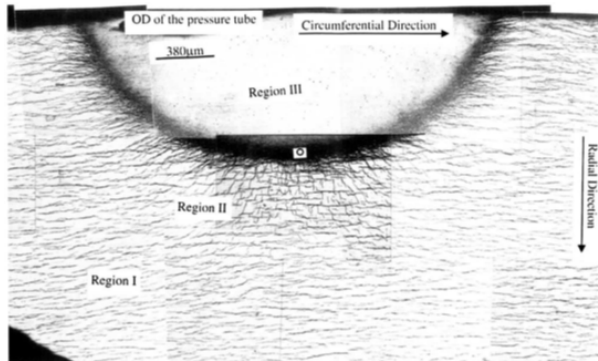


Figure 20: Optical micrograph of the section of the hydride blister, showing the changing orientation around the blister 20.

Further work examined the influence of the volume expansion on the stress of the surrounding material, with Chu et al [59] suggesting that the stress influences the orientate of the hydrides. Figure 21 indicates that the tensile and compressive stresses are influencing the growth of the hydrides. Further work by Vanergass [60] and Ells [61] suggests that the highest stress occurs just beneath the hydride and the stress decays away.

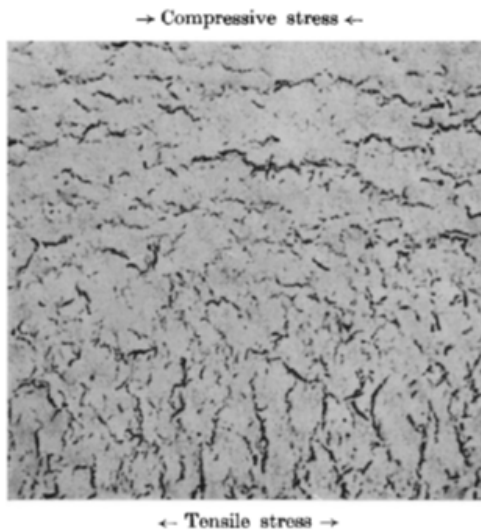


Figure 21: Optical micrograph of the section of the hydride blister, showing the changing orientation around the blister[59].

Zirconium hydride systems have many similarities with the uranium hydride and allow a few conclusions to be made. First, stress could influence the location and orientation of the hydride. Secondly, the stresses around the hydride decay away quickly and have the highest level just beneath the hydride.

## 1.10 Project Aims

Given the literature review and the above discussion on previous modelling work on related systems the project aims can be outlined as a number of questions.

### **1. What are the stresses induced by the nucleation of $\text{UH}_3$ ?**

The project aims to develop a basic understanding of how stresses are developed when hydrides of different sizes are nucleated in the metal at different depths. The influence of the pre-stressed oxide surface on the hydride beneath shall be examined for a spherical hydride.

### **2. Does stress affect the shape of the hydrides?**

A variety of information is available as to the actual shapes taken up by the hydride precipitation nuclei (FIB sections, AFM (Atomic Force Microscope), SEM). The project aims to understand how the stresses change when the shapes of the hydrides vary and whether this can account for the shapes actually observed. Further to this, the project aims to understand whether hydrides in proximity to one another can affect each other's stress pattern.

### **3. Why do some hydrides transform into growth centres**

Previous work has reported that hydride precipitates below the size of 1  $\mu\text{m}$  only deform the surrounding metal elastically [46]. However that work assumed the precipitates had a strain of 1-3% (similar to Pd) whilst  $\text{UH}_3$  has a strain of 20% (discussed in Section 3.2).

The hypothesis outlined in 1.7 suggest that some sub surface precipitates continue to grow and become growth centres while other precipitates stop at a certain size. The concept outlined suggests that one reason for this is that some hydrides fracture the oxide-layer which allows the growth of the precipitate. The orientation of the grain could also significantly influence the growth of the precipitate so this will be examined.

An additional complication not modelled in such systems is that of a work hardened layer. Experimentally samples are often prepared using abrasive media resulting in a work hardened layer in the immediate uranium sub-surface. The project aims to investigate the potential effect of this layer.

## 2 Nano-indentation of uranium hydride

This chapter describes an innovative experiment which has been designed and implemented to measure the reduced Young's modulus of  $\beta$ -UH<sub>3</sub>. Reliable material properties are crucial when creating realistic models using finite element analysis. For  $\beta$ -UH<sub>3</sub> this is problematic as the current values cited for bulk modulus are between 33-144 GPa [18] [13] [22]. This range leads to uncertainty in finite element analysis simulations with calculated stress varying by as much as 35% as discussed in Section 1.

### 2.1 Overview of experiment

Bulk and Young's moduli can be calculated from the reduced modulus derived in nano-indentation experiments [62] with Oliver and Pharr [63] developing a widely adopted method. This method has been used on many materials including by Kurosaki et al on uranium oxide [64] and Kuroda et al [65] on zirconium hydride. The nano-indentation method uses a Berkovich pyramid shaped tip made of diamond. This tip has a flat profile with a total included angle of 142.3 degrees and a half angle of 65.53 degrees, which makes it ideal for use on the thin  $\beta$ -UH<sub>3</sub> film. The tip is pressed into the surface of the material and the load and displacement are measured. The load-displacement curve produced reflects the material properties.

Given that uranium hydride is both pyrophoric and radioactive, indentation measurements on this material require the hydrogenation and indentation processes to be carried out in protective atmospheres. Further to this

$\text{UH}_3$  often spalls readily, so a method of constraint has been developed to enable a compact and adherent layer of uranium hydride to form.

To encourage the development of as stress free a film as possible i) hydride was formed at an elevated temperature ( $130^\circ\text{C}$ ) and cooled slowly and ii) the uranium metal was held within a tin metal matrix such that the  $\text{UH}_3$  was circumferentially constrained. Previous work has shown that  $\text{UH}_3$  forming under one dimensional compressive stress remained intact [66] and it was hypothesised that constraint around a small embedded sample would have the same effect. It should be noted that early work attempted the use of Ceramix (silica based resin) as a matrix material. Despite considerable effort to cure and dry the matrix,  $\text{UH}_3$  would not form in its presence. Later, successful, experiments used tin as the matrix and the hydrogenation temperature was limited to below the melting point of tin ( $232^\circ\text{C}$ ).

The phase diagram of Sn-U is shown in Figure 22 [67]. At the temperatures that the soldering iron heated the tin ( $\sim 300^\circ\text{C}$ ) an inter-metallic phase is unlikely to form unless the tin concentration in the uranium reaches a significant level. Other work by Treick et al [68] found no evidence of a solid solution of Sn within U.

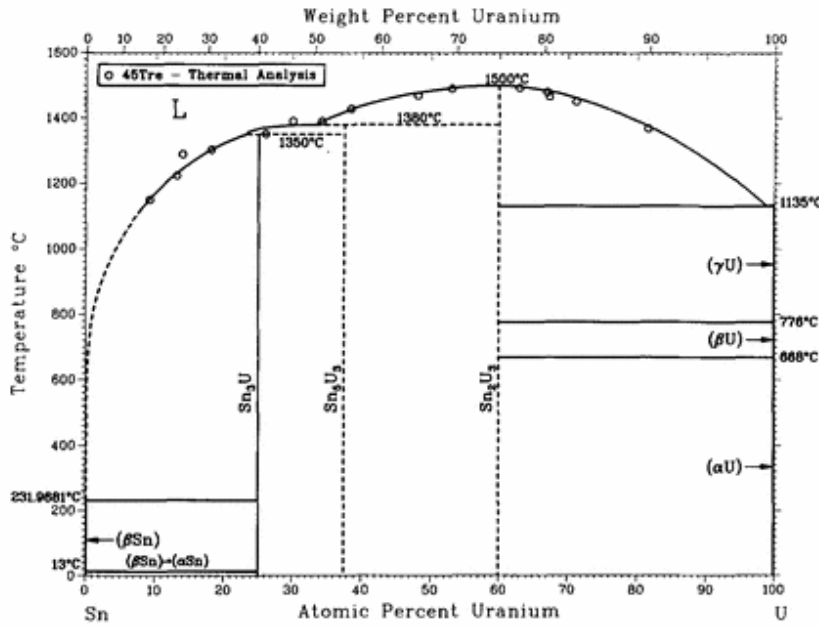


Figure 22: The Sn-U phase diagram [67].

## 2.2 Experimental procedure

### 2.2.1 Film preparation

Uranium wire (7%  $^{235}\text{U}$ , 1 mm diameter, 99.9% purity) was used as received from Goodfellows (cat no 0005120/1) and cut into a 2 mm length with pliers.

Granulated tin (British Drug House Limited, unknown purity) was heated just past its melting point (231°C) in an aluminium mould of diameter 19 mm and depth 4 mm. The uranium wire was set into the material and further tin was added to submerge the uranium. The setting operation was carried out at a low enough temperature that it could be easily carried out with a soldering iron ( $\sim 300^\circ\text{C}$ ). Typically the setting operation could be carried

out in under thirty minutes, an image of an as-set sample can be seen in Figure 23.

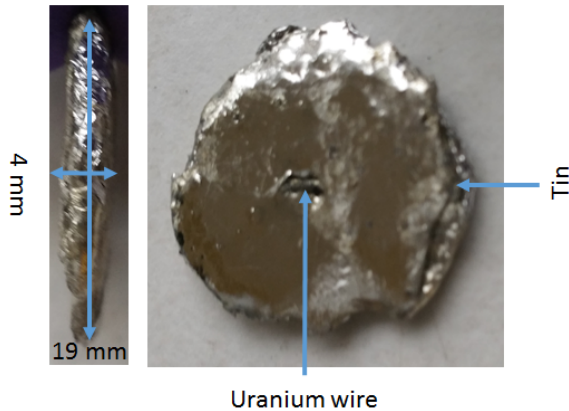


Figure 23: A photograph of an as-set 2 mm length uranium wire surrounded by tin with a diameter of 19 mm (Sample 10).

The two sides of the (Sn constrained U) block were polished to 4000 grit with water. This provides a smooth Sn-only underside and a U-with-Sn top surface where the Sn and U were polished flush. Immediately after polishing the block was rinsed in water and dried using paper towels before loading in air into the reaction cell. The approximate time of air exposure after polishing was 20 minutes.

The reaction cell was constructed from an aluminium tube (Edward's Vacuum, Part number:C10516409, length:130mm) and connected to a gas line with  $\frac{1}{4}$  inch VCR gaskets (Swagelok). Aluminium was used as it does not store and out gas hydrogen as a steel vessel would. The cell was heated externally with a heating tape which was controlled automatically with the use of a thermocouple between the cell and heating tape. The experimental

set-up is shown in Figure 24. The apparatus was contained within a fume cupboard in which the hydrogenation procedure was carried out.

Referring to Figure 24, the input for the hydrogen and argon is shown on the left. The argon (1) and 20%/80% hydrogen/argon mix (2) pass through a valve (3) to the main aluminium chamber (4) where the sample is held. The gas flows through the exit valve (5) and is vented into the fume cupboard. The entire hydrogenation step is carried out at atmospheric pressure.

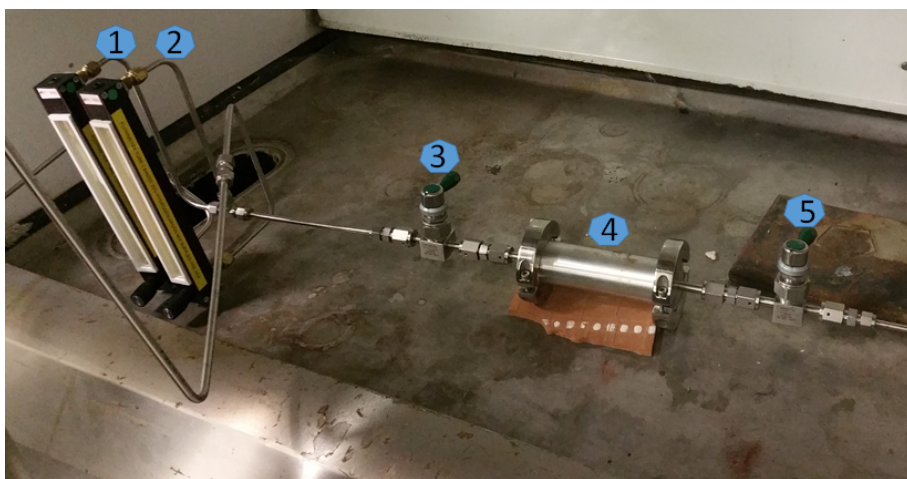


Figure 24: Photograph taken of the hydrogenation experimental set-up. The argon and hydrogen enter from the left hand side and flow through the aluminium chamber where the sample is placed. The chamber is heated by heating tape, the gas exits through the tube on the right.

After sample loading, argon was flowed through the cell for a minimum of 2 hours at room temperature and atmospheric pressure with a flow rate of  $220 \text{ cm}^3\text{min}^{-1}$ . Following this, the temperature of the heating tape was raised stepwise to 50°C, 90°C, 120°C, 150°C, 180°C and finally 210°C under the same flowing Ar. This step is designed to slowly remove adventitious water (and limit additional oxidation of the uranium) while at the same

time activating the uranium surface for hydriding and ensure it reacted as a surface rather than spotwise.

Once the activation process was complete a 20:80 H<sub>2</sub>:Ar mix was flowed through the cell for 60 minutes at a flow rate of 280 cm<sup>3</sup>min<sup>-1</sup> at the same temperature (heating tape 210°C, cell 125°C); followed by Ar during the cool down phase (sample was allowed to cool naturally). Once cool the cell contents were isolated in Ar by closing valves 3 and 5 (Figure 24) and the cell was moved into an Ar glove box for disassembly.

Figure 25 shows a time-temperature profile identical to that used for Sample 9 with the measured temperature both at the heating tape and inside the reaction chamber under flowing gas; the temperature controller set points are also shown. Under flowing argon gas the temperature at the centre of the cell was lower than the heating tape measurement by up to 85°C when at peak temperature. It should be noted that as the sample was resting on the reaction chamber wall, the actual temperature experienced by the uranium would probably be greater than the temperature indicated for the centre of the reaction chamber.

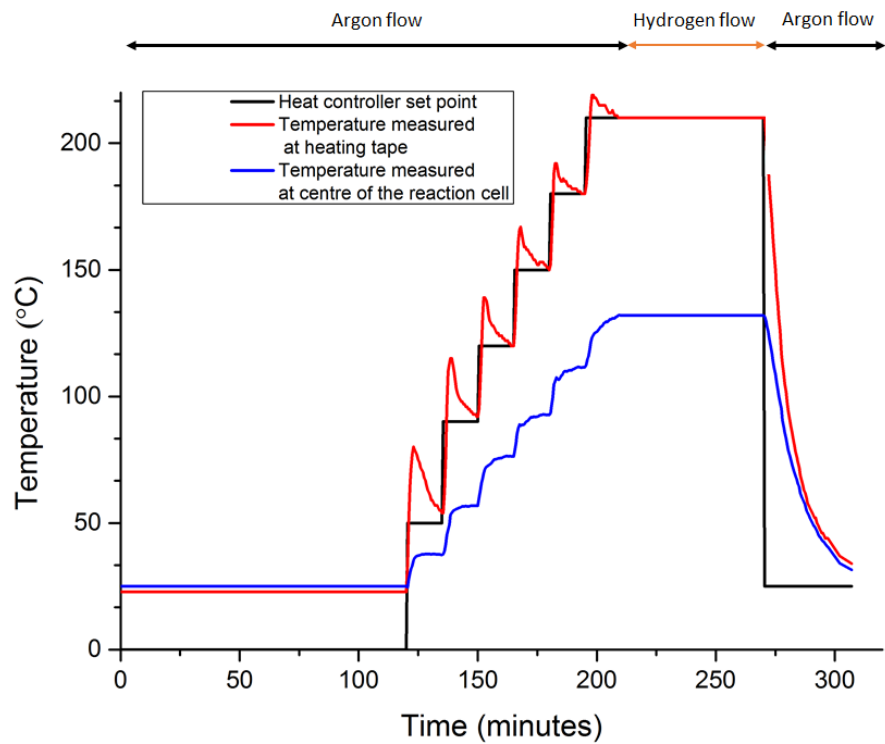


Figure 25: Time temperature profile identical to that used for Sample 9.

Details of all attempted  $\text{UH}_3$  film preparations are included in Table 6. Gold and grey films were assumed to be oxide-layers and were not investigated further.

Table 6: Temperature and hydrogen flow rated for the hydriding procedure

Sample	Matrix	Activation steps			Hydrogenation steps			Observations
		Ar flow at RT (Room Temperature)	Ar gas before hydrgenation (cm <sup>3</sup> min <sup>-1</sup> )	Ar/H <sub>2</sub> gas flow (cm <sup>3</sup> min <sup>-1</sup> )	(%) flow temperature (min)	Hold time at reaction temperature (°C)		
1	Ceramix	190	140	80	30	180		no change
2	Ceramix	140	140	100	30	180		gold film
3	Ceramix	120	140	100	45	180		no change
4	Ceramix	180	220	120	90	180		grey film
5	Ceramix	270	220	140	60	180		no change
6	Ceramix	270	220	220	60	220		dark colour
7	Sn	150	220	80	60	210		dark spots
8	Sn	120	220	220	30	210		black spots
9	Sn	120	220	280	60	210		black powder
10	Sn	120	220	280	60	180		black film

### **2.2.2 X-Ray Diffraction**

The sample was removed from the reaction cell and placed in a Bruker specimen holder capable of isolating the sample from air (Part no. A100B37). The sample was held in the glovebox for 24 hours prior to removal and transported to the diffractometer. Diffraction patterns were collected on a Bruker D8 Discover diffractometer. Samples 6 and 7 used a 2 mm collimated Co source ( wavelength of 17.9 nm)and Samples 8 and 9 used a 1 mm collimated Cu source (wavelength of 15.4 nm). Collection time in each case was 4 hours. It should be noted that the results using the Cu source (15.4 nm) were significantly higher quality than that of the Co source. A Rietveld model analysis of the data was performed at AWE and is included in this thesis.

### **2.2.3 Tomography**

The uranium wire was first removed from the tin setting and placed upright in an NMR (Nuclear Magnetic Resonance) tube under argon. Tomography was attempted on Sample 8 using the Nikon Metris Custom Bay Tomography System at The University of Manchester Materials Department. The energy of the X-rays were 220 keV and allowed for a voxel resolution around  $5 \mu\text{m}$ .

### **2.2.4 Nano-indentation**

The sample was removed from the reaction cell within the glove box, inspected and installed in a removable temperature stage shown in Figure 26. The temperature stage provided a gas seal around the sample except for the tip entry point which was temporarily sealed with tape.

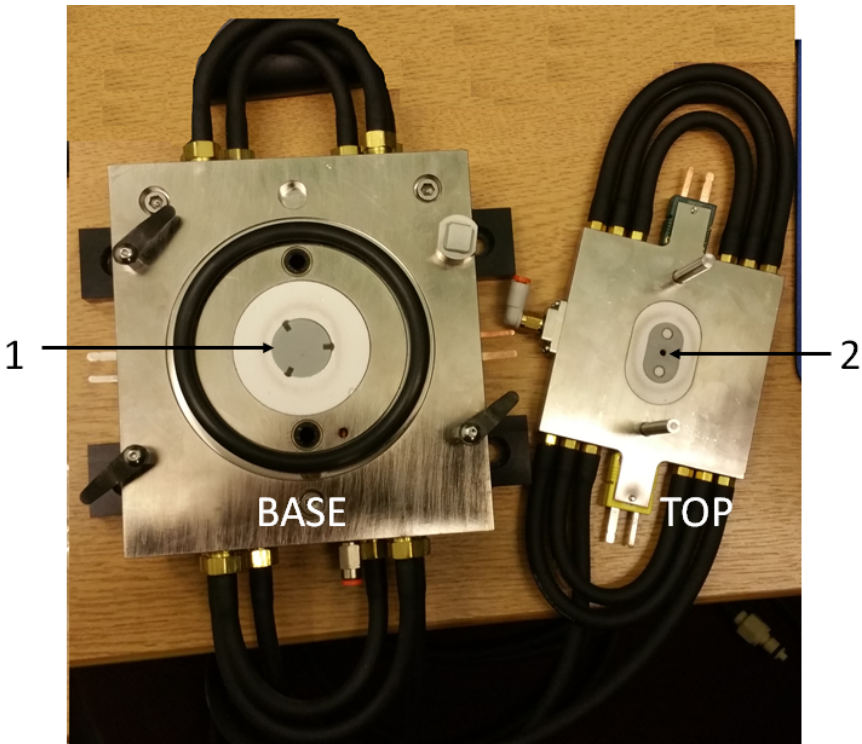


Figure 26: Photograph of the temperature stage used in nano-indentation experiments. The sample is placed in the centre of the base (1). The top of the stage is placed on the base forming a seal and the nano-indenter tip reaches the sample through the hole shown (2).

The temperature stage containing the sample was removed from the glove box and installed in a Hysterion TI 950 TriboIndenter. The calibration of the nano-indentor was carried out in two phases. Firstly fused silica was used to calibrate the equipment 24 hours before the experiment. Secondly a further quick calibration on polycarbonate was carried out 5 minutes before the indentations to ensure the machine was still calibrated. Two gas entry points to the temperature stage were connected to argon: one to the temperature stage and the remaining to flow a shield of gas over the nano-indentor

tip entry point (with tape removed). The procedure was sufficient to protect hydride films from noticeable oxidation. The sample could be observed optically during the experiment as shown in Figure 27.

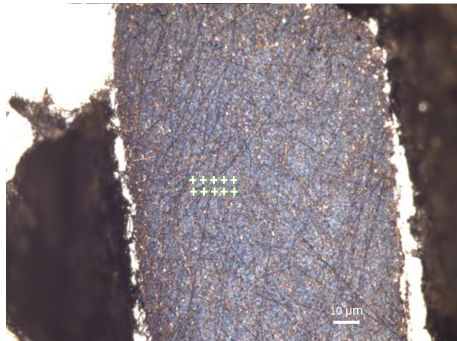


Figure 27: Optical image of Sample 10 whilst in the nanoindenter. Area of interested is indicated.

A three-sided diamond Berkovich indenter tip with radii of 50 nm was used. The indentation load was raised up to  $8000 \mu\text{N}$  and was loaded/unloaded at constant pressure of  $800 \mu\text{N}$  per second and was held for 5 s at the maximum pressure. The experiments were carried out at room temperature and in-between each indentation there was 45 s stabilizing time. The form of the load-displacement graph is shown in Figure 28 through which a number of parameters are derived. Referring to Figure 28 S in the stiffness matrix,  $H_f$  is the final displacement,  $h_{max}$  is the maximum depth of indentation.

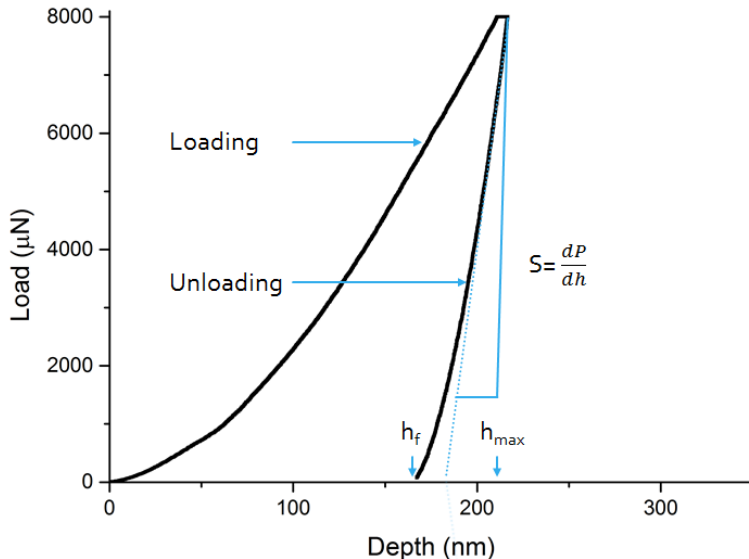


Figure 28: An example of a load-displacement graph with important features highlighted.

## 2.3 Results and discussion

### 2.3.1 Film preparation

Collected observations from the various sample experimental runs are shown in Table 6, the important experiments are discussed in more detail below.

Early experiments were, either because of leaks or the Ceramix matrix, apparently unable to form  $\text{UH}_3$ . Instead the uranium surface apparently oxidised and either developed a gold or grey film or was unchanged.

The use of a higher temperature (heating tape  $210^\circ\text{C}$ , cell contents  $125^\circ\text{C}$ ) with the Ceramix matrix was sufficient to possibly promote  $\text{UH}_3$  formation (Sample 6) but the use of tin as a substitute matrix was more reliable in

promoting  $\text{UH}_3$  formation (Sample 8). Under certain conditions the hydrogenation was observed to have proceeded too far. For example Sample 9 was observed to be a black powder upon removal from the XRD (X-Ray Diffraction) cell. It is not known at what time this material became a non-adherent hydride.

The ideal experimental parameters were determined for Sample 10 as 120 min Argon flow at RT, 60 min reaction time at 180°C with a  $\text{H}_2/\text{Ar}$  flow rate of  $280 \text{ cm}^3\text{min}^{-1}$ . This resulted in an apparently adherent  $\text{UH}_3$  film with a small amount of powder surrounding the perimeter of the sample. It is noteworthy that scratch features can be observed on the  $\text{UH}_3$  film (Figure 27), presumably from the uranium preparation (4000 grit). These scratches are likely to be in size of the order of the  $1 \mu\text{m}$ . The fact that they can still be observed gives an indication that the  $\text{UH}_3$  film is not very thick.

### 2.3.2 XRD

X-ray diffraction confirmed the identity of  $\beta\text{-UH}_3$  on Sample 9 as shown in Figure 29a. Assignment of  $\text{UH}_3$  peaks is as per Bussiba et al [69] in Figure 29b.

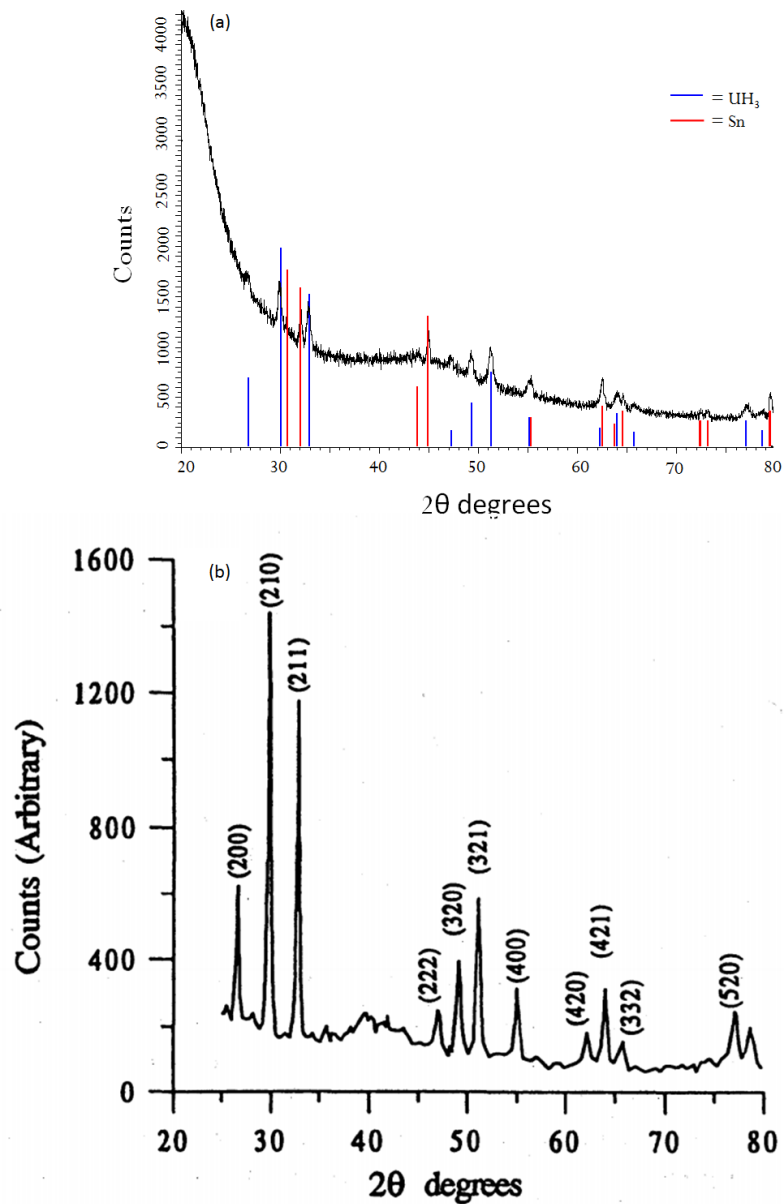


Figure 29: a) x-ray diffraction pattern of Sample 9 with blue positions indicating  $\beta\text{-UH}_3$  and red positions indicating the Sn matrix; b) diffraction pattern collected by Bussiba et al [69].

There are two points of note, firstly the lack of unassigned peaks suggests that a reaction between uranium and tin is unobserved. Secondly, uranium metal peaks are not observed. This would suggest that the film thickness greater than several  $\mu\text{m}$ .

Despite the analysis footprint being only  $1 \text{ mm}^2$  the diffraction pattern clearly shows signals from the Sn matrix as would be expected.

Further Rietveldt analysis (TOPAZ software) on the XRD data at AWE permitted the calculation of the crystalite size to be  $20.6 \pm 0.6 \text{ nm}$  and the lattice parameter to be  $6.664 \pm 0.0009 \text{ \AA}$  which is slightly larger than found experimentally by Bartscher et al of  $6.643 \text{ \AA}$  [70].

### 2.3.3 Tomography

The results from tomography of Sample 8 can be seen in Figure 30. In the images it is not possible to distinguish the hydride layer on the surface of the uranium. As noted above, the voxel size for this observation was around  $5 \mu\text{m}$ . The lack of observations of  $\text{UH}_3$  in this case is thought to be the result of a combination of factors i) the thin nature of the  $\text{UH}_3$  layer, ii) the large difference in x-ray attenuation between  $\text{UH}_3$  and U, and iii) the hydride could have detached during the setting phase.

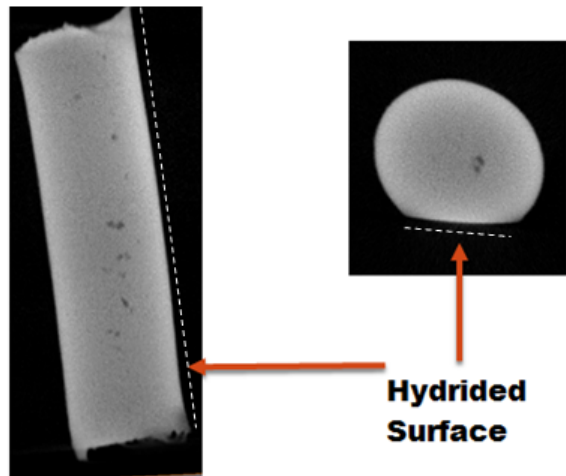


Figure 30: Tomographic image of Sample 8 with the hydrided surfaces indicated by a dotted white line.

#### 2.3.4 Nano-indentation

The results for the nano-indentations are collected together in Figure 31.

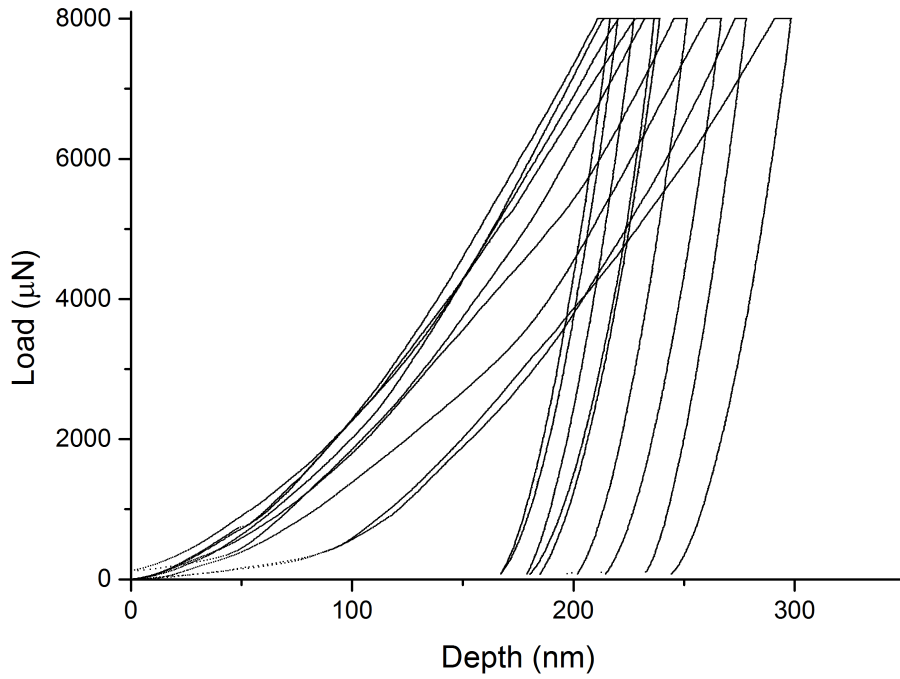


Figure 31: The load-displacement graphs for the indentations (Sample 10).

The maximum depth of indentation,  $h_{max}$ , differs by as much as 25%. In addition, some of the loading curves are initially less steep. This difference in shape is likely due to the fact that even though the uranium was polished to 4000 grit the hydride surface retains some surface roughness. To derive a representative result an average of the data was taken once outliers were identified and removed. An example of an outlier is shown in Figure 32.

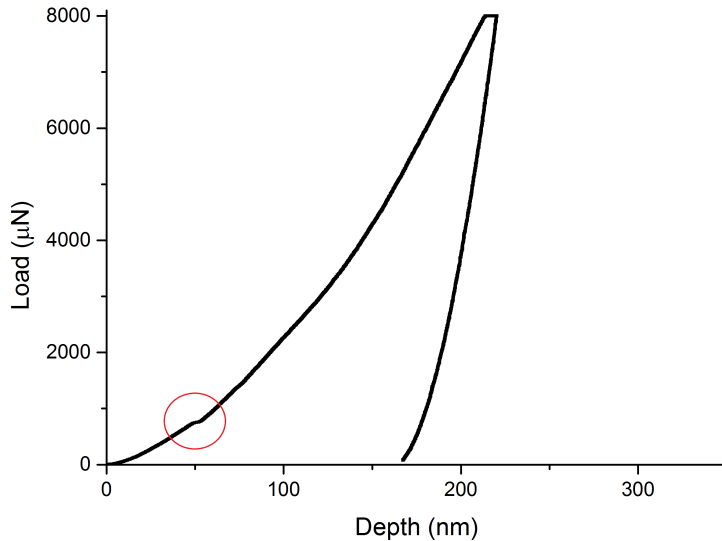


Figure 32: Indent 2 of Sample 10. A flaw that is highlighted by the red circle

Figure 32 highlights a particular feature of the load displacement curve with a red circle. This is a flaw in this indentation, where there is a jump in the measurement, this jump is most likely due to either a slip in the tip due to the hydride surface being uneven or the hydride fracturing under the increasing load. The result from this indent is not reliable and therefore will not be used in further analysis, in total four of the ten indents were ignored due to flaws in the measured load displacement curve. The results are shown collected together in Table 7.

The reduced Young's modulus was calculated using the equations from work carried out by Pharr [71]. This involves fitting the unloading curve and then differentiating the curve to find the unloading stiffness,  $S$  from

Table 7: Nanoindentation results

Indent	hc (nm)	S (MNmm <sup>-1</sup> )	A(Nmm <sup>-2</sup> )	hmax(nm)	Er(GPa)	H (GPa)	Drift (nms <sup>-1</sup> )	Notes
1	233	247	1.48	257	179	5	0.41	removed due to high drift
2	192	245	1.03	217	213	8	0.03	removed due to kink in curve
3	274	248	2.03	299	154	4	-0.21	included
4	214	258	1.26	237	203	6	-0.39	removed due to high drift
5	214	236	1.26	239	186	6	-0.18	included
6	203	248	1.15	228	205	7	-0.19	included
7	255	264	1.77	278	175	5	-0.15	included
8	228	250	1.42	251	185	6	-0.13	included
9	242	241	1.60	267	168	5	-0.12	included
10	196	243	1.07	220	207	7	-0.15	removed due to kink curve

Equation 4

$$S = mB(h_{max} - h_f)^m - 1 \quad (4)$$

where  $h_{max}$  is the maximum displacement,  $h_f$  is the final displacement after loading and B and m are fitting parameters. This then allows the calculation of the reduced modulus,  $E_{eff}$

$$E_{eff} = \frac{1}{\beta} \frac{\sqrt{\pi}}{2} \frac{S}{\sqrt{A}} \quad (5)$$

where  $\beta$  is the geometry of the tip and A is the contact area of the tip within the material. This led to the final  $E_{eff}$  value of  $180 \pm 30$  GPa, where the error shown is from the large spread of the results. Then from this we can find the Young's Modulus, E using Equation 6

$$E = \frac{(E_{eff} - \frac{E_i}{(1 - \nu_i^2)})}{(1 - \nu^2)} \quad (6)$$

where  $\nu$  is the Poisson ratio for  $\text{UH}_3$ ,  $\nu_i$  is the Poisson ratio for the indenter tip and  $E_i$  is the Young's modulus for the indenter tip. Since the only data that is available for the Poisson's ratio  $\nu$  for  $\beta\text{-UH}_3$  is from calculations carried out by Taylor [26] (0.32) and Zhang [22] (0.3) an average of those values was used (0.31). From these calculations the Young's Modulus is found to be equal to  $190 \pm 30$  GPa. A further calculation of the Bulk Modulus (K) is from Equation 7

$$K = \frac{E}{3(1 - 2\nu)} \quad (7)$$

where  $E$  is the Young's modulus and  $\nu$  is the Poisson ratio for  $\beta\text{-UH}_3$ . The bulk modulus is then calculated to be  $180 \pm^{20}_{40}$  GPa which is within the calculated result carried out by Taylor [26] of 144 GPa.

Since the Poisson ratio used in the calculations is uncertain Figure 33 shows the how the bulk modulus calculation changes with different Poisson values. The values found from DFT calculations are also plotted on the graph. With the results indicating that the DFT simulations are 13-18% less than the experimental measurements.

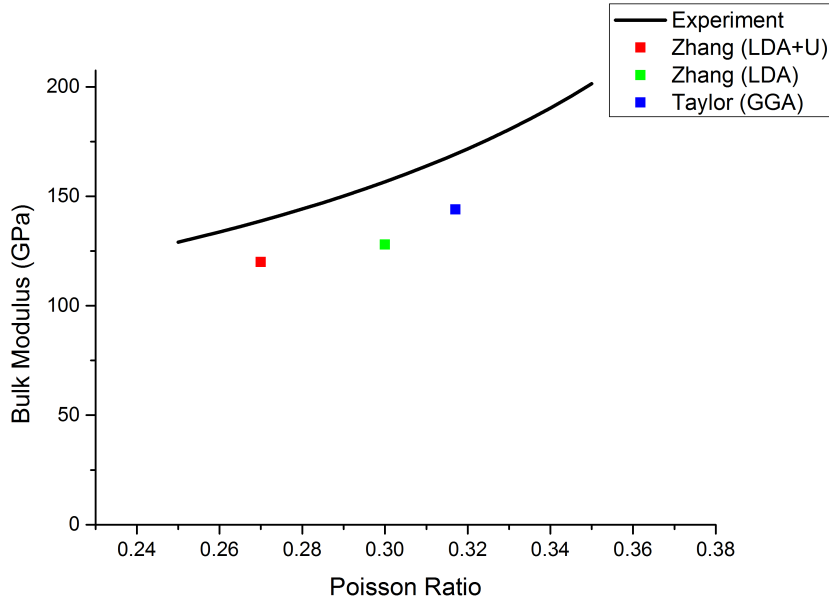


Figure 33: The bulk modulus calculation with different Poisson values, values found from DFT calculations are also plotted on the graph

The primary error in this experiment is due to the roughness of the uranium hydride surface. The average result from all of the indentations is taken to attempt a statistical average for the results, however, the error of the result is considerable as there are only seven indents measured.

The second most significant error is due to this drift of the indenter tip. This is caused by movements of the tip during the experimental procedure. Even the smallest amount of background noise can affect the result. To minimise this the machine is placed on a stabilising table which attempts to counteract any background noise. The tip is also affected by electrostatic charge build up surrounding the tip which can move the tip. It was calculated from the drift velocity that the maximum error for the drift of the tip was 5%

A third mechanism that can influence the accuracy of the calculations used in the determination of the reduced modulus, is pile up, which has been noted by Pharr [71] to increase the value of the reduced modulus from the previous calculations by up to 50%. This is when the material surrounding the indenter piles up around it and affects the contact pressure. The main determining factor for pile up is when the value of  $\frac{h_f}{h_{max}}$  is close to 1. For these indents this ratio varied from 0.69-0.82 for all of the results, so it was assumed that pile up was not a significant factor.

Another important mechanism that could affect the reduced modulus result is the thickness of the uranium hydride layer. This has been noted by Chiang [72] and is part of the BS:EN:ISO14577-4:2007s [73] where a film thickness greater than 10 times the maximum displacement is needed for accurate results. The contact depth,  $h_c$  is calculated using Equation 8

$$h_c = h_{max} - \varepsilon \frac{P_{max}}{S} \quad (8)$$

where  $h_{max}$  is the maximum displacement,  $\varepsilon$  is dependent on the indenter geometry which is found to be 0.75 Berkovich tip [74],  $P_{max}$  is the maximum pressure and  $S$  is the unloading stiffness. For these nano-indentation results the values for  $h_c$  range 190-270 nm.

Referring to the above references, a film thickness of 1.9 to 2.7  $\mu\text{m}$  of  $\text{UH}_3$  would be required for accurate results. Thinner  $\text{UH}_3$  thicknesses may allow an influence of the underlying uranium metal (with a Young's modulus of 200 GPa or more) which would slightly increase the calculated value for  $\text{UH}_3$ . In our case since XRD data on Sample 9 showed a diffraction pattern for  $\text{UH}_3$  in the absence of a pattern for uranium, we can have some confidence that the film thickness was greater than the 1.9 to 2.7  $\mu\text{m}$ . However the calculations presented here should be taken as the upper limits for possible bulk and Young's modulus of  $\beta\text{-UH}_3$ .

## 2.4 Summary

This innovative technique of constrained hydride growth within tin has enabled the measurement of the reduced modulus of  $\beta\text{-UH}_3$  for the first time. From this reduced modulus it is possible to calculate the bulk modulus  $180 \pm^{20}_{40}$  GPa. The result from this experiment gives considerable weight to the calculated values of bulk modulus of Taylor and Zhang [13] [22]. Simulations in Sections 4-6 will use a value of 144 GPa for bulk modulus of  $\beta\text{-UH}_3$  as per Taylor [13].

### 3 Model development

The U-UO<sub>2</sub>-UH<sub>3</sub> system is complex and there are many challenges when attempting to create a realistic finite element (FE) model. To simplify the model certain assumptions have to be made about this reaction. In this chapter is a discussion about the oxide-layer and hydride nucleation and how these are applied to the creation of the FE model.

#### 3.1 Modelling the oxide-layer

As discussed in Section 1, the surface passivation layer is likely to affect both the nucleation and growth of sub-surface hydrides. This passivation layer is principally a UO<sub>2+x</sub> oxide-layer where the properties (H transport and mechanical) are related to the conditions under which it forms. The layer is assumed, for the purpose of this work, to be UO<sub>2.0</sub> due in part to the availability of data and the complexity of the stoichiometry.

When an oxide-layer is formed the density of the oxide is often different to the density of the metal and therefore there will be a change in volume. The ratio of the volume of the oxide to the metal is known as the Pilling-Bedworth Ratio (PBR) [75] and is shown in Equation 9,

$$PBR = \frac{V_{oxide}}{V_{metal}} \quad (9)$$

where V<sub>oxide</sub> is the volume of the oxide and V<sub>metal</sub> is the volume of the metal.

The combination of the PBR for UO<sub>2</sub> being 1.97 and the fact that the

oxide forms at the oxide metal boundary (anionic diffusion) has the result that the change in volume on creating oxide causes the oxide-layer to form under lateral compressive stress, with a consequent tensile stress induced in the metal underneath. The normal stress in the oxide is zero as it is a stationary free surface.

The lateral compressive stresses in a  $\text{UO}_2$  overlayer have been determined using tensile creep data and a simple model by Kench [76] to be 1.93 GPa in coherent oxide films grown at 500°C. A recent study by Chernia et al [77] found the stress to be 6.5 GPa when the oxide-layer is 270 nm thick whilst Kim et al [78] determined compressive stresses in zirconium oxide to be 5 GPa. These stresses could have a significant effect. Benamar et al [52] demonstrated that the presence of an intact coherent oxide or ruptured oxide altered the orientation of the hydride beneath (oxide coated Gd).

Harker [36] has shown there is a strong correlation between the oxide thickness and the induction time of the  $\text{U}+\text{H}_2$  reaction. The study found that the induction time increases as the oxide thickness increases for oxide films up to 48 nm. There was a strong correlation with pre-breakaway intact oxide (up to 48 nm), but a weaker correlation post breakaway. Further to this, Teter et al [35] has indicated that thicker oxides produce fewer larger growth centres but the size of the growth centres is not necessarily a direct result of the oxide thickness.

The kinetics of uranium oxidation has been studied extensively [79]. Of particular interest to this thesis is the thickness the oxide reaches when spallation or failure occurs. Often known as the break point or breakaway (due to the measurable change in the oxidation kinetics). This break point for

$\text{UO}_2$  overlayer was reviewed by Harker [36] and was found to occur in the range of 48-370 nm depending on experimental and oxidation conditions. The oxide thickness used for the simulations in this thesis is 64 nm, which is the thickness determined experimentally at AWE by Chohollo [15] for the work the model will compare to. We have reasonable confidence that for these experiments the thickness is below that of the break point (failure of the oxide) due to the fact that oxide was still growing at a parabolic rate when it was stopped prior to hydriding.

### **3.1.1 Oxide stress relaxation mechanisms**

Several stress relieving mechanisms have been suggested to occur during oxide-layer growth. These will influence the stress level of the oxide during growth and the subsequent nucleation of hydride beneath the surface.

#### **3.1.1.1 Oxide creep**

The first stress relaxation mechanism of relevance is the creep of the oxide at high compressive stress. At temperatures below 1400°C Canon [32] found that no creep has been measured within  $\text{UO}_2$  pellets over a time scale of  $\sim 1000$  hours. While further work by Shunk [80] found that at low temperatures (25°C) no plasticity occurs.

Setzer et al [81] have shown that in  $\text{UO}_{2+x}$  there is a increase in the creep rate with an increased number of excess oxygen atoms present within the oxide-layer. This is important because we would expect a superstoichiometric  $\text{UO}_{2+x}$  oxide in the real world situation. For reasons of lack of experimental data in this region and complexity this effect is omitted.

### 3.1.1.2 Anisotropic growth of the oxide

Uranium dioxide has a face centred cubic structure but is known to exhibit anisotropy [77] due to the growth of favourable crystallographic planes.

A simulation was run which assumed isotropic oxide growth across the whole of the oxide-layer. The results of the simulation show that if isotropic growth of the oxide is assumed then the stresses induced on the oxide surface are found to be 42 GPa when the oxide is 64 nm. This is shown in Figure 34 and is significantly higher than that reported experimentally (6.5 GPa) [77].

Parise [82] used data from flexure bending experiments to calculate the anisotropic growth tensors. Parise grew a zirconium oxide (PBR 1.56) layer on one side of a zirconium coupon and calculated the thin film compressive stress by measuring the bending of the specimen. An assumption was made that the oxide grew by an anisotropic growth strain tensor  $\xi^{pt}$ , as shown in Equation 10.

$$\xi^{pt} = \begin{bmatrix} \xi_1^{pt} & 0 & 0 \\ 0 & \xi_1^{pt} & 0 \\ 0 & 0 & \xi_3^{pt} \end{bmatrix} \quad (10)$$

Parise used a FE model to determine the anisotropic variables by fitting the oxide expansion in the model to the experimental flexure measurement. The work concluded that the oxide-layer has a different strain rate in the lateral direction ( $\xi_1^{pt} = 0.005$ ) to the perpendicular direction ( $\xi_3^{pt} = 0.54$ ).

Similar flexure bending experiments were carried out by Weirick on Th [83] and U-Nb-Zr alloy [84] samples. Unfortunately, it appears that Weirick

did not carry out work on the U system and for this reason his Th work was chosen as a surrogate. In these experiments the oxide stoichiometry was  $\text{ThO}_2$  (PBR 1.35). An FE simulation of the Weirick data was constructed for this thesis and is detailed in Appendix B. By utilising Parise's method values of  $\xi_1^{pt} = 0.005$  and  $\xi_3^{pt} = 0.955$  were found. This value is the same in the lateral direction but is larger in the perpendicular direction than Parise, which would mean the stress within the oxide is less.

Chernia et al [77] used XRD data to calculate the strain in oxides of over 270 nm thickness. The strain ( $\xi$ ) of the oxide-layer is calculated using Equation 11,

$$\xi = \frac{(d - d_0)}{d_0} \quad (11)$$

where the strainless oxide-layer is  $d_0$  and the interplanar spacing of the strained oxide is  $d$ . By using these values Chernia calculates the anisotropic growth of the oxide-layer for a grain which is perpendicular to the surface, the values were  $\xi_1^{pt}=0.0145$  and  $\xi_3^{pt}=0.0093$ . The lateral stress is almost double both Parise and Weirick whilst the perpendicular direction is less, these both would mean the oxide is significantly more stressed.

The three different strain matrices discussed (Parise  $\text{ZrO}_2$ , Weirick  $\text{ThO}_2$ , Chernia  $\text{UO}_{2+x}$ ) were used to simulate an expanding oxide-layer up to a thickness of 64 nm (assuming they are  $\text{UO}_2$ ). These data are plotted in Figure 34 along with the isotropic  $\text{UO}_2$  oxide case.

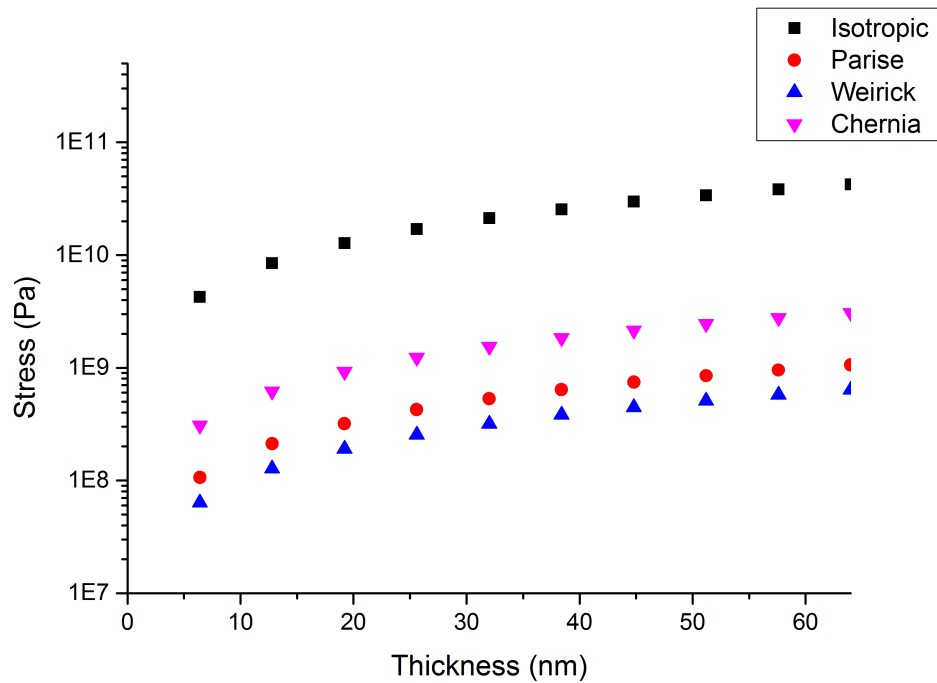


Figure 34: Calculated stress on the oxide surface for a 64 nm oxide assuming i) isotropic growth and anisotropic growth based on anisotropic strain tensors derived from data of ii) Parise for ZrO iii) Weirick for  $\text{ThO}_x$  and iv) Chernia for  $\text{UO}_2$

As can be seen the calculated stress for the isotropic system reaches 42 GPa at 64 nm and this is at least an order of magnitude greater than for the Chernia (3.1 GPa), Parisse (1.0 GPa) and Weirick (0.64 GPa) for the same oxide thickness. As a result of this analysis the Chernia anisotropic strain matrix was chosen for further simulations as it was taken from experimental data on  $\text{UO}_{2+x}$  whilst the other methods were based on surrogate materials. Future uranium flexure bending experiments allied with an FE model would allow further investigation of such strain variables.

### 3.1.2 Failure of the oxide

There are a number of mechanisms by which the oxide-layer can fail on a macroscopic scale, distinct from relaxation mechanisms: these are compressive, shear and tensile stress. As uranium dioxide is a ceramic it has an ultimate strength in compression much larger than in tension [30]. This is because compressive stresses inhibit the propagation of cracks through the ceramic and therefore limit the crack's development.

Compressive strength for  $\text{UO}_2$  (pellets) has been shown to be dependent on grains size as shown in Figure 35 with the compressive strength increasing with decreasing grain size [30]. The available data is somewhat variable for grain sizes over  $5 \mu\text{m}$ . XRD analysis of the oxide films that this thesis is comparing to suggests a crystallite size of 9-17 nm with a mean of 13 nm [85]. Other recent data provided by Petherbridge [86] suggests a grain size of 12 nm from TEM measurements.

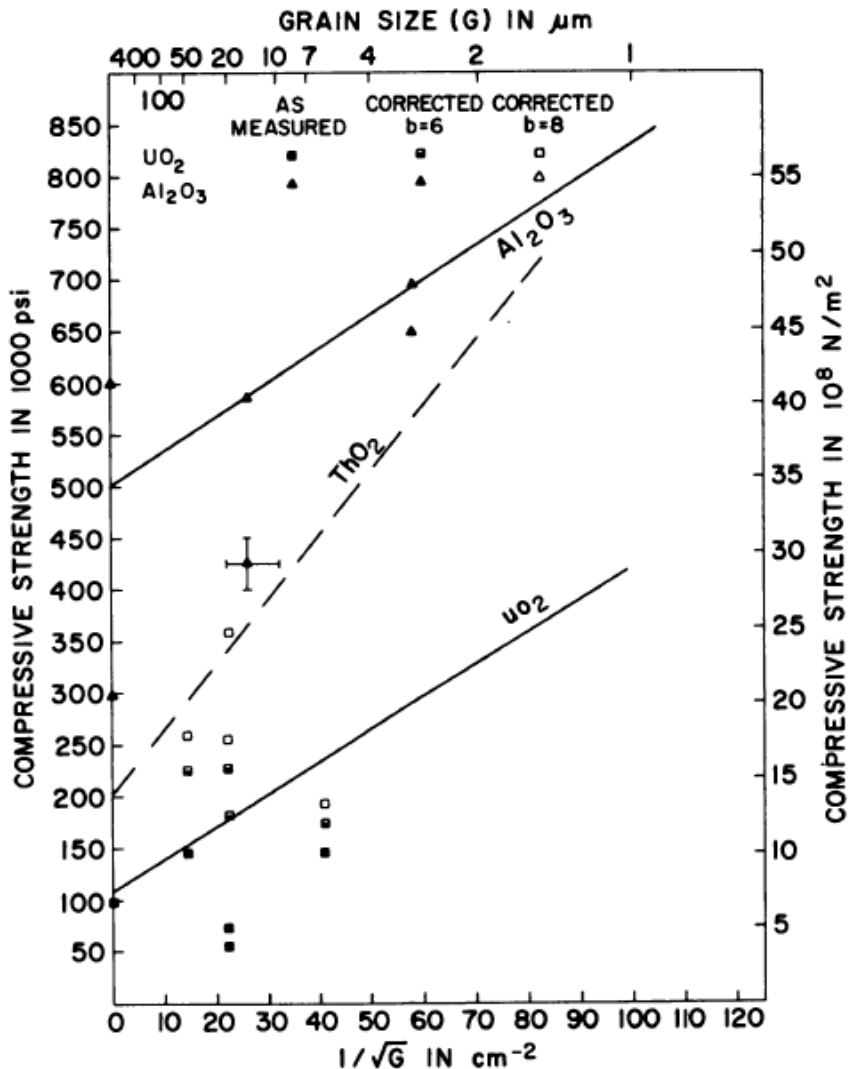


Figure 35: The compressive yield stress of  $\text{UO}_2$  against the grain size, a fitted line to the data is calculated by Rice [30].

If we assume extrapolation of grain size vs compressive stress in Figure 35 is correct and extrapolate to 10 nm this predicts a compressive strength of 20 GPa. This value is much larger than expected and this is most likely due to the data being extrapolated from only three data points and by a factor of

a hundred. Therefore, the error involved in this value is extremely large and should only be taken as a rough guide, when compared to other materials the compressive strength is more likely to be in the region of 5 GPa. On the grounds that this compressive strength was greater than all the predicted compressive stress levels in the oxide (except for that of the isotropic oxide), failure in compression was considered unlikely and was therefore not included.

Another potential method of failure is through the delamination of the oxide-layer [87]. This occurs when the shear stress of the oxide-layer in relation to the shear stress in the uranium beneath it are in opposite directions, and large enough that the oxide-layer shears off, shown in Figure 36.

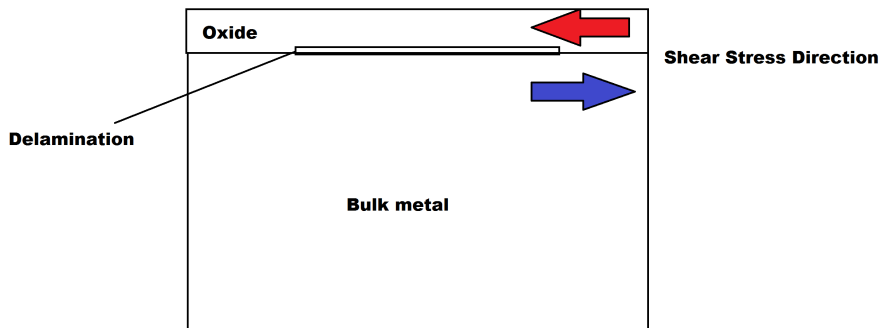
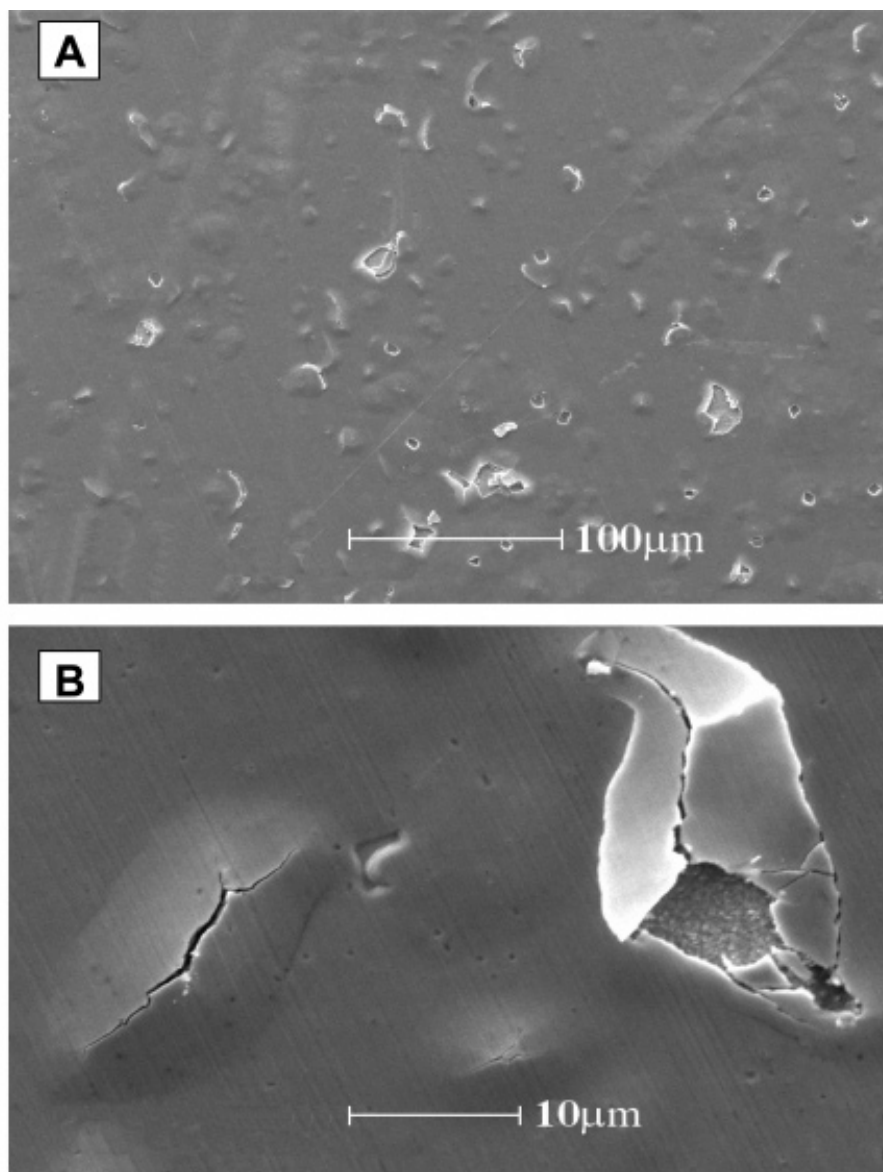


Figure 36: Schematic showing delamination as a potential failure mechanism for the oxide-layer

For the U/UO<sub>2</sub> system there is little data available, Chernia found that delamination of the oxide occurs for thick oxide-layers in the region of 500 nm (after oxidation at 130°C for 30 hours) and an example micrograph is shown in Figure 37. Figure 37(B) shows that a portion of the oxide has fallen away due to delamination.

Given the lack of data on delamination of  $\text{UO}_2$  for oxide scales of  $\sim 60$  nm, and the fact that the rate of oxidation was known to be in the parabolic region, for the samples of interest here, delamination is considered to be unlikely and again will not be considered in the model.



The last method of failure discussed in this work is tensile failure. This

Figure 37: Image showing delamination as a potential failure mechanism for the oxide-layer [77]

is when the tensile stress is large enough that the  $\text{UO}_2$  fractures. As noted earlier,  $\text{UO}_2$  is brittle and once the tensile yield stress is reached the oxide will fracture. There are three main studies on the tensile strength of  $\text{UO}_2$  and these studies are based on pellets which have a grain size of  $8\text{-}10 \mu\text{m}$ : three orders of magnitude larger than the grain size expected in this work ( $\sim 10 \text{ nm}$ ).

Knudsen et al [88] used flexural measurements from a three point bend to determine the flexural strength of uranium dioxide. Knudsen found at  $25^\circ\text{C}$  for a low porosity material with a grain size of  $10 \mu\text{m}$  the flexural strength was 103 MPa. Evans and Roberts [29] also used a three point flexure experiment to determine the flexure strength with a grain sizes of  $8 \mu\text{m}$  and they found at  $25^\circ\text{C}$  the results were 180 MPa and this flexure strength was constant up to  $400^\circ\text{C}$ . This gives confidence that these  $25^\circ\text{C}$  results are relevant to the model conditions of  $80^\circ\text{C}$ . Finally Canon et al [32] used a four point flexure experiment to determine the flexure strength with a grain size of  $8 \mu\text{m}$  and 3% porosity and found the flexure failure point to be 105 MPa.

Four point flexure methods are reportedly more reliable than a three point test since a much larger area of the oxide is stressed [89]. This gives a more reliable average of the flexure strength and is preferred in brittle materials. On these grounds Canon would appear to have the more reliable set of data.

No data was found for grain size smaller than  $8 \mu\text{m}$  but both Evans and Knudsen established that with smaller grain sizes the flexure strength

increased whilst Canon was not able to determine a clear link between grain size and flexure strength. The data has been collated together in Figure 38 and a possible extrapolation of the data is shown with a dotted line. This value was extrapolated from very few data points and over three orders of magnitudes. Therefore, the error involved in this value is extremely large and should only be taken as a rough guide, therefore in further work the number and the maximum extrapolated data were both included.

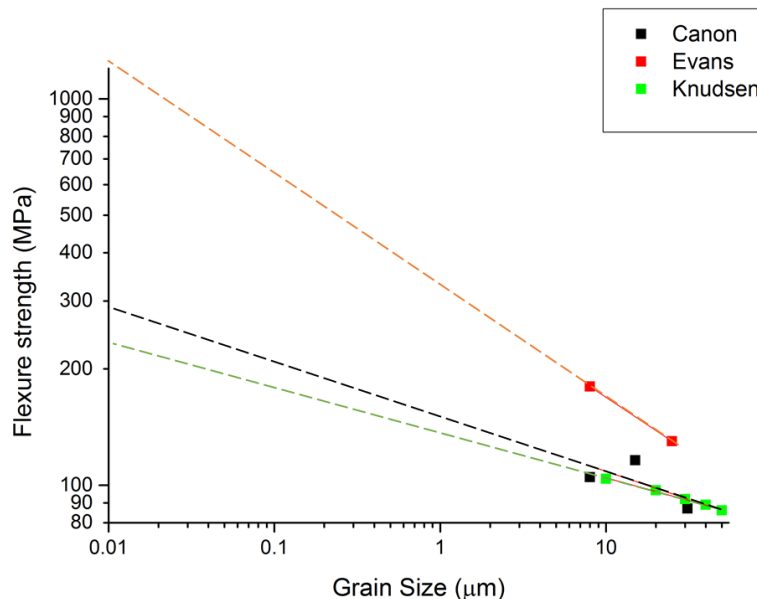


Figure 38:  $\text{UO}_2$  flexure failure for different grain sizes from work by Canon, Evans and Knudsen [32] [29] [88].

There is so little data about small grains that it is possible failure could occur either at 105 MPa if grain size is not a factor or between 230-1100 MPa if the extrapolation is correct.

A further influence on the tensile strength is the amount of hydrogen

which is dissolved within the oxide. Westlake [90] has shown that this influence the yield point in the Zr/ZrO<sub>2</sub> system.

From the studies discussed above the UO<sub>2</sub> layer is unlikely to fail due to compressive or shear stress. This would suggest that the most likely mechanism of oxide failure would be when the oxide is in tension. For these reasons the model does not include compressive or shear failure of the oxide but does include tensile failure when the stress exceeds a yield point of 105 or 1100 MPa.

It should also be noted that the majority of relevant materials data is from UO<sub>2</sub> samples while this system considers a thin UO<sub>2+x</sub> oxide-layer on a U sample. As a result the properties of the overlayer may be further influenced by the nature of the oxide-metal interface. The real U-UO<sub>2</sub> interface will probably contain roughness, forming local residual stresses within the oxide-layer [91]. Early simulations were run to predict the influence of surface roughness. These simulations produced local compressive stresses within the troughs, and tensile regions on the peaks, of the uranium with stresses within the oxide-layer varying by as much as  $\sim$ 1 GPa. Due to the additional complexity in modelling such undulations the effect of interface roughness was decided to be outside the scope of this project and left for future work.

### 3.1.3 Summary: Modelling the oxide

The oxide-layer was modelled with four key assumptions:

- There are no stress relaxation mechanisms operating within the oxide-layer over the time scale of the hydrogen reaction.

- The growth of the oxide-layer is anisotropic with  $\xi_1^{pt}=0.0145$  and  $\xi_3^{pt}=0.0093$  as per the results of Chernia [77]
- Failure of the oxide-layer only occurs when the tensile stress exceeds the yield stress at 105-1100 MPa [32].
- The metal-oxide has no surface roughness.

### 3.2 Modelling the uranium hydride

Bloch and Mintz have reported that for nuclei growing under a surface passivation layer the growth rate of most nuclei is approximately isotropic producing near circular patterns when observed by microscope [38], an example of this is shown from their experiment in Figure 39. An exception to this is when nuclei grow along grain boundaries and near inclusions (Section 1.5). Powell has also argued that the growth should be isotropic because uranium has a low saturation level of hydrogen [9]. From this reasoning the nucleation of the hydride in the simulations was assumed to be nucleated equally across the whole of the hydride. Whilst as this thesis is interested in the pre-induction size of the hydride ( $\sim 0.5 \mu\text{m}$  diameter) it is assumed that there is a coherent  $\text{UH}_3/\text{U}$  interface.

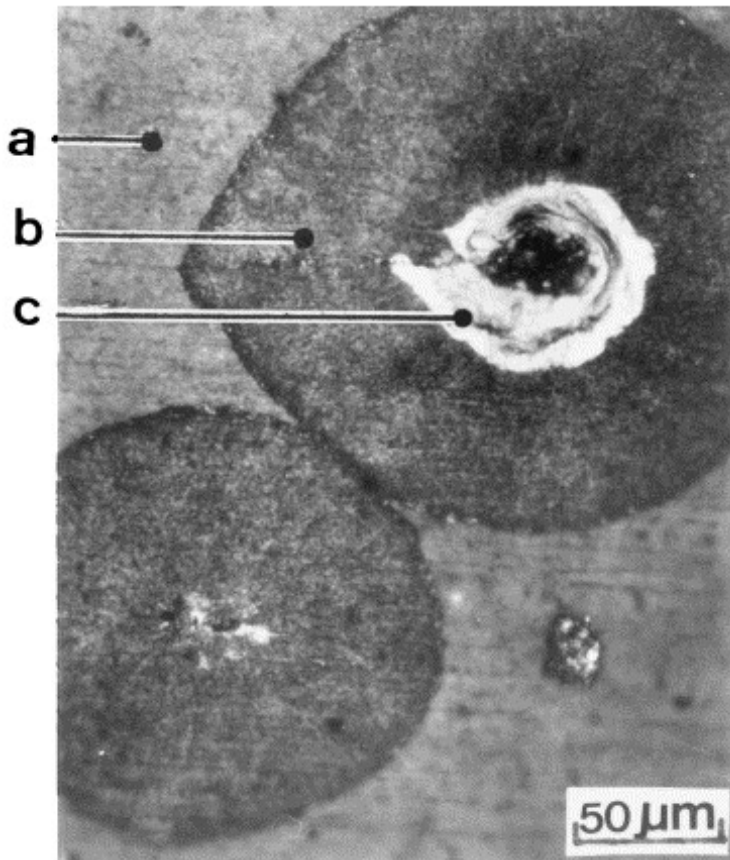


Figure 39: An image which indicates hydride growth is isotropic a)metal b) hydride growth c)initial hydride [38]

The chemical reaction of the  $\text{UH}_3$  formation is exothermic, so that an excess of energy is released into the surrounding environment increasing the temperature. A temperature increase may effect stress distribution or hydrogen transport properties and so it was important to understand how much heat could be released into the local uranium metal after precipitation. The effect of temperature was tested using a 3D model for a  $1 \mu\text{m}$  diameter hydride grown over 30 seconds in an infinite bulk. The simulation concluded that the temperature produced by such a nucleation due to chemical effects

will raise the temperature by 0.16°C at the UH<sub>3</sub>/U interface. Such a temperature rise is assumed to have insignificant effect on materials properties. Further details for this model can be found in Appendix C.

Misfit strain is the prominent method of simulating the nucleation of a hydride in Finite Element Analysis (FEA)[92] [93] [94]. A misfit strain occurs when the distance between the uranium atoms in the U bulk metal and UH<sub>3</sub> are different. Greenbaum [56] calculated the UH<sub>3</sub>/U misfit to be 0.2 from data collected by Rundle [95]. Since U is orthorhombic it means there are 4 potential U-U distances for U. Greenbaum's choice of misfit is based on the largest of the misfit strains. The simulations for this project will use the same logic and misfit strain of 0.2.

The hydride will be modelled as a hyper elastic material. As a hyper elastic material the hydride is assumed to be entirely in the elastic regime. A UH<sub>3</sub> is a ceramic and will be under compression there is an assumption no plasticity or fracture. This method has been successfully used in modelling hydrides previously [57].

This model calculates the stresses within the material by using the St-Vincent Kirchoff hyper elastic method in Equation 12 where W<sub>s</sub> is the strain energy density

$$W_s = \frac{\lambda}{2}(\epsilon)^2 + \mu(\epsilon)^2 - 2(\epsilon) \quad (12)$$

where  $\lambda$  is the first lame parameter and  $\mu$  is the second lame parameter. Both of these lame parameters are calculated from the bulk and shear modulus of uranium hydride and  $\epsilon$  is the strain which is calculated through an increase in temperature which is set to produce a 20% increase in strain through

Equation 13

$$\varepsilon = \alpha(T - T_{ref}) \quad (13)$$

where  $\alpha$  is the coefficient of volume expansion (set to 0.1),  $T$  is the change of temperature and  $T_{ref}$  is the reference temperature (which is 0). In this way when the simulation reaches a 2°C increase in temperature a 0.2 strain is applied throughout the hydride.

### 3.2.1 Summary: Modelling the hydride

The hydride growth is modelled with four key assumptions:

- The hydride is considered a coherent hyper-elastic material.
- There are no temperature effects due to the hydride nucleation.
- The U:UH<sub>3</sub> couple has a misfit strain of 0.2.
- There is an assumption of no plasticity or fracture in the hydride.

## 3.3 Uranium metal

In preliminary simulations uranium was modelled as having isotropic material properties. However, to account for the fact that uranium has an orthorhombic unit cell anisotropic conditions have been included. This data was taken from Table 1 and added to the model using an anisotropic matrix shown in Figure 3.3

$$\begin{pmatrix} c_{11} & c_{12} & c_{13} & 0 & 0 & 0 \\ c_{21} & c_{22} & c_{23} & 0 & 0 & 0 \\ c_{31} & c_{32} & c_{33} & 0 & 0 & 0 \\ 0 & 0 & 0 & c_{44} & 0 & 0 \\ 0 & 0 & 0 & 0 & c_{55} & 0 \\ 0 & 0 & 0 & 0 & 0 & c_{66} \end{pmatrix}$$

Figure 40: Anisotropic Strain Matrix

### 3.3.1 Plasticity

The sample can be further refined with the inclusion of uranium metal plasticity. Plasticity can be increased in complexity from perfect, to isotropic to anisotropic plasticity. Greenbaum did not note which plasticity method he used or if plasticity was utilised in his models.

Plasticity was initially modelled through the perfectly plastic mechanism so that once the yield limit is reached isochoric (constant volume) plastic deformations occur. This is the simplest method of modelling plastic deformation as the only data required is the yield stress, models found in the Appendices use perfect plasticity. A more sophisticated description of plasticity is given by isotropic plasticity. The effect of these on the stress strain matrix is shown in Figure 41.

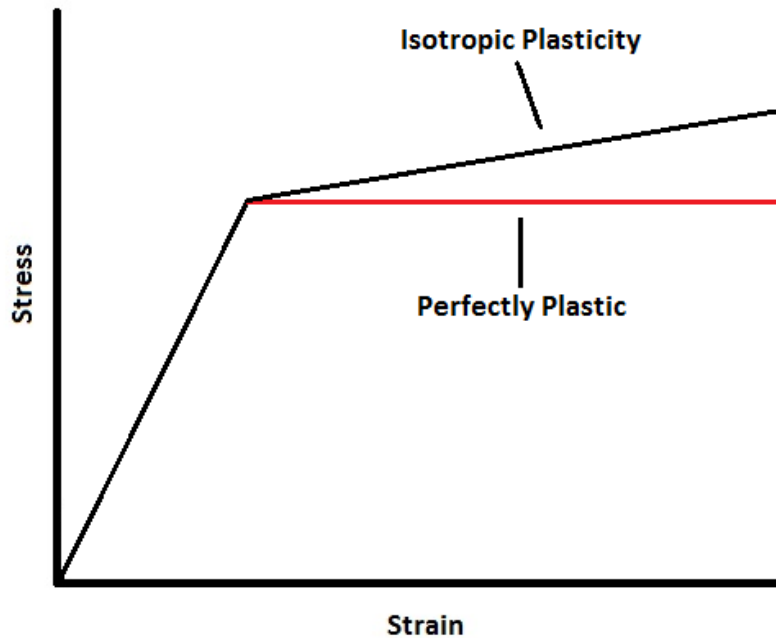


Figure 41: Simplified stress strain behaviour showing the inclusion of perfect and isotropic plasticity.

A stress strain curve for uranium at room temperatures as measured by Knezevic et al [96] is shown in Figure 42. The data is available to 0.2 strain, after which perfectly plastic strain was assumed.

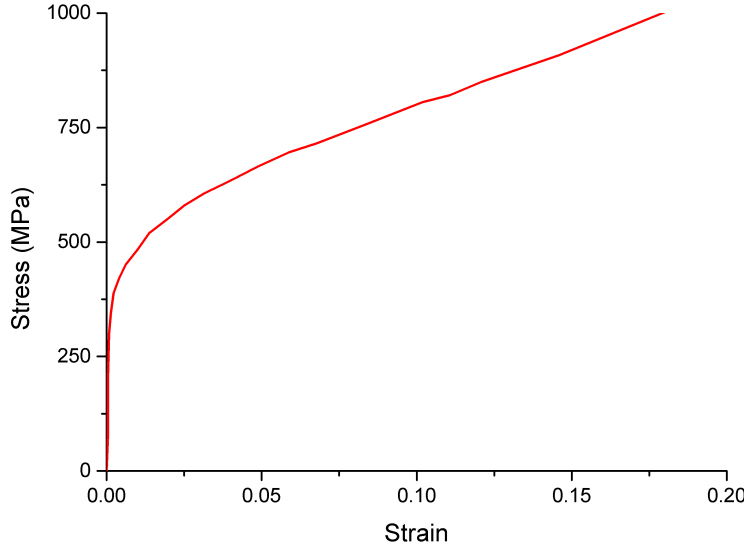


Figure 42: Stress-strain curve for uranium [96]

When using perfect or isotropic plasticity, the model calculates the Von Mises stress ( $\sigma_{vonmises}$ ) through Equation 14 and compares it to the yield point of 230 MPa. In Equation 14  $\sigma_{11}\sigma_{22}\sigma_{33}$  are the principal stresses and  $\sigma_{12}\sigma_{23}\sigma_{31}$  are the shear stresses. The difference between the calculated Von Mises stress and the yield point is used to determine the amount of plasticity which occurs.

$$\sigma_{vonmises} = \sqrt{\frac{1}{2}(\sigma_{11} - \sigma_{22})^2 + (\sigma_{22} - \sigma_{33})^2 + (\sigma_{33} - \sigma_{11})^2 + 6(\sigma_{12}^2 + \sigma_{23}^2 + \sigma_{31}^2)} \quad (14)$$

Uranium is, however, a base-centred orthorhombic structure with the result that plasticity is highly anisotropic [97]. Hill [98] has devised an ex-

tension to the Von Mises criterion as shown in Equation 15 where F, G, H, L, M, and N are parameters which describe the plasticity.

$$F(\sigma_y - \sigma_z)^2 + G(\sigma_z - \sigma_x)^2 + H(\sigma_x - \sigma_y)^2 + 2L\sigma_{yz}^2 + 2M\sigma_{zx}^2 + 2L\sigma_{xy}^2 = 1 \quad (15)$$

Data on likely values for these parameters is sparse; however Knezevic has reported on F (280 MPa) and G (305 MPa) [31]. Parameters H, L and M were due to the lack of published data, assigned the value of the average uranium metal yield stress (230 MPa). In the case of anisotropic plasticity, the model again calculates principle and shear stresses and compares it to the hill yield condition in order to determine the extent of plastic deformation. Models found in Sections 4.2-6 use anisotropic plasticity within the uranium metal.

### 3.3.2 Summary: Modelling the uranium metal

The uranium metal is modelled with two key assumptions:

- The metal is anisotropic and the data used is from Table 1.
- Plasticity occurs through the Hill orthorhombic method.

## 3.4 Finite Element Analysis

More details about the finite element method for solid mechanics can be found by Zienkiewicz [99].

### 3.5 COMSOL Calculations

#### 3.5.1 Stress calculations

Full details of the method COMSOL(version 4.4) uses to calculate the stresses can be found elsewhere [100]. A brief explanation of the calculations is given here.

Fundamental to the calculations is the relationship between the strain tensor,  $\epsilon_{mn}$  to the displacement gradient,  $\frac{1}{2}(\frac{\delta u_m}{\delta u_n} + \frac{\delta u_n}{\delta u_m})$

$$\epsilon_{mn} = \frac{1}{2}(\frac{\delta u_m}{\delta u_n} + \frac{\delta u_n}{\delta u_m}) \quad (16)$$

For the elastic case (oxide) the Duhamel-Hooke's (Equation 17) law is used to calculate the final stress,  $s$ .

$$s = s_0 + C(\epsilon - \epsilon_0) \quad (17)$$

This is calculated from the original stress  $s_0$ , the strain  $\epsilon$  and the initial strain  $\epsilon_0$  calculated from Equation 16, where  $C$  is the Cauchy elasticity tensor.

When  $\text{UH}_3$  undergoes strain of 0.2 the surrounding uranium metal deforms. As the strain is greater than 0.05 the solver must implement a method called large plastic strain as shown in Equation 18. Where the mass density is  $\frac{dV}{dV_0}$  and  $F$  is the deformation gradient can be seen in Equation 18.

$$\frac{dV}{dV_0} = \frac{\rho_0}{\rho} = \det(F) \quad (18)$$

This is then related to the Cauchy-Green tensor via Equation 19.

$$C = F^T F \quad (19)$$

This tensor is then used to calculate the strain  $\epsilon$ .

$$\epsilon = \frac{1}{2}(F^T F - I) \quad (20)$$

A stationary solver was used in this simulation which undergoes an auxiliary sweep of the strain from 0-0.2 in 0.1 steps. The method of solving was a double dogleg with non-linear calculations and is described in the next section.

### 3.5.2 Solving double dogleg non-linear static equations

For these simulations the double dogleg solver was used. The double dogleg, developed by Dennis [101], combines the Newton-Raphson and steepest descent methods.

First the steepest decent method is used. This moves from the point on the graph  $X_{initial}$  to  $X_{initial+1}$  and continues this step in the direction of the lowest gradient. This method is slow but guarantees progress towards a minimum unlike the Newton-Raphson method which is inaccurate at points far away from the solution. Once within a certain distance from the solution the quicker Newton-Raphson is used, which is a root-finding algorithm that utilises a Taylor series. The previous solution from the steepest method is used as the initial solution  $x_0$ . Equation 21 is then used to find another closer solution  $x_{n+1}$

$$x_{n+1} = x_0 - \frac{fx_0}{f'x_0} \quad (21)$$

where function  $fx_0$  and the function's derivative  $f'x_0$  are calculated. This process is then iterated until convergence at an approximate zero.

The main challenge for a non-linear structural mechanics problem is that the solution may not converge correctly. To reduce this probability the starting point for the strain is set to zero and the strain is slowly increased for each iteration; after each change in strain the previous solution is used.

### 3.6 Construction of the Model

To limit the amount of computer power required the symmetry of the hydride precipitate is exploited. An accurate model is built up by dividing up the hydride into symmetrical segments. Firstly the model was limited to a  $6 \times 3 \times 3 \mu\text{m}$  rectangle of uranium with the hydride positioned in the centre of the geometry. The model was split in half at the centre as shown in Figure 43a, then the model was split in half again, which is shown in Figure 43b and then finally the model was sliced down the middle as shown in Figure 43c to give a portion equal to one eighth of the model. This minimised the size of the model.

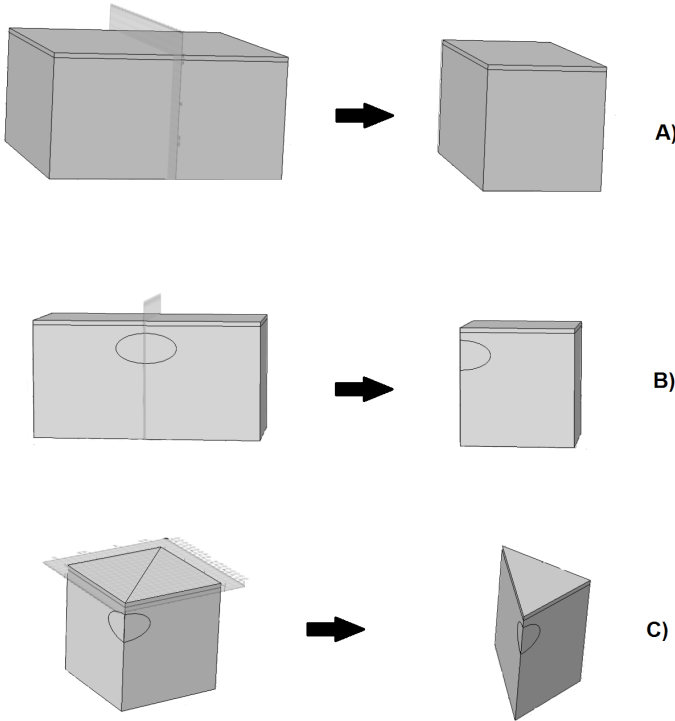


Figure 43: Splitting the geometry to exploit symmetry. The model was split in half at the centre as shown in (a), then the model was split in half again (b) and finally sliced down the middle in (c).

The boundary conditions of the model are shown in Figure 44 and are defined as follows:

- Symmetry. A geometric boundary which allows the model to be replicated.
- Fixed. The bottom of the model (uranium) is unable to move in any direction.
- Free. The top of the model is free to deform.

- Fixed in X and Y. The side of the model can only deform in the z direction.

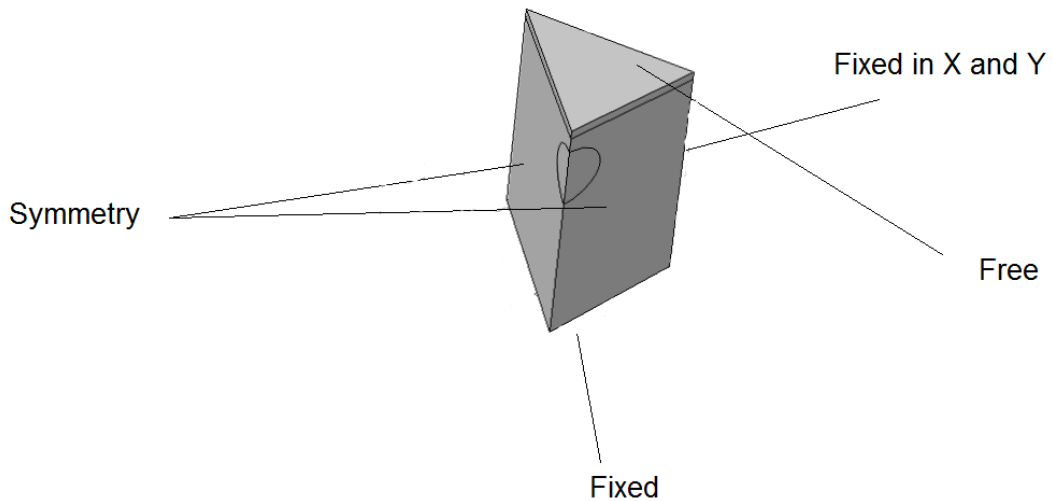


Figure 44: The boundary conditions on the model.

### 3.7 Mesh optimisation

Within any FE model, the confidence in the solution is dependent on the finite element mesh used in the simulation. This is because the mesh splits the geometry created into solvable elements which then represent the stress fields in the solution.

Previous work carried out by Greenbaum [57] used quadrilateral elements which contain eight integration points, one at each of the nodes. However the elements used in this work were second order tetrahedral, an example of

which is shown in Figure 45 (the integration points are indicated by black dots). In this element there is an integration point at each of the nodes and in the centre of the element. This type of element is able to mesh all geometries and is therefore extremely versatile when varying the shape and depth of the hydride within the uranium. Further to this the tetrahedral element is the only element within COMSOL that allows you to use adaptive mesh refinement, this allows COMSOL to remesh high stress areas.

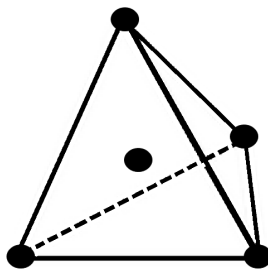


Figure 45: A tetrahedral mesh element, the black dots indicate the integration points.

Mesh refinement is used to optimise the mesh so that the areas of interest are the most accurate; the mesh density was manually increased around certain boundaries and geometries. This technique was particularly useful for the oxide-layer and around the hydride.

To ensure the mesh density was high enough a mesh sensitivity analysis was carried out on a single model ( $0.5 \mu\text{m}$  depth spherical precipitate) with a variation in the mesh size within the whole model. The stress in the oxide-layer directly above the  $\text{UH}_3$  precipitate was used as a probe to understand the model accuracy as a function of mesh size. The results are shown in

Figure 46 where the calculated stress is plotted against the number of degrees of freedom.

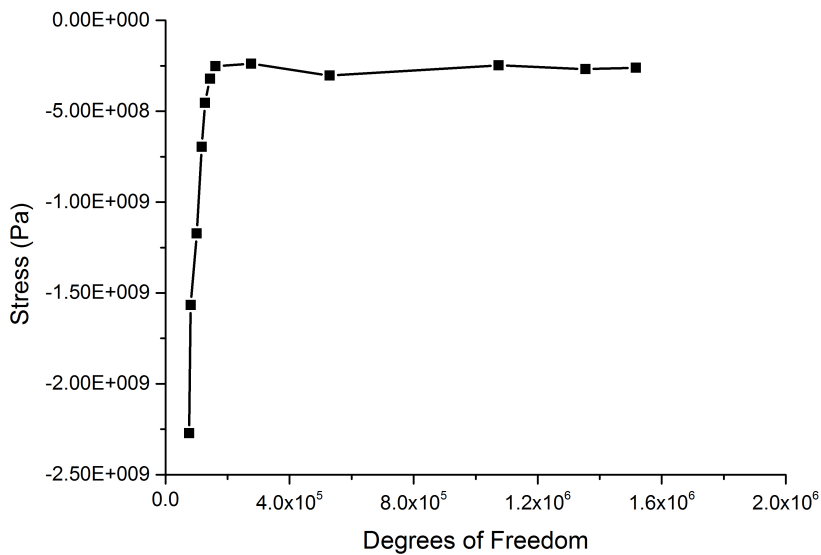


Figure 46: Mesh sensitivity analysis where the maximum stress of the oxide is plotted against the number of degrees of freedom within the model.

Mesh sensitivity analysis works by solving the model for different mesh sizes (degrees of freedom), initially starting at a low mesh density (low number of degrees of freedom) and then increasing the mesh density (more degrees of freedom). As the mesh density increases the compressive stress in the oxide decreases from around 2.3 GPa to around 0.23 GPa; increasing the mesh density further does not affect the calculated stress.. The optimal mesh density is a reliable output with the lowest number of degrees of freedom, as this requires the least amount of computing power. From this sensitivity analysis a mesh with  $4 \times 10^5$  degrees of freedom was the optimal mesh density, with

the final mesh properties used for future models shown in Figure 47 and Table 8..

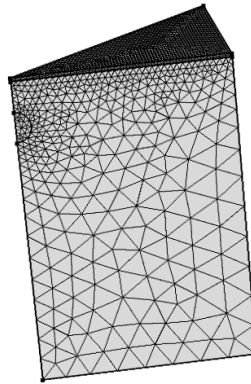


Figure 47: Final mesh used in the simulations.

Table 8: Mesh Element Properties

Material	No. elements	Max Growth Rate	Avg. element quality
UO <sub>2</sub>	1461	1	0.938
U	161646	3.605	0.7681
UH <sub>3</sub>	1039	2.818	0.6921

### 3.8 Post processing Calculations

Some calculations are used consistently throughout the results. These are listed below.

The hydrostatic stress  $\sigma_H$  was calculated using Equation 22,

$$\sigma_H = \frac{\sigma_{11} + \sigma_{22} + \sigma_{33}}{3} \quad (22)$$

where  $\sigma_{11}$ ,  $\sigma_{22}$  and  $\sigma_{33}$  are the principal stresses.

Total elastic strain energy (TESE) is the total stored energy within the model in units of  $\text{Jm}^{-3}$ . This parameter is calculated using Equation 23 with  $E_{tese}$  is the total elastic strain energy ,  $\sigma_{ij}$  is the elastic stress and  $\varepsilon_{ij}$  is the strain.  $\sigma_{ij}$  are the elastic stress  $\varepsilon_{ij}$  is the strain.

$$E_{tese} = \frac{1}{2} \int \sigma_{ij}\varepsilon_{ij}dV \quad (23)$$

### 3.9 Simulation uncertainty

The uncertainty of the simulation measurements are diverse and hard to quantify. The largest source of error involves the material properties chosen for the modelling and as discussed earlier this may have an impact on the absolute calculated stress of up to 40%. As a result of the experimental work (Section 2) uncertainty in the bulk modulus is now much reduced and the effect on the calculated stress is expected to be around 15%. Further errors are also involved in the simulations with inherent solving errors sometimes rising to as high as 5% of the simulation.

These and other these errors lead to a situation where the calculated results give a guideline to the stress formation and deformation but the exact figures could vary by as much as +/-50%. Therefore the verification methods used in this simulation are based on observations and trends that are common between experimental work and simulations. Appendix D describes a sensitivity analysis of varying the different properties followed by a test comparison between experimental AFM results and the deformation from the

model. The result of this was to show that this model provides a reasonable description of the stresses and deformation after sub-surface nucleation.

### **3.10 Modelling conditions**

Experimental data was used to determine the dimensions of the simulation. The size of the hydride was taken from Table 4 and had a diameter of  $0.5 \mu\text{m}$  and AFM work carried out at AWE [15] was used to determine the oxide-layer thickness to be 64 nm. The shape of the hydride was initially modelled as spherical which gives an understanding of a simple system, with the depth ( $0.5 \mu\text{m}$ ) measurement being taken from the top of the oxide-layer to the top edge of the uranium hydride before nucleation.

## 4 Stresses induced by the nucleation of $\text{UH}_3$

Previous finite element simulations [57] [56] have examined the stress generation of a hemi-spherical palladium hydride (0.034 misfit strain) directly under a non-stressed oxide-layer. This section aims to expand on this work and examine a spherical uranium hydride (0.2 misfit strain) nucleated at various depths under a pre-stressed oxide.

To examine this situation the model developed in Section 3 was modified to simulate the stresses produced when a spherical uranium hydride precipitate nucleates at depths varied from  $0 \mu\text{m}$  to  $2 \mu\text{m}$  beneath the pre-stressed oxide-layer. This was investigated to understand the influence a nucleated hydride at depth can have on the stress regions in the surrounding bulk metal and oxide-layer.

Unless otherwise indicated the simulations described in this section (with reference to Section 3.10) modelled an oxide thickness of 64 nm, and a spherical  $\text{UH}_3$  of diameter  $0.5 \mu\text{m}$  and the oxide stress measurements are in the plane of the material as the normal stress in the oxide is zero as it is a stationary free surface.. The first part of this section assumes the uranium metal is isotropic; anisotropy is introduced from Section 4.2.

### 4.1 Modelling of stress from a nucleated hydride with isotropic material properties

An image showing the calculated pressure for a  $0.5 \mu\text{m}$  spherical  $\text{UH}_3$  nucleated at a  $2 \mu\text{m}$  depth, assuming isotropic material properties is shown in

Figure 48. In Figure 48a is the cross section of the uranium metal and the oxide surface. The pressure scale has been truncated from -0.5 GPa (tensile) to 0.5 GPa (compressive) in the cross section to view the pressure range in greater detail. Greater compressive stress than this can be found in the uranium surrounding the hydride precipitate. In Figure 48b is a bird's eye view of the oxide surface directly above the hydride precipitate, the pressure on the oxide over-layer has not been truncated. The normal stress in the oxide is zero as it is a stationary free surface.

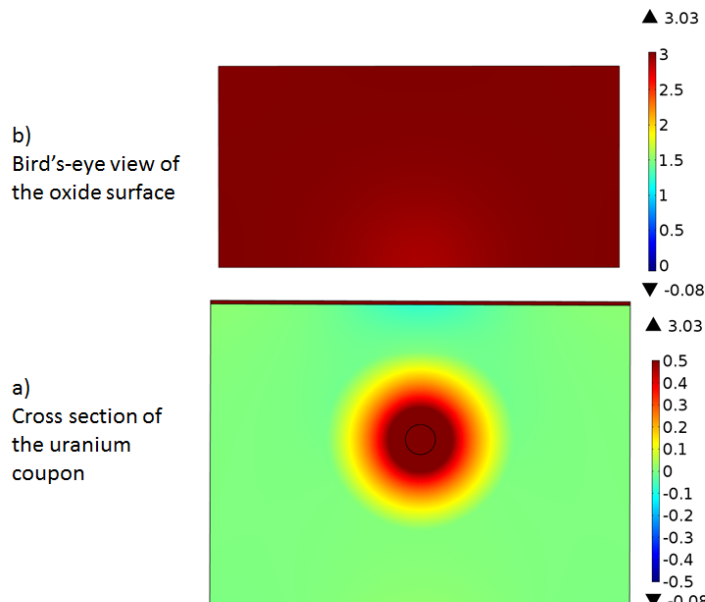


Figure 48: Images showing the pressure generated due to a  $0.5 \mu\text{m}$  diameter spherical  $\text{UH}_3$  nucleated at a  $2 \mu\text{m}$  depth, assuming isotropic material properties. a) Cross section of the whole model; b) bird's-eye view of the oxide surface.

The initial size of the hydride precipitate is shown by a black circle. The pressure at the  $\text{UH}_3/\text{U}$  interface is 0.85 GPa compressive and is equal in all

directions, this stress then decreases at a relatively constant rate until at a distance of  $\sim 1.3 \mu\text{m}$  the pressure is negligible. The oxide over-layer and hydride have minimal effect on each other's stress when the precipitate is at this depth. In the case where a  $\text{UH}_3$  is not present the metal experiences a tensile stress in the immediate sub-surface. In this case however a slight tensile stress of -0.08 GPa in the uranium just beneath the oxide surface directly above the precipitate. The deformation on the oxide over-layer is negligible

Below in Figure 49 is an identical nucleation at a depth of  $0.5 \mu\text{m}$  (i.e. much closer to the surface).

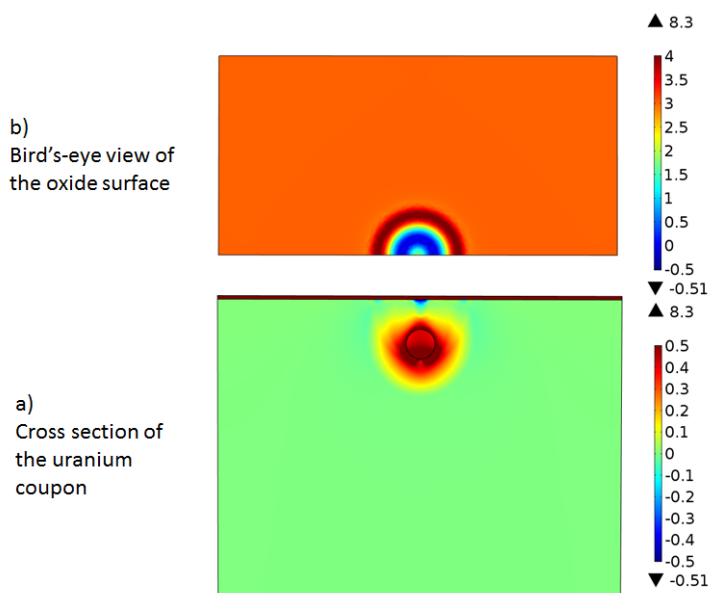


Figure 49: Images showing the pressure generated due to a  $0.5 \mu\text{m}$  diameter spherical  $\text{UH}_3$  nucleated at a  $0.5 \mu\text{m}$  depth, assuming isotropic material properties. a) Cross section of the whole model; b) bird's-eye view of the oxide surface.

When the nucleation takes place this close to the surface there is a significant interaction between the  $\text{UO}_2$  and  $\text{UH}_3$  stress regions. In the x-y directions around the hydride there is the same decreasing compressive stress region at 0.85 GPa reaching zero at  $\sim 1.2 \mu\text{m}$  in the x-direction. Above the precipitate and closer to the surface this compressive region is more concentrated and decreases to zero over  $\sim 0.9 \mu\text{m}$  in the x-direction. Further, this compressive region appears somewhat hemi-spherical and contains a small tensile region. On the oxide-layer there are concentric rings with the centre point under compression (1 GPa) followed by rings of tension (-0.1 GPa) and compression (4 GPa) before returning to parity with the rest of the oxide-layer. In each case a reduction or increase in oxide compression is related to the stress in the near surface metal.

To enable a comparison with modelling work by Greenbaum [57] a new simulation was created. In this simulation (i)the oxide layer was removed, (ii)the uranium properties were isotropic with no plasticity and (iii) the hydride was moved to a  $0.1 \mu\text{m}$  depth (even closer to the surface). Other than these changes the same  $\text{U}/\text{UH}_3$  properties were used and the results are shown in Figure 50.

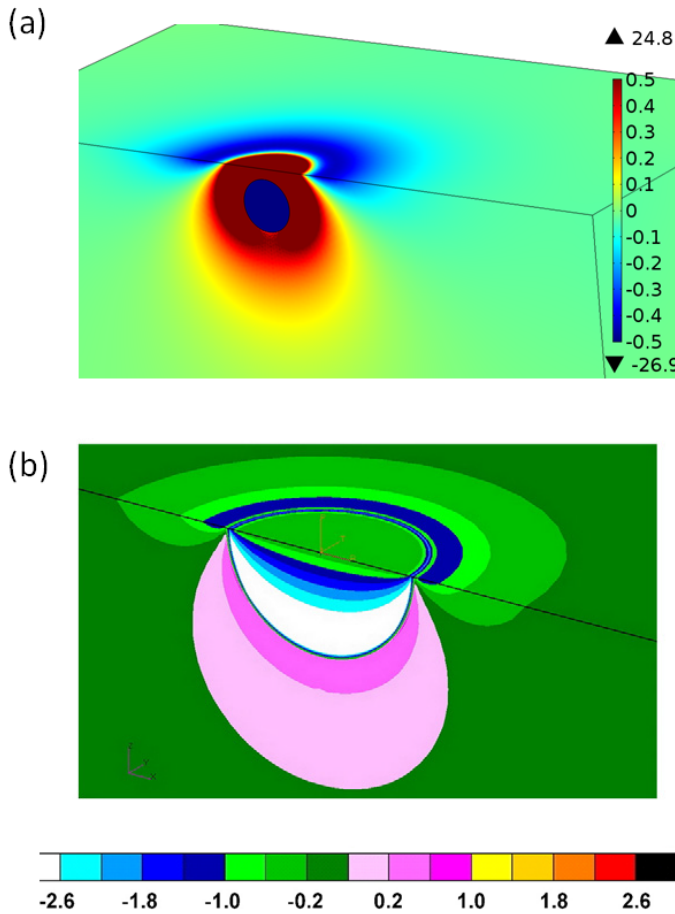


Figure 50: Stress map of (a) a U/UH<sub>3</sub> with no oxide, isotropic uranium properties with no plasticity and at a depth of 0.1  $\mu\text{m}$  (b) semi-spherical Pd-PdH<sub>x</sub>hydride particle tangent to the free surface with no oxide, isotropic with no plasticity [57].

Similarities between these two simulations are found through the shape of the compression region beneath the hydride: this region expands out more in the z direction than the x direction. Further to this on the surface similar stress rings are found, with an inner region above the hydride followed by a high tensile stress surrounding it. The differences are that the inner

region is compressive in (a) whilst slightly tensile in (b). This is probably due to the spherical precipitate in (a) being at a slight depth as compared to a hemispherical precipitate in (b) at the free surface. Which means that in (a) the surface is the uranium metal while in (b) the surface is the precipitate. Furthermore the magnitude of the tensile stress is different probably because of the different material properties of the two simulations; U/UH<sub>3</sub> and Pd/PdH<sub>x</sub> respectively.

These results give extra confidence in the simulations in this work as the trends found in the Figure 50 simulation (no oxide, no plasticity, isotropic) are similar to those found previously by Greenbaum [57]

## **4.2 Modelling of stress from a nucleated hydride with anisotropic material properties**

Anisotropic material properties for uranium metal have been added to the model as described in Section 3.3. The orientation of the bulk uranium in these models is equivalent to orienting the [001] plane parallel to the surface which was the orientation most commonly found within the uranium by Carpenter [102].

The simulation of the basic spherical 0.5 μm diameter UH<sub>3</sub> at 2 μm depth is shown in Figure 51. The pressure scale has been truncated from 0.5 GPa (compressive) to -0.5 GPa (tensile) to enable a uniform scale which displays the tensile and compressive regions clearly.

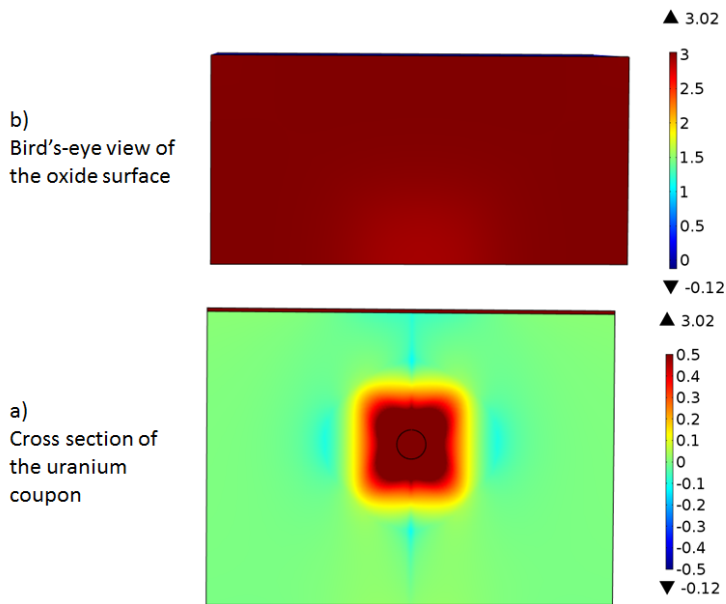


Figure 51: Images showing the pressure generated due to a 0.5  $\mu\text{m}$  diameter spherical UH<sub>3</sub> nucleated at a 2  $\mu\text{m}$  depth, assuming anisotropic material properties. a) Cross section of the whole model; b) bird's-eye view of the oxide surface.

The stresses surrounding the hydride form a compressive rectangular region of 1.45 GPa at the UH<sub>3</sub>/U interface, as before the compressive stress reduces with distance from the UH<sub>3</sub> precipitate. This cuboid is surrounded by regions of tensile stress (-0.1 GPa) in the x,y and z orthogonal directions. By 2  $\mu\text{m}$  distance from the UH<sub>3</sub> the stress approaches zero. The tensile regions are semi-spherical in shape. In the 45° angles between the orthogonal directions the compressive stress decays to zero with no tensile regions formed.

When this result is compared to the isotropic case the similarities relate to the general shape and form of the compressive region around the hydride, with the isotropic compressive region being spheroidal and the anisotropic

compressive region being cuboidal. Further more there are no tensile regions in the isotropic case. Once again at this depth there is no interaction between the stress fields of the precipitate and the oxide.

The same  $\text{UH}_3$  precipitate again was placed at a depth of  $0.5 \mu\text{m}$  (much closer to the surface) and is shown in Figure 52.

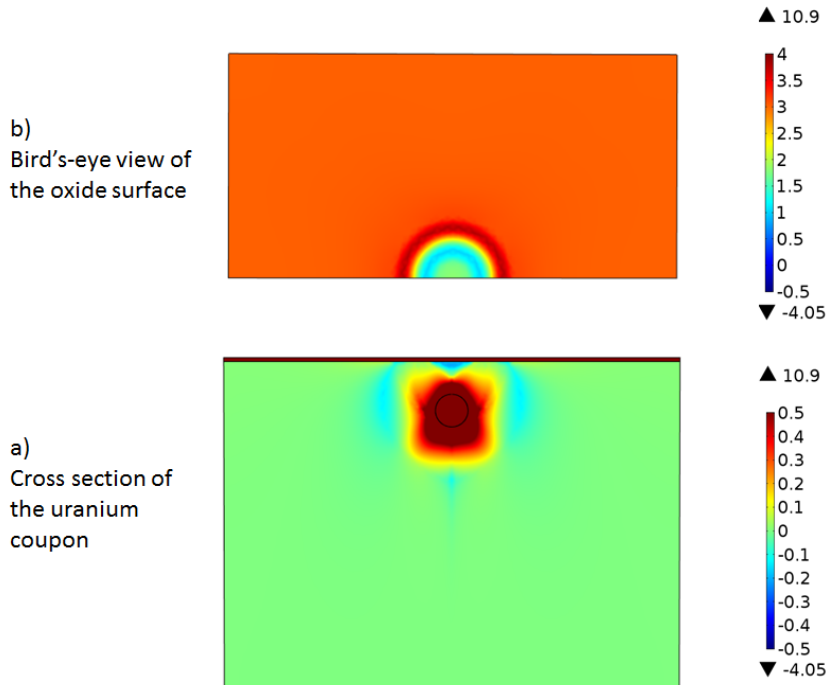


Figure 52: Images showing the pressure generated due to a  $0.5 \mu\text{m}$  diameter spherical  $\text{UH}_3$  nucleated at a  $0.5 \mu\text{m}$  depth, assuming anisotropic material properties. a) Cross section of the whole model; b) bird's-eye view of the oxide surface.

Again a compressive region is evident at the  $\text{UH}_3/\text{U}$  interface of 1.5 GPa and this reduces with distance from the  $\text{UH}_3$ . The tensile regions on the edge of the compressive region are greater (-0.12 GPa) as compared to the previous example. Similarly, tensile regions can be found in the orthogonal

directions whereas directly in-between the orthogonal directions no tensile stress is observed. These tensile regions are highlighted in Figure 53 where only the tensile stress regions are visible (-0.01 to -0.5 GPa).

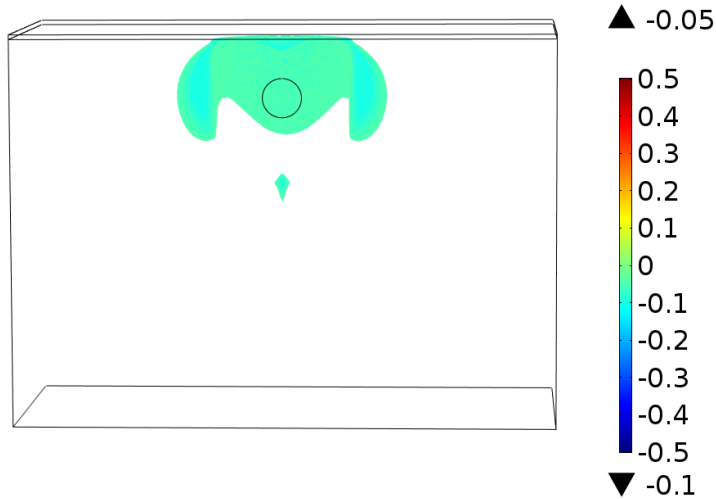


Figure 53: Image showing the tensile region generated due to a  $0.5 \mu\text{m}$  diameter spherical  $\text{UH}_3$  nucleated at a  $2 \mu\text{m}$  depth, assuming anisotropic material properties.

On the oxide surface there are two concentric rings of stress expanding from the centre (1 GPa compressive surrounded by a ring of 3.8 GPa compressive). This is similar to the isotropic case except in the isotropic uranium the inner stressed region is tensile(-0.1 GPa).

### 4.3 Modelling different depths of nucleated hydrides

An important topic of debate is the depth at which  $\text{UH}_3$  is likely to nucleate. The depth of nucleation may be influenced by the effect that the nucleation at any given depth has on surrounding bulk uranium metal and oxide-layer.

The anisotropic model was used to simulate  $\text{UH}_3$  at different depths within the uranium bulk, at 0  $\mu\text{m}$ , 0.25  $\mu\text{m}$ , 0.5  $\mu\text{m}$ , 1  $\mu\text{m}$ , 1.5  $\mu\text{m}$  and 2  $\mu\text{m}$ . These simulations used a 0.5  $\mu\text{m}$  diameter spherical hydride beneath a 64 nm pre-stressed oxide. The depths are defined as the distance from the top of the hydride to the  $\text{U}/\text{UO}_2$  interface. The 2  $\mu\text{m}$  and 0.5  $\mu\text{m}$  examples were previously discussed in Figures 51 and 52(Section 4.2).

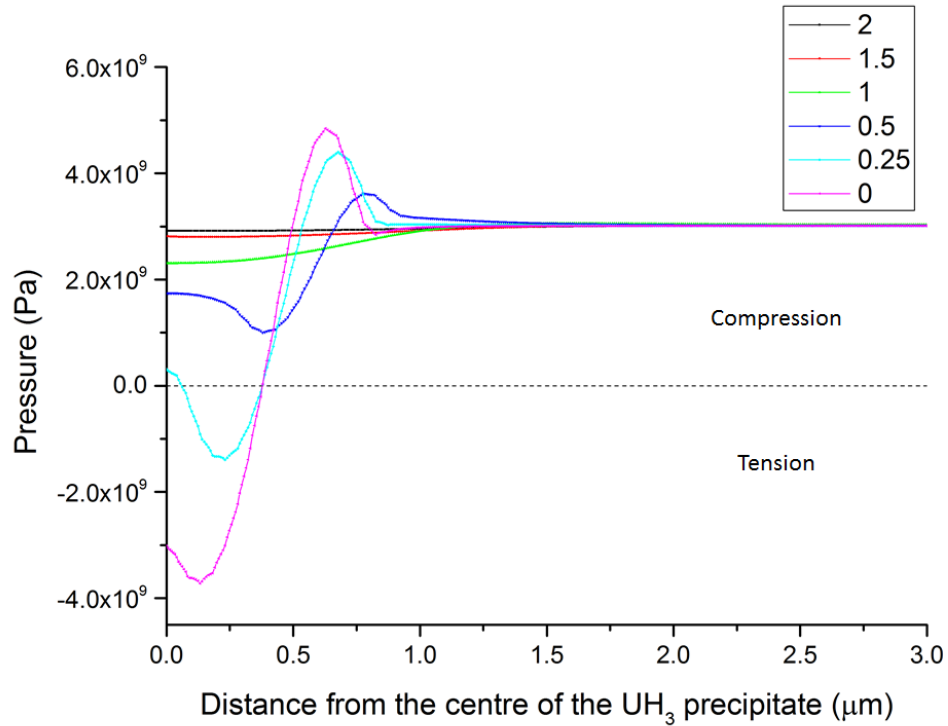


Figure 54: The pressure within the oxide-layer taken from the centre of the simulation to a distance of 3  $\mu\text{m}$  in the x direction for precipitate depths of 0  $\mu\text{m}$ , 0.25  $\mu\text{m}$ , 0.5  $\mu\text{m}$ , 1  $\mu\text{m}$ , 1.5  $\mu\text{m}$  and 2  $\mu\text{m}$ .

In Figure 54 the pressure at the oxide surface from a position directly

above the hydride to a distance of  $3 \mu\text{m}$  in the  $x$  direction is shown for six different  $\text{UH}_3$  precipitate depths. The normal stress in the oxide is zero as it is a stationary free surface.

When the  $\text{UH}_3$  is at a depth of  $2 \mu\text{m}$  (deepest) the oxide compressive stress directly above the hydride is slightly reduced from the normal oxide stress from  $3 \text{ GPa}$  to  $2.96 \text{ GPa}$  compression.

When the  $\text{UH}_3$  is moved to a depth of  $1 \mu\text{m}$  the compressive oxide stress is reduced further to  $2.68 \text{ GPa}$  and reaches parity with the normal oxide stress at a distance of  $1.1 \mu\text{m}$  from the hydride position.

If the simulation is run with the  $\text{UH}_3$  at a depth of  $0.25 \mu\text{m}$  the compressive stress directly above the centre of the hydride is now considerably reduced to around  $0.6 \text{ GPa}$  (i.e.  $20\%$  of its normal oxide value). This region is now surrounded by a ring of tensile stress at a distance of  $0.2 \mu\text{m}$  and reaches a peak tensile stress of  $-1.3 \text{ GPa}$ . Outside of this region the oxide stress is under compression and reaches parity with the "normal oxide"  $1.3 \mu\text{m}$ .

Finally, for the case where the  $\text{UH}_3$  is  $0 \mu\text{m}$  from the surface the oxide directly above the centre of the  $\text{UH}_3$  is now in greater tension at  $-3 \text{ GPa}$ . The central tensile region is surrounded by a ring of higher tensile stress at  $-3.7 \text{ GPa}$  at  $0.13 \mu\text{m}$  before reducing to zero at  $0.37 \mu\text{m}$ . Outside of this region the oxide is under high compression ( $5 \text{ GPa}$ ) before finally achieving parity with "normal" oxide stress ( $-3 \text{ GPa}$ ) at  $1.2 \mu\text{m}$ .

In comparing how the oxide is influenced by these precipitates it is apparent that the stress levels directly above the hydride become more intense and localised the closer the precipitate is to the surface. Where the pre-

cipitate is 0 or  $0.25 \mu\text{m}$  from the surface, the oxide compressive stress is reduced and becomes tensile to the extent that it will probably fail. In addition when the precipitate is closer than  $1 \mu\text{m}$  to the surface this inner stress region (which is reduced in compression or tensile) is itself surrounded by a region of increased compressive stress. That is to say that this region of increased compressive stress is greater than that experienced in the normal oxide situation reaching a peak of 4.8 GPa for the  $\text{UH}_3$  precipitate at  $0 \mu\text{m}$  depth.

The argument made in Section 3.1.2 was that failure of the oxide was only likely when it is in tension, and, depending on how close the  $\text{UH}_3$  precipitate is to the surface, the peak tensile stress can be found closer to the centre or further away from the precipitate central point. This could indicate that the oxide-layer would fracture closer to the centre of the surface protrusion if the precipitate was closer to the surface. Of interest to this discussion are images of surface protrusions exhibiting cracking in Figures 11 and 12. Although Figure 11 is complicated by the presence of an inclusion, both figures show crack paths that appear to converge (either as a start or end point) at the highest/central point of the protrusion rather than at the side only. This would suggest that the hydride particle itself is very close to the oxide in these cases.

At the same time that these stress patterns are developing the surface of the model is deforming allowing the surface protrusion to develop. The extent of deformation over the same x scale is shown in Figure 51 and the positions of peak tensile stress are indicated.

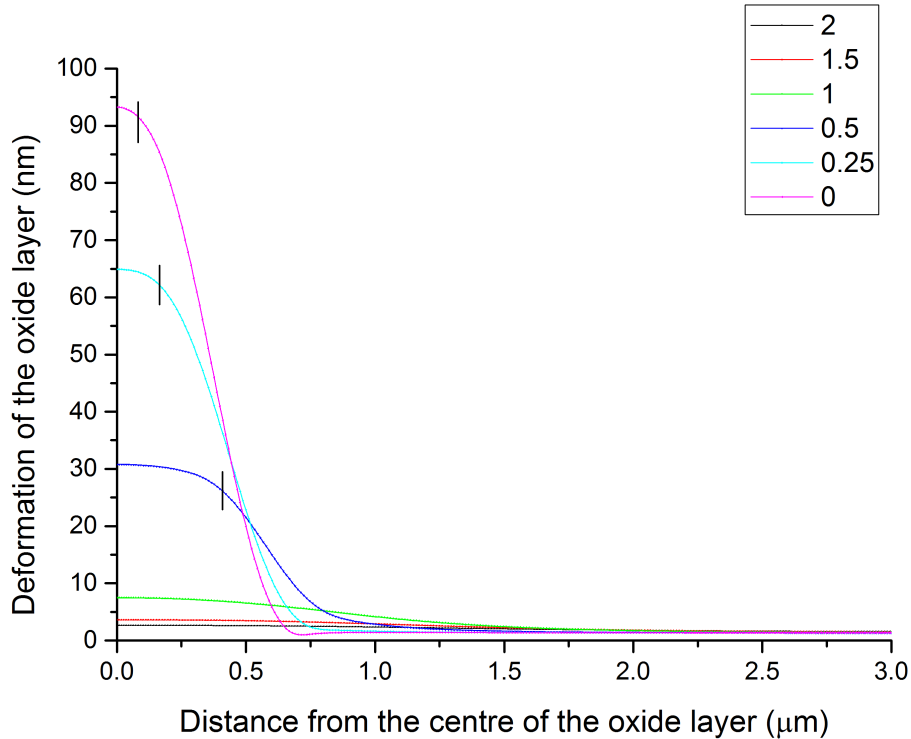


Figure 55: The deformation of the oxide-layer taken from the centre of the hydride to a distance of  $3 \mu\text{m}$  in the  $x$  direction for various depths in  $\mu\text{m}$ . Positions of peak oxide tensile stress are indicated.

At a depth of  $1 \mu\text{m}$  and greater the deformation of the surface is minimal. Above this depth at  $0.5 \mu\text{m}$ , a total deformation in the  $z$  direction of 32 nm occurs, which stays relatively constant until a distance of  $0.3 \mu\text{m}$  from the centre and then reduces to no deformation by  $1 \mu\text{m}$ ; i.e. the diameter of the protrusion is less than  $2 \mu\text{m}$  for a  $0.5 \mu\text{m}$  precipitate. The deformation seen when the  $\text{UH}_3$  is at a depth of  $0.25 \mu\text{m}$  is some 65 nm. This protrusion is more rounded and also of a smaller overall diameter at  $\sim 1.5 \mu\text{m}$ . At the extreme

case of the  $\text{UH}_3$  having a distance of  $0 \mu\text{m}$  to the oxide-metal interface, the protrusion is more protruding in the centre and is smaller diameter still at  $\sim 1.4 \mu\text{m}$ . In summary, as the hydride is placed at a greater depth, the effect on the oxide surface is to make the surface protrusion lower in height and flatter.

Plotted in Figure 56 is the TESE and total energy (TESE + plastic dissipation) calculated for these simulations as a function of the depth of the hydride.

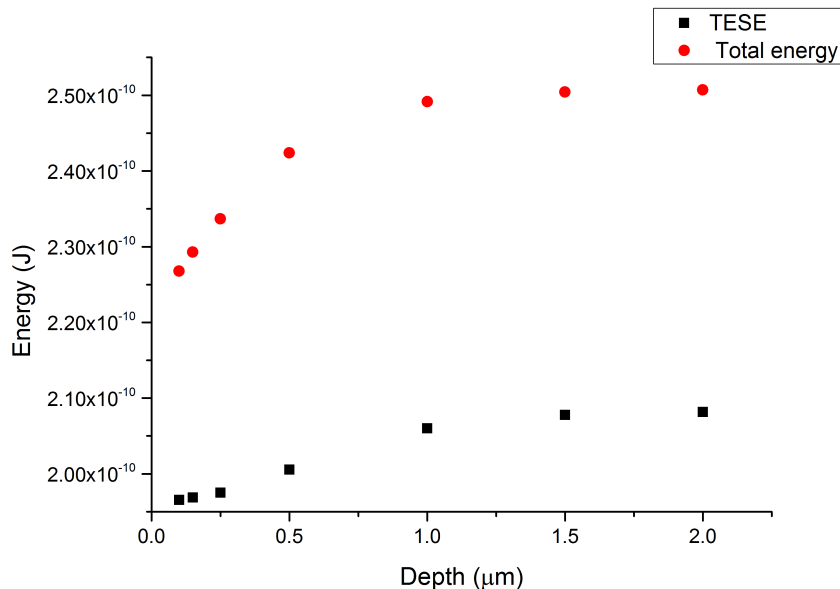


Figure 56: The total energy and the total elastic strain energy density plotted against the depth of the  $\text{UH}_3$  precipitate.

Below  $1 \mu\text{m}$  depth the TESE in these cases is approximately equivalent. Bringing the  $\text{UH}_3$  precipitate closer to the surface results in a reduction of TESE of around 4.5%. This suggests that on TESE grounds that precipitation closer to the surface is favoured over precipitation at depth. When

plasticity dissipation is included (total energy) a similar trend is found for preferential nucleation nearer the surface. This agrees with the experimental work which has observed  $\text{UH}_3$  at or close to the oxide surface (Section 1.6).

The deformation of the bulk metal gives an indication to the hydride development at different depths. In Figure 56 is the displacement of the uranium bulk is shown for the depths of  $2 \mu\text{m}$   $1 \mu\text{m}$  and  $0.5 \mu\text{m}$ . The colours indicate the displacement of the material occurring with red indicating the largest amount of displacement.

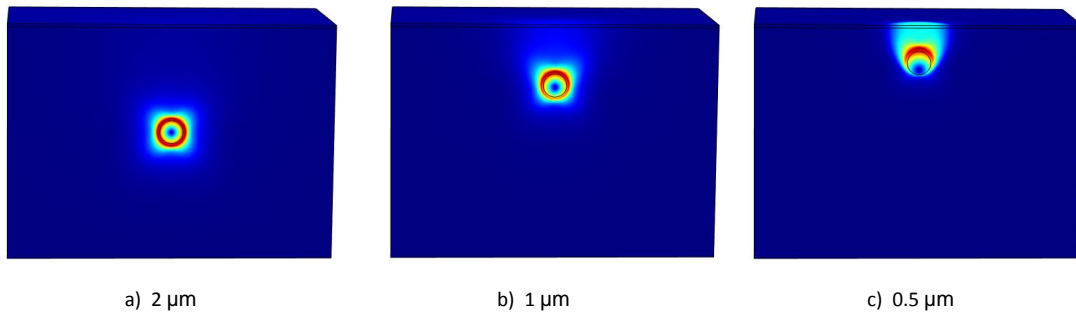


Figure 57: The displacement of the uranium bulk for depths of a)  $2 \mu\text{m}$  b)  $1 \mu\text{m}$  and c)  $0.5 \mu\text{m}$ . The colours indicate the displacement of the material occurring with red indicating the largest amount of displacement

When the hydride is at a  $2 \mu\text{m}$  depth the deformation is uniform in all

directions, which could mean that the  $\text{UH}_3$  precipitate would develop in all directions. When this depth is decreased to  $1 \mu\text{m}$  the displacement increases slightly above the precipitate. Finally, at a depth of  $0.5 \mu\text{m}$  the uranium displacement is greatest above the precipitate. This indicates that as the  $\text{UH}_3$  precipitate is brought closer to the surface, uranium is increasingly displaced towards the model surface.

## 4.4 Discussion

The presence and intensity of compressive and tensile regions close to the surface and/or close to the sub-surface precipitate might reasonably be expected to influence the development of these precipitates. This influence may occur through these mechanisms.

### 4.4.1 Diffusion argument

Firstly, those areas of tension will have uranium atoms fractionally further apart as compares to the compressive regions. Since diffusion of hydrogen through this structure is dominated by interstitial to interstitial jumps [26] the U-U distance is an important factor and a larger U-U distance will probably bring about faster diffusion. Takakuwa et al. [103] have shown such an influence of stress on diffusion in steels and welds.

### 4.4.2 Solubility argument

Secondly, hydrogen has been found to accumulate preferentially at high tensile regions in the uranium system [46]. Similarly, Wriedt and Orani [104]

have observed a solubility effect of hydrogen in steel with a variation in tensile and compressive stress. This mechanism may again be related to the size of the U-U distances with tensile regions having larger U-U distances, larger interstitial distances and more energetically favourable sites for hydrogen to locate in.

#### **4.4.3 Phase change argument**

Lastly, the amount of stress could affect the ability of uranium to transition to  $\text{UH}_3$ . Since the phase transformation from metal to hydride incurs a volume expansion, work is invested on the surrounding metal matrix. It seems reasonable to think that in regions where the uranium atoms are further apart, less energy will be required to transform to hydride. On the basis of this one could predict that the phase transformation might be more likely to occur in regions of tensile stress as compared to compressive stress.

#### **4.4.4 Hydride development**

So, turning to the understanding of the stress profiles developed in  $\text{UH}_3$  precipitates close to the surface: tensile regions are prominent to the side and above the precipitate. In these regions the idea is that hydrogen can be delivered faster (diffusion argument) and in more quantity (solubility argument) to these regions. Since these regions have hydrogen in potentially higher concentrations (solubility argument) and they are also in regions where phase change might be more energetically favourable (phase change argument), these are the regions that would be expected to develop into  $\text{UH}_3$  at a faster rate. These considerations lead to a hypothetical mechanism of the develop-

ment of sub-surface precipitates as shown in Figure 58.

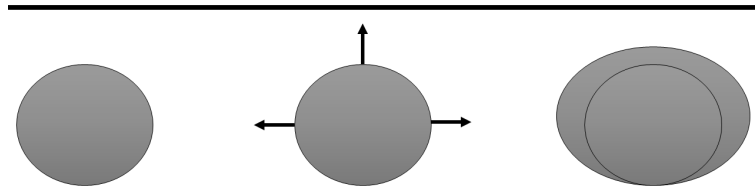


Figure 58: The possible growth mechanism for an initial hydride nucleation site. The hydride grows upwards and to the sides with the possibility of forming streamers below.

This process would appear to be valid for spherical precipitates nucleated close to the surface. Critically the tensile regions to the side are only observed in the case of anisotropy in the metal. Once initiated the precipitate grows upwards and outwards at a faster rate enhanced by the tensile regions. Metal above the precipitate is limited and once consumed further faster growth can only occur over the x-direction.

A further feature of great interest is that of streamers that have been observed in  $\text{UH}_3$  cross-sections (see Figure 11 and section 1.6). One explanation based on their location in Figure 11 is that they might be related to the focused tensile region found below the precipitate. Brierley [105] has recently shown similar streamers around cerium hydride precipitates. Since Brierley's material was isotropic (FCC) this suggests that the tensile region argument might not be valid (since the isotropic model did not show tensile regions).

A final point of note is to consider the metal region outside of the tensile region very close to the surface. Given that this is compressive it could be that further nucleation is retarded in this region (for the arguments of reduced

H flow, solubility and increased penalty in transforming uranium to UH<sub>3</sub> in a compressed region). If this relationship were true, there may be a reduced probability of UH<sub>3</sub> precipitating close to one another. This simulation would suggest that they should have reduced chances of nucleating within 2 μm of each other.

## 4.5 Summary

A UH<sub>3</sub> precipitate has been modelled at six different depths from 0 μm to 2 μm and the stress and deformation were calculated on the oxide surface and around the precipitate. On the oxide surface there is a central region surrounded by a ring of high compressive stress. This central region is either under less compressive or increased tensile stress with the stress tending to tensile stress when the precipitate is closer to the surface. Outside of the ring of increased compressive stress, the stress reduces when moving away from the UH<sub>3</sub> precipitate and approaches the normal compressive stress in the oxide. This could have the effect on the precipitate:

- The diffusion of hydrogen, solubility of hydrogen and the ability of the uranium to transform into UH<sub>3</sub> could be important factors in the UH<sub>3</sub> precipitate development. With evidence found from the stress models that the precipitate may preferentially develop into an ellipsoidal shape.
- In anisotropic matrices streamers could form due to the tensile region found beneath the precipitate.
- To the side of the precipitate but close to the oxide surface there are

rings of compression. These could limit the  $\text{UH}_3$  precipitate close to one another.

- This work assumes a grain size of the  $\text{UO}_2$  in the region of 10 nm which is to be expected from the work carried out at AWE, however, in a more general industrial context the grain size will be around 10  $\mu\text{m}$ . This increased grain size could have an influence on the failure point of the oxide over layer and also the amount of pre-stress within the oxide layer.

## 5 Stress induced by different shaped hydrides and multiple hydride precipitates

It has been considered that a change in shape of a hydride precipitate containing the same amount of  $\text{UH}_3$  may have an impact on the stress generated both in the hydride and the bulk metal. Experimentally, hydride precipitates have typically been observed as horizontal ellipsoidal in shape and nucleated within  $1 \mu\text{m}$  of the surface (Section 1.6). Which suggests either that (i) the horizontal ellipsoidal shape generate the least amount of energy and would therefore be preferential on nucleation, or (ii) stress generated by a sub-surface precipitate is likely to change its growth behaviour so that as the hydride increases in size the shape becomes more horizontal ellipsoidal. The energy of nucleation was previously examined by Greenbaum with regards to hydride formation on the surface of palladium, as discussed in Section 1.8. In an elastic matrix he suggested that the shape with the lowest energy of formation was semi-spherical hydride at a free surface. Whilst in an elast-plastic matrix with an oxide Greenbaum found that a vertical ellipsoid was preferential.

The work described in this section will examine the effect shape has on (i) the stress profile surrounding the hydride with a pre-stressed oxide and (ii) total energy for a  $\text{UH}_3$  system. The deformation on the surface will be compared to experimental AFM data of uranium samples exposed to hydrogen, collected at AWE [15], to evaluate whether the model is reasonable. Then a simulation of a multiple precipitate system will examine the influence

two hydrides can have on each others stress profile and deformation of the surface.

### 5.1 Stress induced by different shaped hydride precipitates

Hydride precipitates were singly introduced into an anisotropic model at a depth of  $0.5 \mu\text{m}$  depth from the surface with a  $64 \text{ nm}$  oxide layer. The volume of the hydride was held constant at  $0.065 \mu\text{m}^3$ , which is equivalent to a spherical hydride with a  $0.5 \mu\text{m}$  diameter. The hydrides in this model are ellipsoidal and their shape determined by the ratio of the height to width (A:B). An image depicting the different axis of the hydride is shown in Figure 59 where dimension A is perpendicular to the surface (z) and dimension B is parallel to it (x,y). This height to width ratio of the initial hydride particle was set to 2:1 and 1:2 in each model to represent vertical and horizontal ellipsoidal hydrides respectively.

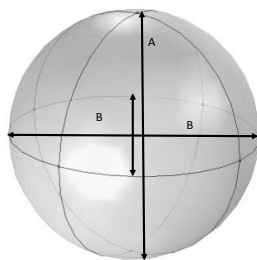


Figure 59: The different dimensions of an ellipsoidal hydride precipitate with (A) representing the height and (B) the width.

Figure 60 shows the pressure surrounding the precipitate for the two different ellipsoidal shapes, with the red indicating compressive stress and blue tensile stress. In a similar fashion to Section 4 the pressure scale shown was truncated from -0.1 GPa to 0.1 GPa for the cross section (a) and was not truncated for the bird's-eye view (b) of the oxide surface.

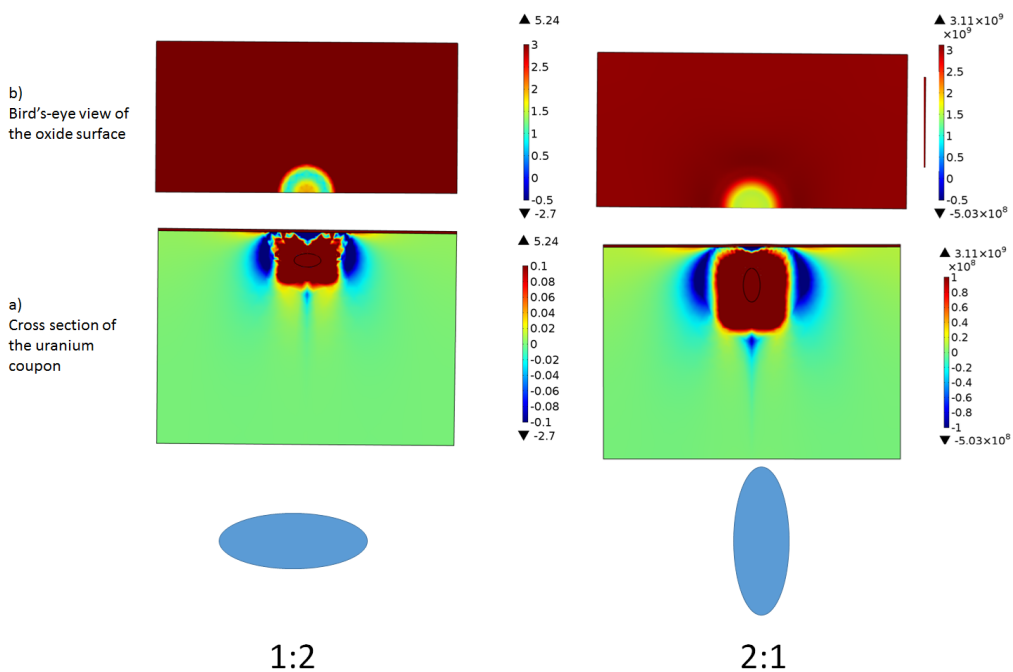


Figure 60: Images showing the pressure generated due to  $\text{UH}_3$  nucleated at a  $2 \mu\text{m}$  depth, assuming isotropic material properties:a) cross section of the whole model; b) bird's-eye view of the oxide surface.

For the vertical ellipsoid the compressive pressure at the  $\text{UH}_3/\text{U}$  interface is 0.8 GPa. Close to the  $\text{UH}_3/\text{U}$  interface the metal experiences a tensile

region of magnitude -0.12 GPa at  $0.58 \mu\text{m}$ . Whilst in the z direction in the bulk there is a smaller region of tensile stress of magnitude -0.05 GPa at a distance of  $0.85 \mu\text{m}$ . Directly above the  $\text{UH}_3$  precipitate but below the oxide the metal experiences a tensile stress of -1.5 GPa. Moving in the x direction this tensile region is surrounded by a ring of compressive stress of 0.25 GPa. This in turn is surrounded by metal under tensile stress as would normally be the case where  $\text{UH}_3$  is not present. This sub-surface metal stress profile then interacts with the oxide causing the inherent oxide compressive stress levels to range from 1.8 GPa directly above the hydride (above the uranium metal tensile region) to 1.7 GPa above the ring of compressive stress in sub-surface uranium to 3.1 GPa more distant from the  $\text{UH}_3$  precipitate

For the horizontal ellipsoid the compressive pressure at the  $\text{UH}_3/\text{U}$  interface is 0.85 GPa. This compressive region fully surrounds the precipitate. Further out from this compressive region is a tensile region that reaches a peak of -0.14 GPa at  $1 \mu\text{m}$ . In the z direction the compressive stress at the  $\text{UH}_3/\text{U}$  interface is 0.9 GPa and further out there is a tensile region that has a peak stress of -0.2 GPa at  $0.1 \mu\text{m}$ . The stress pattern above the  $\text{UH}_3$  precipitate is once again a tensile region of -2 GPa, surrounded by a ring of compressive stress of 0.35 GPa. This sub-surface metal stress profile then interacts with the oxide causing the inherent oxide compressive stress to range from 1.8 GPa directly above the uranium metal tensile region to 0.2 GPa above the ring of compressive stress in sub-surface uranium to 4.1 GPa more distant from the protrusion.

One interesting difference is the region of tensile stress in the uranium metal above the precipitate but below the oxide. In the case of the vertical

ellipsoid this region is smaller and reaches a stress of -1.5 GPa. The way this oxide layer interacts with the oxide layer means there is a large change on the stress on the surface. The vertical ellipsoid interacts with the surface to the same amount directly above the hydride but does not decrease further. Whilst the horizontal ellipsoid reaches that same level of stress above the hydride and then decreases in a ring of lower compression (towards tensile) followed by a region of higher compression. This means the horizontal ellipsoid influences the oxide-layer more substantially into the tensile region and could mean the horizontal ellipsoid is more likely to fracture the surface.

Another difference is that the vertical ellipsoid shape has a larger region of tension surrounding it in the metal. While both examples have tensile regions outside of compressed metal regions in the x direction, those for the vertical are larger and greater in intensity as compared to the other horizontal. This might indicate that growth of precipitates is more likely in the x direction and if this was the case that it be promoted in the case horizontal ellipsoids.

Figure 61 shows a comparison of the TESE for five A:B hydrides (2:1, 3:2, 1:1, 2:3, 1:2) in an elastic uranium matrix from this simulation and this was compared to Greenbaum's simulation on palladium [56]. The two data sets were normalised to the spherical (1:1) shaped hydride and plotted against the percentage difference from this value.

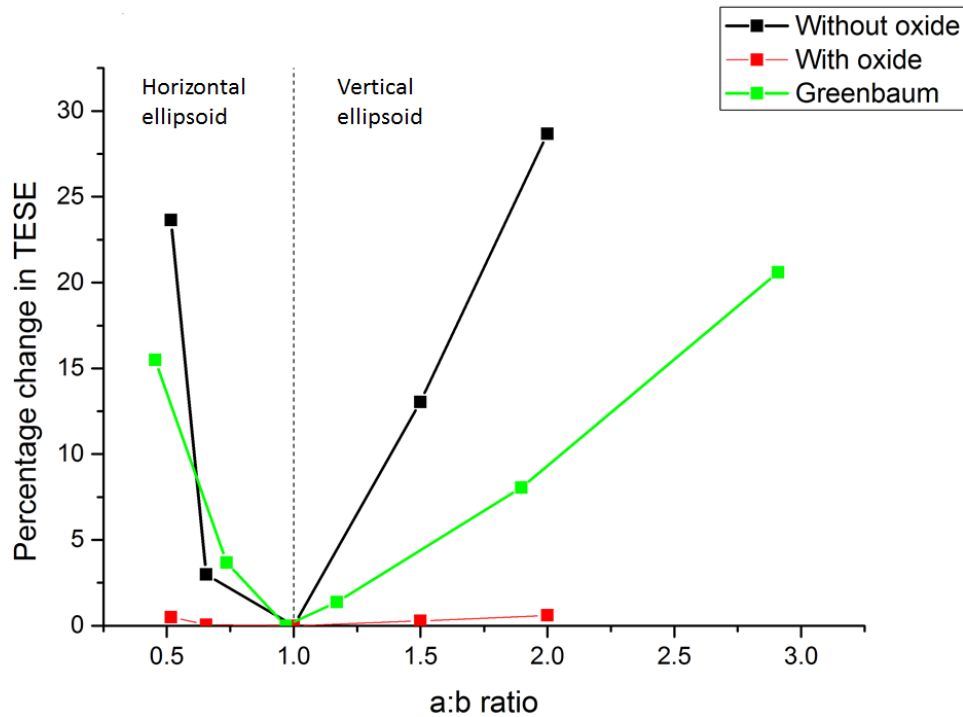


Figure 61: The percentage change in TESE from the normalised TESE value (when spherical) against the A:B ratio of the hydride. Greenbaums work [56] is compared to work for this thesis.

There are a number of points to make about Figure 61. Firstly for the uranium system without an oxide the TESE is at its lowest point for a spherical precipitate. As the precipitate becomes a horizontal ellipsoid the energy increases steadily at first, then more rapidly to over 20% for a 1:2 precipitate. A change from sphere to vertical ellipsoid causes the energy to increase at a more constant rate. This result is similar to Greenbaum, which is surprising as Greenbaum studied the precipitate at the free surface, compared to one

at 0.5  $\mu\text{m}$  depth in this study [56].

Secondly turning to the use of the same system with a pre-stressed oxide. Here the relative changes in TESE are much less, and changing the A:B ratio has less of an effect. According to this analysis the most likely shape should be spherical, followed by horizontal ellipsoid but the relative energy change is not large, reading highest for 2:1 of 1.1%.

Without the stress of the oxide included in the TESE calculations both this work and that carried out by Greenbaum suggests similar results that the spherical hydride is preferential and the TESE increases for both ratios steeply. With a high% change in the TESE immediately once the hydride shape is non-spherical. When the oxide-layer is included the results differ. The pre-stressed oxide-layer has a large total elastic stress (3 GPa) that the hydride expansion does not alter the total energy of the system as a percentage as much. With a total of only 1.1% change in TESE, however, a similar pattern for the spherical hydride being preferential is still seen. Although a change is noticed that the horizontal ellipsoidal shape becomes preferential over the vertical ellipsoidal this could be due to the horizontal ellipsoid interacting with the oxide more (as seen Section 4.1) and thus relaxing the oxide stress more.

The same simulation was run and the total energy (including plastic dissipation) was calculated and compared to results from Greenbaum and this is shown in Figure 62.

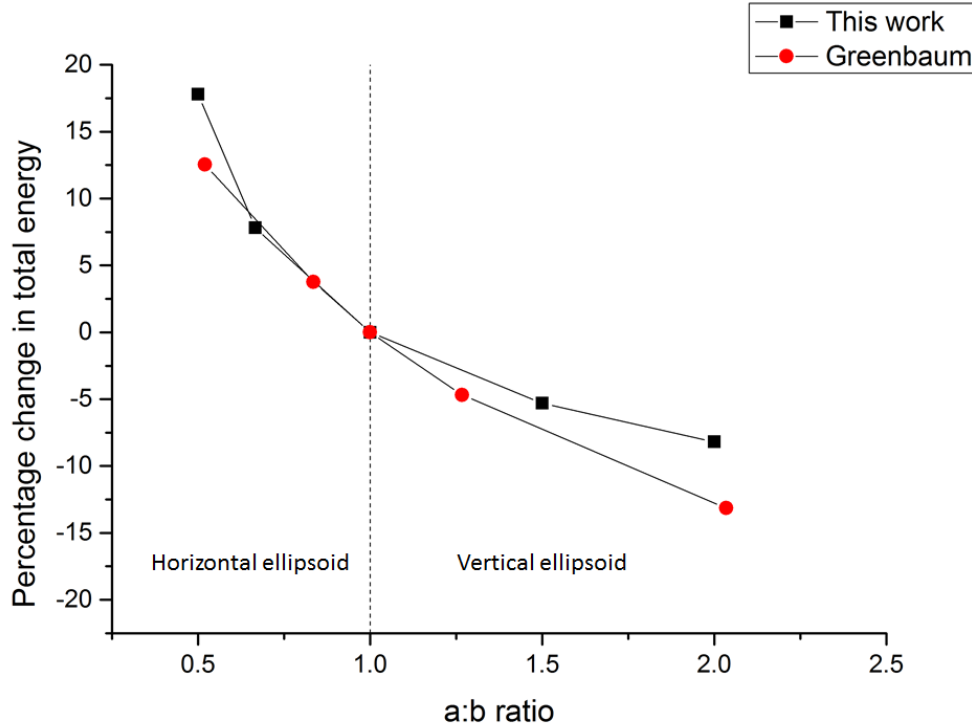


Figure 62: The percentage change in total energy from the normalised total energy value (when spherical) against the A:B ratio of the hydride. Greenbaums work [56] is compared to work for this thesis.

The trend is similar both for this work and Greenbaum for the elasto-plastic matrix. However within  $\text{UH}_3$  the energy trails off as the vertical ellipsoid increases in A:B ratio. The same conclusion is reached for both this work and Greenbaum that a vertical ellipsoid is preferential shape with the lowest energy of formation within an elasto-plastic simulation.

It is surprising that a vertical ellipsoid is preferential within the simulations found in both this work and in Greenbaums [57] on energetic grounds.

It has also shown the importance in including the plastic deformation within the model as there can be significant plastic deformation.

The fact that this result suggests that a spherical/vertical ellipsoid shape is preferential and the fact that this is not seen within the experimental results suggest that there are some other important on the  $\text{UH}_3$  shape i.e. that the energy of the shape in the system is not the only factor. These other factors could include the local availability of hydrogen close to the  $\text{UH}_3/\text{U}$  interface. Even though the vertical ellipsoid may be a more energetically favoured shape the tensile regions could encourage the hydride to grow faster horizontally due to the local availability of hydrogen and the possibly that these tensile regions require less energy to transform from  $\text{U-UH}_3$ .

## **5.2 Stress profiles of two $\text{UH}_3$ precipitates nucleated in close proximity**

An aspect that is of interest is the effect sub-surface  $\text{UH}_3$  precipitates have on each other's stress profile. Greenbaum briefly examined this possibility but only the effect of the maximum stress on the oxide surface for identical precipitates superimposed next to each other [57]. Greenbaum found that the maximum radial stress on the oxide would not increase beyond the pressure of one hydride growth even if the hydrides were growing next to each other. This study will consider the influence of these modified stress profiles on the way they develop and if two precipitates beneath the surface are distinguishable from one protrusion. Further work examining AFM data collected at AWE will allow this study to compare with realistic surface protrusions.

Simulations containing two sub-surface  $\text{UH}_3$  precipitates were not achievable to the desired accuracy in 3D. For this reason a 2D model was created for this part of the study. The total size of the 2D model was  $10 \mu\text{m}$  by  $10 \mu\text{m}$ , with a 64 nm oxide-layer thickness. The shape of the  $\text{UH}_3$  precipitates were taken to be circular (3D spherical) and to have a size of  $0.5 \mu\text{m}$  diameter. The hydrides were nucleated simultaneously and were at the same depth of  $0.5 \mu\text{m}$ . The same materials properties were used as in previous models. Simulations were created with distances of  $1.5 \mu\text{m}$ ,  $2.5 \mu\text{m}$  and  $3.5 \mu\text{m}$  between the precipitates. This distance was defined from the centre on one hydride to the centre of the other hydride. The distance range was chosen as it was similar to the data collected in AFM experiments at AWE.

Below in Figure 63 are three stress maps of two hydrides apart at distances of  $1.5 \mu\text{m}$ ,  $2.5 \mu\text{m}$  and  $3.5 \mu\text{m}$ , where negative stress is tensile and positive is compressive.

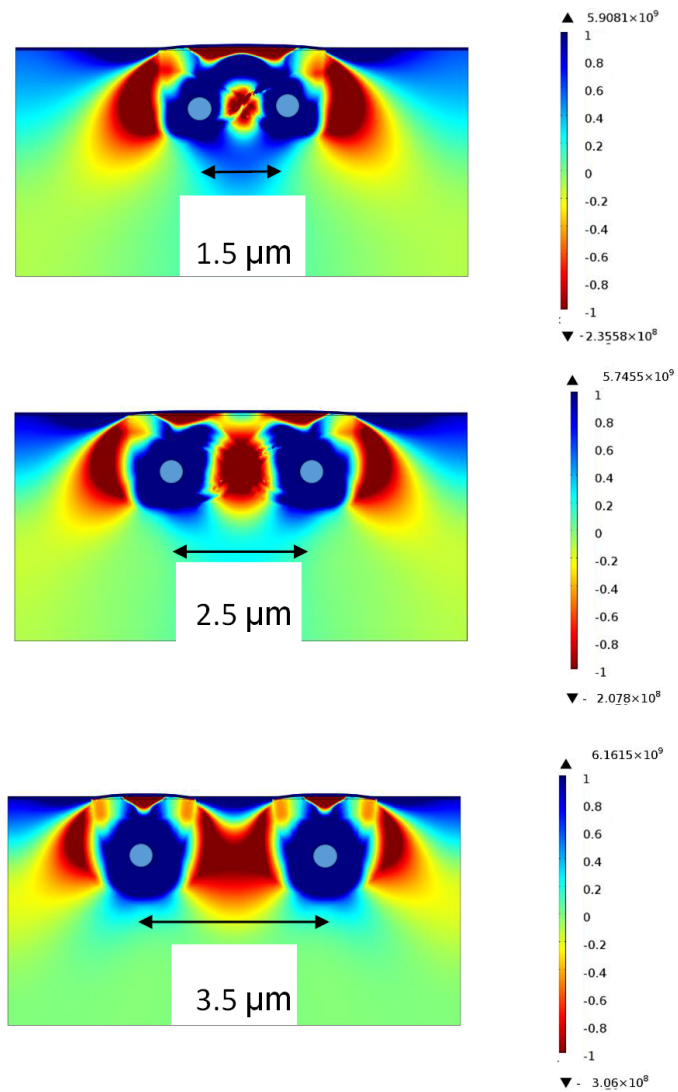


Figure 63: Three stress maps of two sub-surface precipitates at distances of a)  $1.5 \mu\text{m}$  b)  $2.5 \mu\text{m}$  and  $3.5 \mu\text{m}$ .

Precipitates at a distance of  $3.5 \mu\text{m}$  show a stress profile similar to that of two superimposed single precipitates (Section 4.2). For example in the near surface metal two tensile regions are surrounded by a compressive region. When the precipitates are placed closer at a distance of  $2.5 \mu\text{m}$  their

stress profiles begin to interact. In the sub-surface metal region the two tensile regions begin to coalesce and the previously seen compressive region is smaller. Finally, at a distance of  $1.5 \mu\text{m}$  apart, the sub-surface metal region in-between the two tensile regions has merged into one singular tensile region

The pressure on the oxide layer for those same three distances is shown in Figure 64.

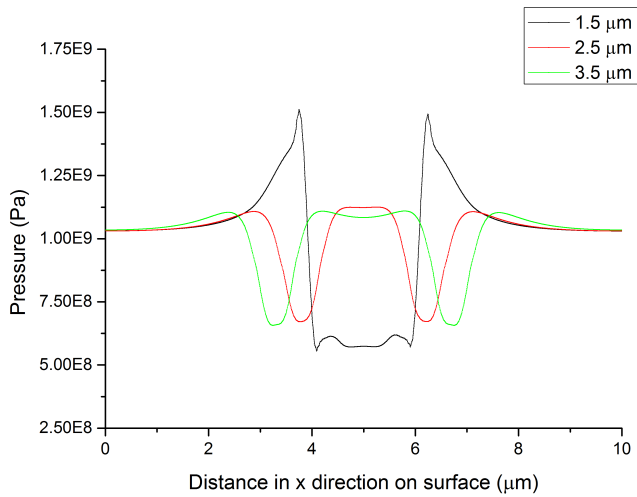


Figure 64: The pressure on the surface for different distances between two hydrides at a depth of  $0.5 \mu\text{m}$ .

When the precipitates are a distance of  $3.5 \mu\text{m}$  apart the same regions of lower compression (towards tensile) above the precipitate and increased compressive to either side of the precipitate as seen in the singular precipitate example. These same regions are found for the  $2.5 \mu\text{m}$  with a lower compressive region in-between the hydrides than the  $3.5 \mu\text{m}$  distance. When the precipitates are  $1.5 \mu\text{m}$  apart a significant change happens. Instead of compressive stress in-between the hydride that region becomes less compressive

(towards tensile), which would increase the chance of the oxide fracturing. Further to this the compressive regions on the other side are also higher than previously.

The total energy of the 2D model is shown for both circular and elliptical hydrides for distances of 0.5-3  $\mu\text{m}$  between Figure 65.

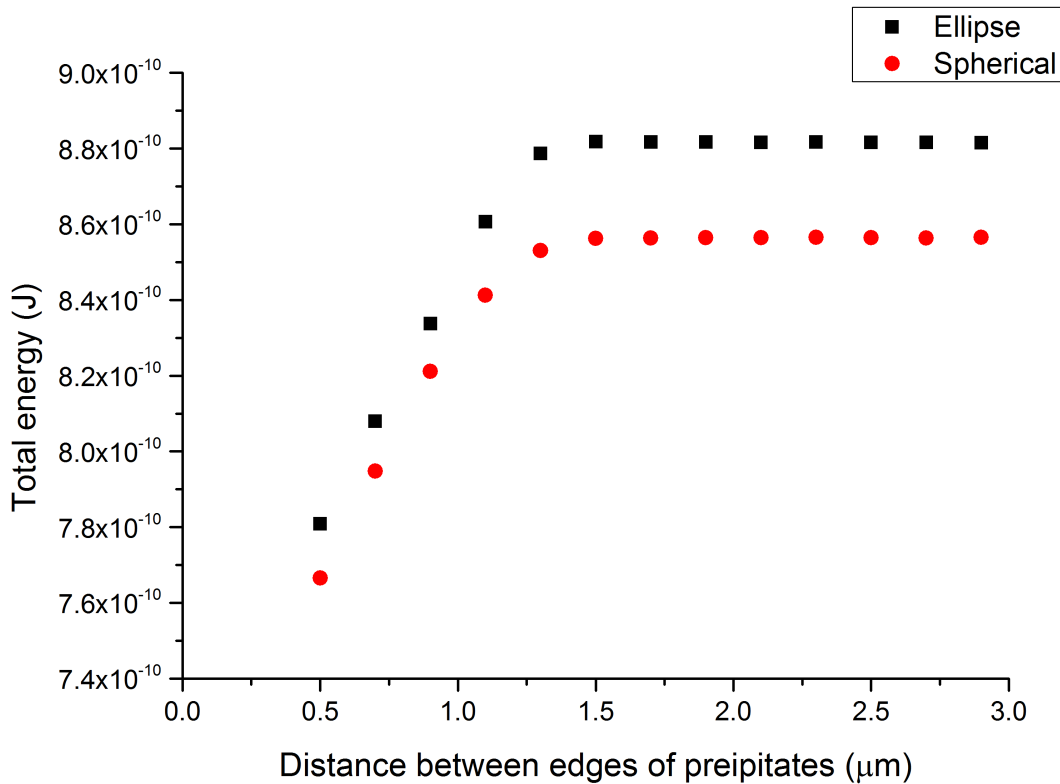


Figure 65: The total energy for different distances between two hydrides at a depth of 0.5  $\mu\text{m}$  for a) 0.5 diameter circular and b) 1:2 ellipse with the same area.

As the hydride distance decreases between the two hydride sites the total

energy for the system is constant until a point when the energy begins to fall. This occurs at  $1.5 \mu\text{m}$  for the circular and horizontal ellipse precipitates.

Firstly on energetic grounds the total energy of both the circular and ellipse shaped precipitates are constant until a distance of  $1.5 \mu\text{m}$ . This would mean that on energetic grounds there is a benefit to coalesce when the distance is less than  $1.5 \mu\text{m}$ .

When the stress profiles are further than  $1.5 \mu\text{m}$  apart there is a compressive region near the metal/oxide surface and in a similar way to Section 4 this could retard their coalescence due to the diffusion of hydrogen being limited. However when the hydrides are closer than  $1.5 \mu\text{m}$  this compressive region becomes tensile, and this same region could then encourage diffusion and therefore coalescence.

Finally the effect of the two precipitates on the oxide is similar to two superimposed precipitates at distances greater than  $1.5 \mu\text{m}$ . Once closer than that point the region in-between the precipitates becomes tensile instead of compressive. This would mean that the surface is more likely to fracture if two precipitates are closer than  $1.5 \mu\text{m}$ .

This would imply that when the hydrides are at a distance of greater than  $1.5 \mu\text{m}$  apart there is a compressive region near the surface between the hydrides which could slow down the diffusion of hydrogen into the bulk. This slowdown of hydrogen could then limit the hydrides development closer to each other. However once that initial barrier has been breached (less than  $1.5 \mu\text{m}$ ) the further growth and amalgamation of the hydrides is encouraged due to a tensile region (instead of compressive) and the energy benefit which could encourage their coalescence. This then would increase the likelihood of

oxide fracture due to the lower compressive (towards tensile) stress. Experimentally (Section 1.4) surface protrusions are typically found at distances greater than  $2 \mu\text{m}$  apart, so it could mean that these sites are further apart than when the coalescence effect occurs.

### **5.3 Comparison of the deformation of the oxide to AFM surface protrusion data**

There are limited opportunities for comparing the model developed against experimental data. One method was to compare surface deformation results from the model against collected AFM data measuring the surface protrusions. Similar AFM data has previously been collected on Gd+H<sub>2</sub> samples [54].

Two sets of AFM data (collected at AWE [15] were extracted using MATLAB(version:R2012A) and a number of areas were isolated as useful for this comparison. These areas were chosen as the sites had no observable other nearby protrusions within  $4 \mu\text{m}$  making these a good test case to think about surface protrusions in proximity to one another. Referring to Figure 66 both images are of a similar scale, red indicates a high deformation ( $\sim 200 \text{ nm}$ ) and blue indicates no deformation.

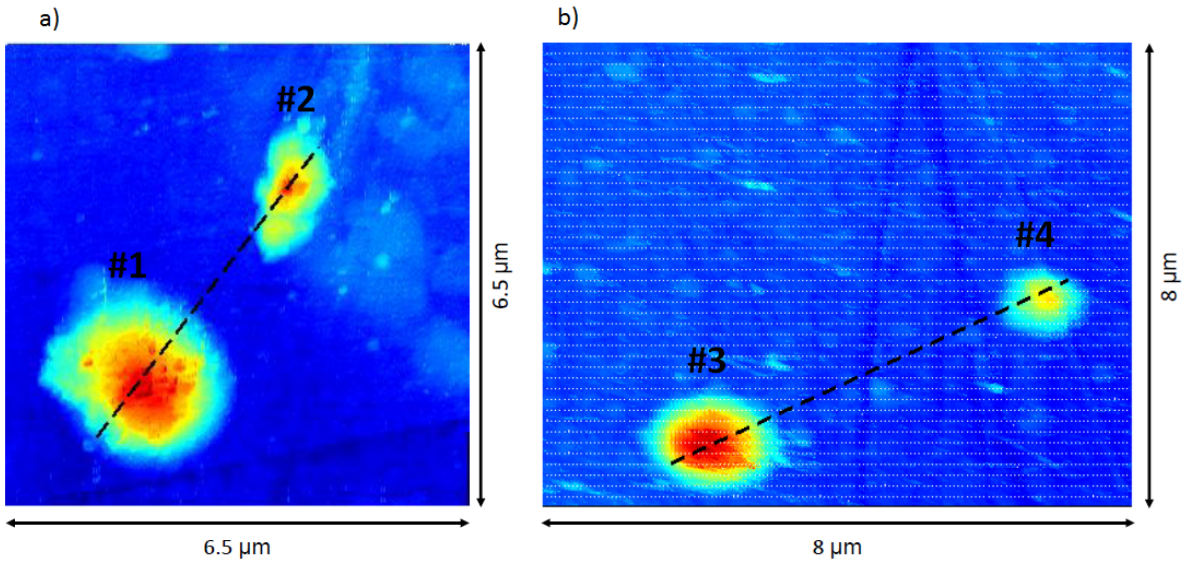


Figure 66: Two AFM images, the dotted lines indicate the line the AFM data was taken from. On the left are surface protrusions #1 and #2 which are  $3.5 \mu\text{m}$  apart and on the right are surface protrusions #3 and #4 which are  $5.1 \mu\text{m}$  apart [15].

Referring to Figure 66a, two surface protrusions are apparent. The larger #1 is circular with a diameter of  $\sim 2 \mu\text{m}$ . Site #2 is smaller and somewhat ellipsoid in plan view ( $0.85 \mu\text{m}$ ,  $1.5 \mu\text{m}$ ) with the long axis somewhat orientated to its neighbour. The distance between the central points of #1 and #2 (from previous work presented in Section 4 is likely to be the position of the  $\text{UH}_3$  precipitate in the x-y plane) is  $3.5 \mu\text{m}$ . Because site # 2 is smaller, it might be assumed that it represents a later precipitation and therefore that its growth might be modified by the larger site. This however cannot be known with confidence.

Referring to Figure 66b, two surface protrusions are again apparent but this time they are some  $5 \mu\text{m}$  apart. Both sites are broadly circular with site #3 having a diameter of  $1.5 \mu\text{m}$  and the remaining site #4 having a diameter of  $1 \mu\text{m}$ . In this case the fact that the sites are generally circular it can be suggested that they have no significant effect on each other.

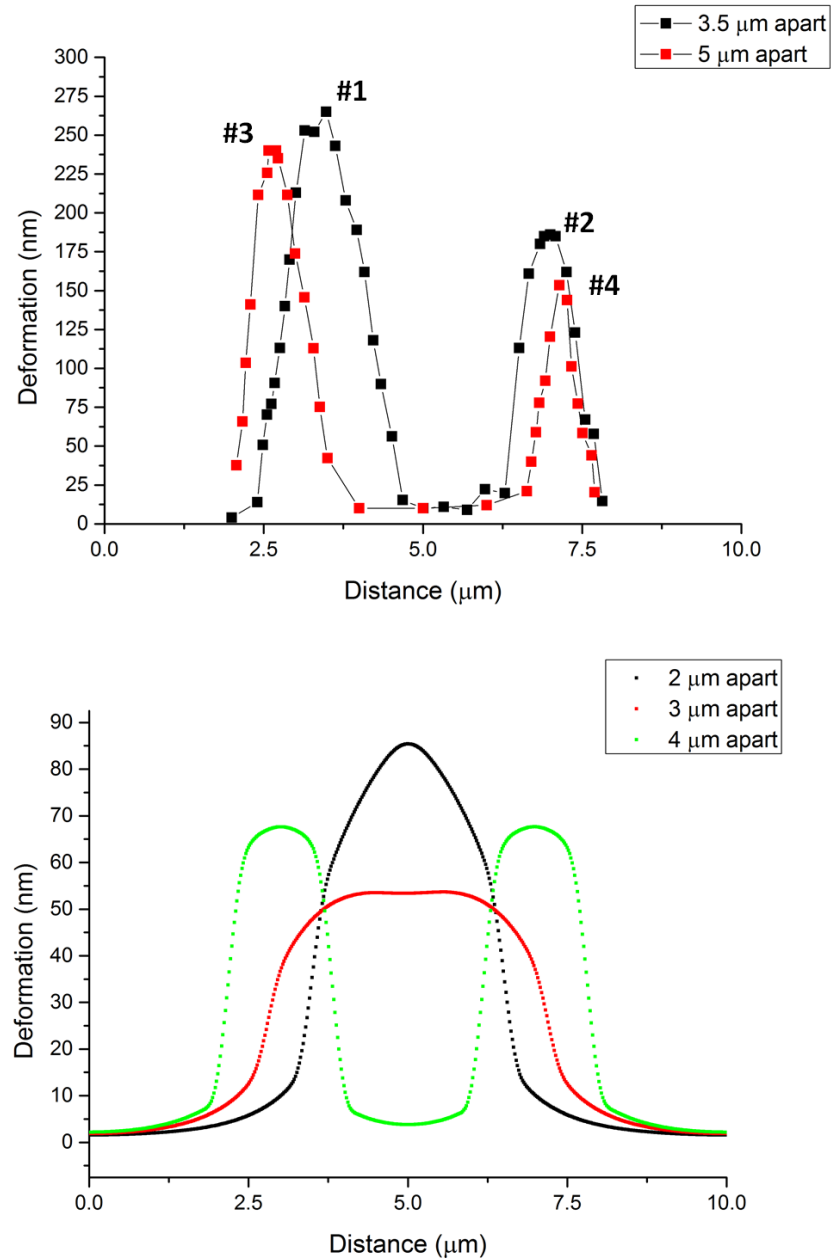


Figure 67: A two dimensional profile of two hydride sites from a) AFM sites and b) simulated results of two spherical hydrides at a depth of 0.5  $\mu\text{m}$ .

The simulated work indicates that at a distance of  $4 \mu\text{m}$  apart the hydride sites produce two distinct surface protrusions of a height of 65 nm. When the hydrides are closer at  $3 \mu\text{m}$  the surface protrusion is one undistinguishable surface protrusion, which has a lower deformation of 50 nm. When the hydrides are  $2 \mu\text{m}$  apart the deformation peaks high at 85 nm and decays to zero much faster. For the AFM data the surface protrusions are both two distinguishable  $5 \mu\text{m}$  and  $3.5 \mu\text{m}$  distance apart, so the model is in agreement that at these distances the surface protrusions should be indistinguishable. Of note is the fact in the simulation the precipitates are at a depth of  $0.5 \mu\text{m}$  and are the same size, which could influence the development of the hydrides.

From the simulations it is possible for hydrides at a depth of  $0.5 \mu\text{m}$  to form a singular long flat surface protrusion. Further to this when the hydrides are sufficiently close two hydrides at depth of  $0.5 \mu\text{m}$  will cause the oxide-layer to deform more.

## 5.4 Summary

In this section the stress profiles, total energy and deformation of the surface were investigated for different sized precipitates and for a multiple precipitate system.

- The shape of the vertical ellipsoidal and the horizontal ellipsoidal had similarities, however, the influence of the shape on the metal just beneath the surface and oxide layer were different. The total energy of the system suggested that the vertical ellipsoidal shapes were preferential nucleation shapes for the precipitates in an elasto-plastic system.

Since these shapes aren't seen experimentally [44] it could suggest that the growth of the hydride is a contributing factor for their horizontal ellipsoidal shape.

- When the two precipitates are at a distance of greater than  $1.5 \mu\text{m}$  apart there is a compressive region near the surface between the hydrides which could slow down the diffusion of hydrogen into the bulk and limit their coalescence. However once that initial barrier has been breached (less than  $1.5 \mu\text{m}$ ) the further growth and amalgamation of the hydrides is encouraged due to a tensile region (instead of compressive) and the energy benefit.
- For two precipitates at a depth of  $0.5 \mu\text{m}$  and a distance greater than  $\sim 3 \mu\text{m}$  it is possible to form a singular long flat surface protrusion. When these precipitates are nucleated even closer together the tensile stress on the surface increases even more meaning that the oxide surface is more likely to fracture.
- An aspect this model hasn't taken into account of, but is important, is the residual stresses in the uranium metal due to fabrication and forming of the metal. In the case of uranium fuel rod the metal could be quenched and these thermal gradients induce residual stresses, furthermore they could be machined and this again induces residual stresses into the metal surface[7]. These effects could have significant effects both on the initial formation of the hydride but also it's subsequent transformation into a growth centre.

## 6 Factors that could influence the hydride stress profile and the transformation into growth centres

As discussed in Section 1 once the hydride precipitate reaches a certain size it can deform and stress the surface oxide causing it to fracture. Experimental data [9] [53] indicated that fracture has occurred on samples before the surface protrusion is  $\sim 4 \mu\text{m}$  in diameter. Once fractured, the local consumption of hydrogen will significantly increase (since the oxide is no longer an effective barrier). At a macroscopic level this increase in  $\text{H}_2$  consumption is observed as an increase in the reaction rate.

There are many factors that could influence the system stress profiles and transformations into growth centres: plastic deformation, oxide-layer thickness, grain orientation and work hardened layer. In this chapter these factors will be examined to determine their importance in this process.

### 6.1 The size of the precipitate beneath the oxide surface

A simulation was created that varied the size of the hydride beneath the surface to emulate a surface protrusion of  $2 \mu\text{m}$  diameter. The model from Section 3 was adapted so that the diameter was varied from  $0.08 \mu\text{m}$  to  $0.8 \mu\text{m}$  and the deformation on the surface was measured. Model surface deformations from these simulations are reproduced in Figure 69.

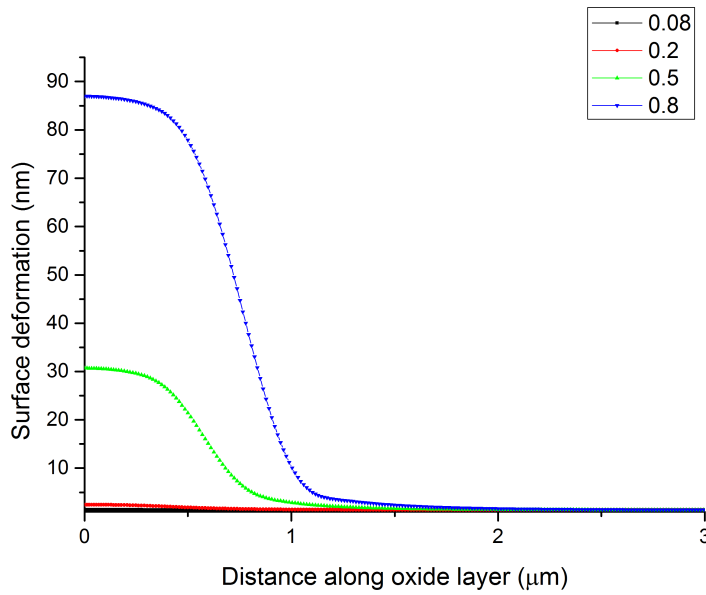


Figure 68: The deformation of the oxide surface for  $\text{UH}_3$  precipitates of diameter 0.08, 0.2, 0.5 and 0.8  $\mu\text{m}$ , the depth of the hydride is kept constant at 0.5  $\mu\text{m}$ .

As the hydride diameter increases the surface protrusion deformation increases in height significantly but the diameter of the protrusion does not increase appreciably. For a 60% increase in the precipitate diameter the protrusion height increases by  $\sim 180\%$  whereas the protrusion diameter increases by  $\sim 35\%$  (for a change in diameter from 0.5 to 0.8  $\mu\text{m}$ ). The largest protrusion modelled here was of diameter  $\sim 2.2 \mu\text{m}$  which is of a smaller size to those discussed in Section 1.6. This size of precipitate is chosen as a test case for subsequent investigations detailed in this section.

## 6.2 Influence of plasticity on hydride development for different sized hydrides

Previous work has suggested that precipitates below the size of  $1 \mu\text{m}$  only deform the surrounding metal elastically [106]. However, this was for a system where the precipitate-matrix experienced a strain misfit of 1-3% as opposed to the U-UH<sub>3</sub> case where the misfit strain is 20%.

If the U-UH<sub>3</sub> system remains in an elastic regime then there is the potential for the precipitate to dissolve (if hydrogen is removed from the local system). In this regime the total elastic strain energy (TESE) is an effective measure of the energy of the system.

The introduction of plastic deformation as the hydride grows (plastic deformation was observed for precipitates as small as  $0.08 \mu\text{m}$  diameter) means that this will not take place and that the TESE is no longer an effective measure of the energy of the system.

In Figure 69 plastically deformed regions surrounding three different sized precipitates of  $0.08 \mu\text{m}$ ,  $0.2 \mu\text{m}$  and  $0.5 \mu\text{m}$  are shown. The scale shown is that of the total effective plastic strain (amount of strain past the yield point of the uranium) with the red colour indicating a higher effective plastic strain.

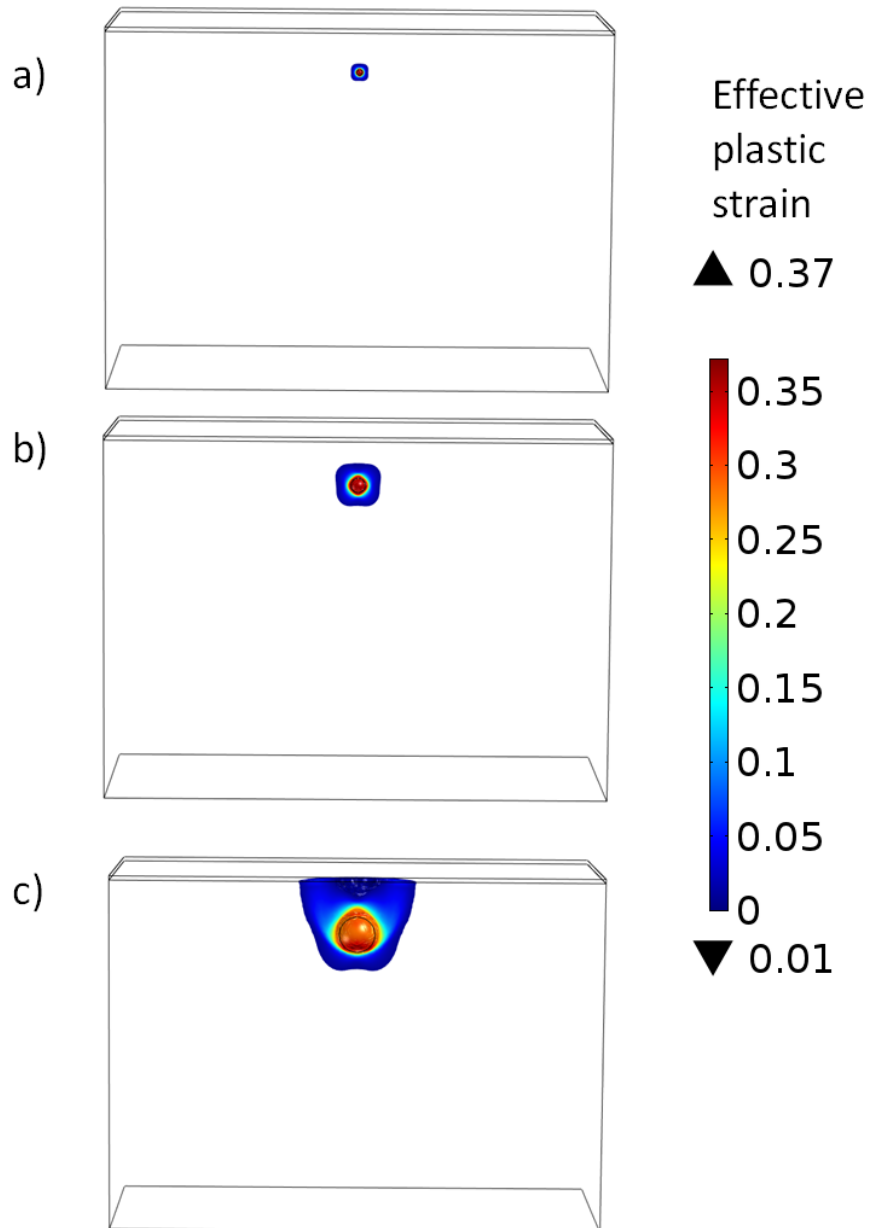


Figure 69: Plastically deformed regions surrounding the UH<sub>3</sub> precipitate are shown with the colours representing the amount of effective plastic strain. Precipitate diameter a) 0.08  $\mu\text{m}$  b) 0.2  $\mu\text{m}$  c) 0.5  $\mu\text{m}$  at a depth of 0.5  $\mu\text{m}$

As can be seen in Figure 69, the rectangular features of the plastic region

surrounding the hydride is common throughout the three different simulations. The rectangular features develop as a result of the orthogonal material properties of uranium; in each direction there is a significantly different plasticity effect depending how the grain is orientated. Further to this the maximum plasticity always observed at the bottom of the hydride has an effective plastic strain of 0.35 for the  $0.08\ \mu\text{m}$  and  $0.2\ \mu\text{m}$  hydrides and 0.37 for the  $0.5\mu\text{m}$  hydride. This implies that the region directly surrounding the hydride undergoes a high level of plastic deformation even at 40 nm diameter ( $\sim 120$  unit cells). This result confirms that precipitates formed as  $\text{UH}_3$  cannot be accommodated by elastic strain only in the metal and as such will plastically deform the surrounding metal. While it is possible that under the right conditions the  $\text{UH}_3$  precipitates could reduce in size under the influence of elastic stress (assuming removal of hydrogen from the system causes decomposition of the  $\text{UH}_3$ ), these simulations suggest that they will not completely disappear.

The surrounding plastic regions have important implications for the hydrides development. Willetts [107] has postulated that the plastic deformation of the metal can have important influences on the way hydrogen interacts within the material. He suggests that the hydrogen is more susceptible to trapping in plastically deformed metal. The presence of plastically deformed metal may also change the hydrogen diffusion and terminal solubility properties of the uranium. Such property changes are likely to effect the direction and rate of growth of sub-surface precipitates.

Plastic dissipation is the amount of energy spent in the simulation due to the formation of plastic regions. This changes for different sized precipitates,

however to understand the overall influence the value was normalised to the amount of plastic dissipation per unit volume ( $\mu\text{m}^3$ ) and this is shown in Figure 70.

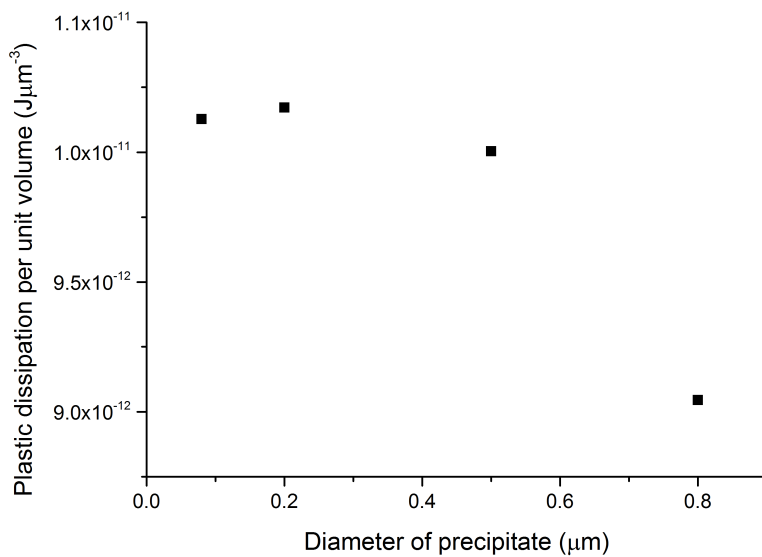


Figure 70: Plastic dissipation per unit volume for the different diameter precipitates.

When the diameter is small the plastic dissipation per unit volume is largest at  $1 \times 10^{-11} \text{ J}$  and after 0.2 diameter precipitate this energy decreases to  $0.9 \times 10^{-11} \text{ J}$ . This means that the work required to deform the matrix for every  $\mu\text{m}^3$  added reduces as the precipitate grows.

The plastic dissipation is primarily lost as heat. Previous work (see Appendix C) examined the possibility that the heat could have an impact on material properties and discounted it.

### **6.3 Influence of oxide thickness and stress on hydride transformation into growth centres**

The previous work in this section has assumed the oxide had a thickness of 64 nm, however, oxide over-layers in nuclear applications may have a range of thicknesses either side of this figure. This variation could have a significant impact on the size sub-surface precipitates can develop before oxide failure occurs. For this reason a model was created that varied the oxide-layer thickness from 20 nm to 500 nm. For these oxide thicknesses the compressive stress was fixed at 3 GPa prior to the introduction of the  $\text{UH}_3$

Figure 71 plots the least compressive or most tensile stress within the oxide for a given oxide thickness and sub-surface hydride site (depth 0.5  $\mu\text{m}$ , spherical precipitate diameters of 0.5 and 0.8  $\mu\text{m}$ ). This region is the ring observed on the oxide which is either low compressive or tensile stress. Also plotted is the assumed breaking point of the oxide-layer at -105 MPa (no grain size effect) and -1.1 GPa (grain size effect).

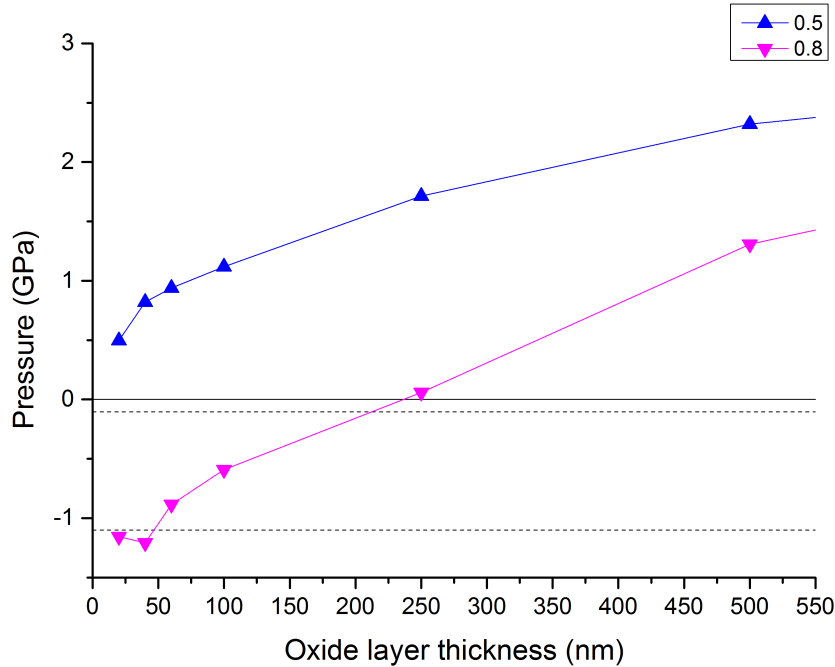


Figure 71: The minimum stress within the oxide-layer for a sub-surface hydride diameter  $0.5\ \mu\text{m}$  and  $0.8\ \mu\text{m}$  at a depth of  $0.5\ \mu\text{m}$  as a function of the oxide layer thickness.

Firstly considering the smaller sub-surface ( $0.5\ \mu\text{m}$  diameter) with the thickest oxide the oxide remains under considerable compression and is expected to remain intact. If the same system is considered with a thinner oxide the lowest compressive stress within the oxide remains considerable in the presence of the sub-surface precipitate:  $0.5\ \text{GPa}$  at  $25\ \text{nm}$ . This would suggest that oxide tensile failure will not occur for this size precipitate at this depth.

Turning to the larger of the two sub-surface precipitates ( $0.8\ \mu\text{m}$  diam-

eter). Again at the thickest oxide the least compressive pressure observed remains considerable at  $\sim 1.5$  GPa, and again this minimum compressive force is reduced for thinner oxides. For this sized sub-surface precipitates at this depth the least compressive force reduces to zero as the oxide layer thickness approaches  $\sim 240$  nm. Below a thickness of  $\sim 240$  nm this part of the oxide experiences a tensile force but is it below the tensile force required to fracture the oxide. As indicated in Section 3.1 there is considerable uncertainty in the tensile yield point of the oxide and this work has concluded that it is -105 MPa (assuming no grain effects) and -1.1 GPa (assuming grain size effects). If the oxide thickness is reduced further the tensile stress experienced by the oxide increases until it reaches a yield point. For these oxide thicknesses, formation of this size sub-surface precipitate will cause the oxide to fail in tension.

These results suggest the thickness of the oxide-layer will have a significant influence on the transformation of sub-surface precipitates into growth centres. Thicker oxides require the sub-surface precipitate to grow to a significant larger size before fracture occurs. This is in agreement with experimental work as shown in Section 1.5: experiments that use different preparation methods, and lengths of time in an oxidation environment will produce different thickness of oxide-layers. This change in oxide thickness as well as other factors will significantly effect the likelihood of sites to transform into growth centres.

As mentioned before the oxide stress in the previous model was kept constant (3 GPa). This will not always be the case as the stress within that oxide will vary if stress relieving mechanisms occur (temperature, cracking).

Therefore a model was developed which kept the oxide layer the same thickness (64 nm) but varied the level of stress within the oxide to examine how a stress relieved oxide could influence this fracture point, this is shown in Figure 75.

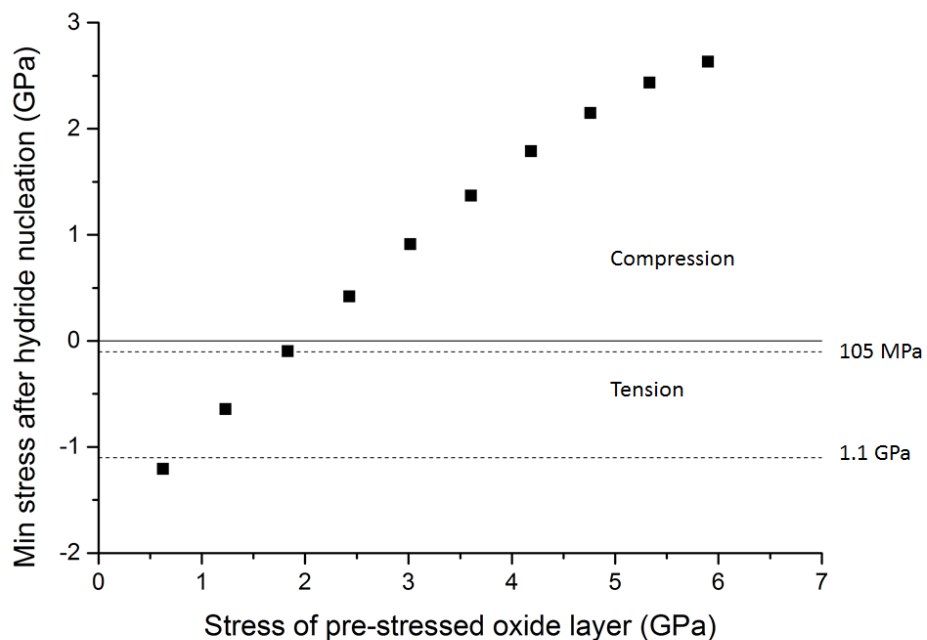


Figure 72: The minimum tensile stress within the oxide-layer for a  $0.5 \mu\text{m}$  hydride plotted against the compressive stress of the oxide for a thickness of 64 nm.

As the initial pre-stress within the oxide decreases the minimum compressive stress (most tensile) decreases. This follows roughly a linear relationship and means unsurprisingly that a less stressed hydride will increase the likelihood of fracture of the hydride. This again indicates the importance of the

experimental technique introducing different stress layers, within the oxide and at what temperature the hydrides are produced experimentally.

#### 6.4 Influence of grain orientation on the stress profile of a hydride precipitate

The orientation of the grain to the surface could have a significant effect on the stress profile of the hydride. Carpenter [102] has shown, through orientation imaging microscopy, that the average grain size of wrought  $\alpha$ -U is between  $10 \mu\text{m}$  and  $40 \mu\text{m}$ . Furthermore there is a significant variation of grain orientations, but with a preferential orientation towards [001] (used in previous simulations), his image is shown in Figure 73.

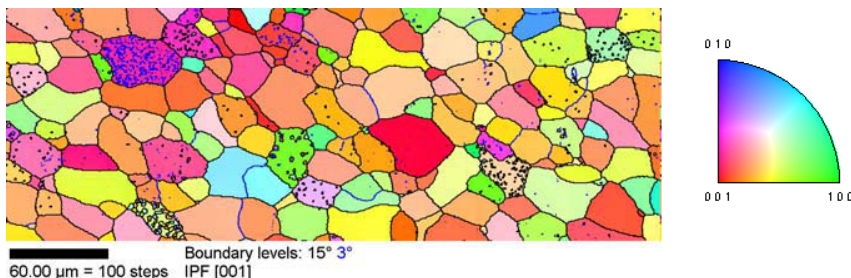


Figure 73: An inverse pole map of  $\alpha$ -U grain orientation with preferential [001] orientation [102]

A simulation was run which varied the orientation of the metal surrounding the hydride. This meant that with COMSOL the anisotropy of the uranium metal was rotated in the material frame and allowed the simulation to be varied for different planes on the surface. The orientations used in these simulations were then set to create the [100] and [010] on the surface. The

rotation was made when the hydride site was  $0.5 \mu\text{m}$  from the surface and the hydride was spherical with a diameter of  $0.5 \mu\text{m}$ .

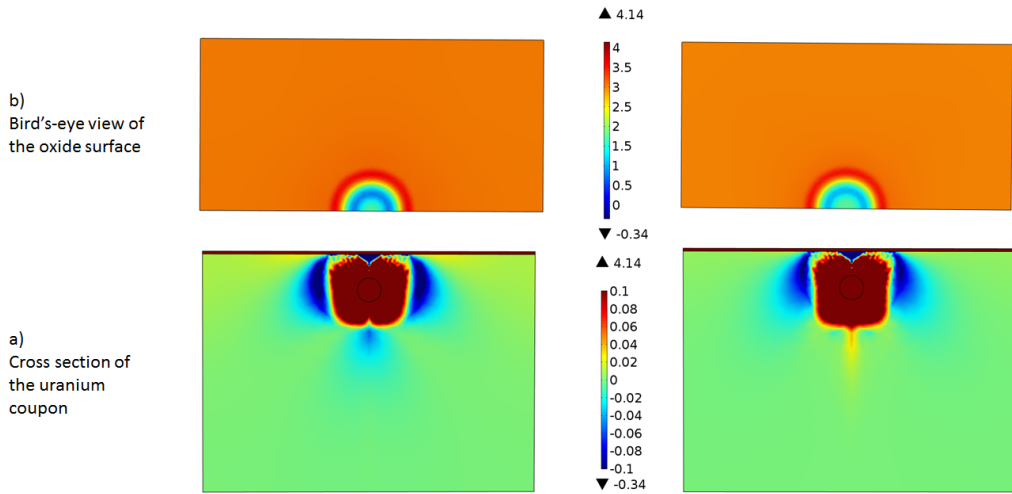


Figure 74: Image on the left the [010]  $\alpha$ -U grain orientation and on the right is the [100] orientation a) Cross section of the whole model; b) bird's-eye view of the oxide surface.

For the [010] the pressure directly surrounding the hydride and in the x directions were identical for all three grain orientations. The oxide stress causes the stress pattern on the oxide surface to be concentric circles. This stress pattern which was also identical in all three grain orientations. There is a clear difference in the model in the z direction away from the surface. This is that on the [010] plane there is a tensile region beneath the hydride (similar to the [001]), and could aid the formation of streamers. Whilst in the [100] plane the stress beneath the hydride is compressive, which would most likely limit the formation of streamers. This could mean that streamers do not

always form underneath the hydride and their formation could be dependent on the grain orientation of the metal.

The deformation of the surface and the total energy of the system for the three different grains is shown in Table 9.

Table 9: Deformation and total energy for different grain orientations

Grain orientation	Protrusion height (nm)	Total energy ( $J \times 10^{-10}$ )
[100]	30.5	2.433
[010]	32	2.423
[001]	31.5	2.420

The three different orientations of the grains have very similar deformation of the oxide surface with a maximum difference of 3% between the [100] and [001] planes. Whilst the total energy of the system is again similar with a maximum difference of 0.55% for the same planes. This difference will have a limited influence on the formation of  $UH_3$  within different orientation of grains.

## 6.5 Work Hardened Layer

When metal is polished a work hardened layer is formed. This worked hardened layer has been found to be of dependent both on the size of the grit and the pressure applied [108]. In the case of the experimental work carried out at AWE this could equate to a hardened surface layer  $\sim 0.25\mu m$ . When the uranium is hardened the yield stress of the hardened layer is increased, the increase is determined by the amount of plastic strain that occurred during this polishing operation. This change is dependent on the dislocation density so the increase in the yield stress is hard to quantify an estimate

of the increase in yield stress is  $\sim 5\%$  [109]. Therefore a sensitivity analysis was carried out which examined an extreme change in yield stress of up to 15%. An additional complication not simulated here is the change in residual sub-surface metal stress also brought about by polishing [108].

Two simulations were run with a work hardened layer thickness of  $0.25 \mu\text{m}$  (representing the size of the grit) and  $1.25 \mu\text{m}$ , with a  $0.5 \mu\text{m}$  spherical hydride at a depth of  $0.5 \mu\text{m}$ . The results of the total energy is plotted against the % increase in the yield stress.

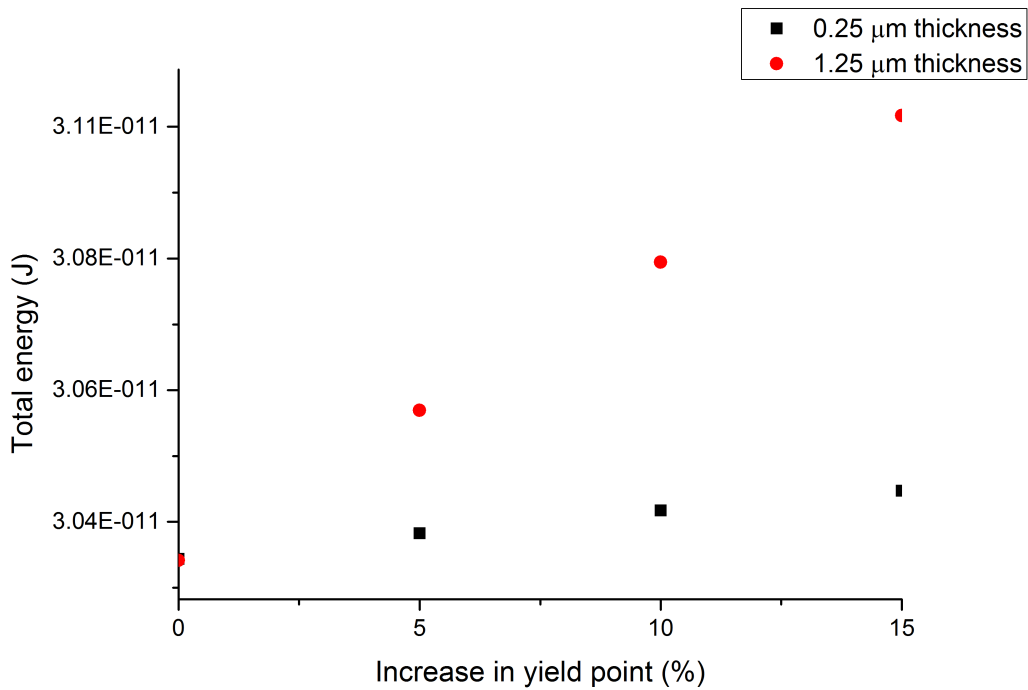


Figure 75: The total energy of the system was plotted against the % change in the yield stress on the work hardened layer.

In Figure 75 as the work hardened layer becomes thicker the energy required to form the same sized hydride increases. For a 10% increase in yield stress the extra energy required is 0.28% for 0.25  $\mu\text{m}$  thickness and 1.72% for a 1.25  $\mu\text{m}$  thickness.

These results indicate that the thicker the work-hardened layer the more energy that is required to form hydrides. This is in agreement with Scott et al [44] who found that for two samples, one containing a work hardened layer (10  $\mu\text{m}$  thickness) and the other not, the work-hardened sample exhibited a smaller number of  $\text{UH}_3$  precipitates in comparison to the non-hardened sample.

## 6.6 Summary

Many factors influence the transition from sub-surface precipitates to growth centres: size of the precipitate, plasticity of the uranium, oxide thickness, degree of pre-stressed oxide, grain orientation, and work hardened layer. In this section these effects were investigated and the results are detailed below:

- The plasticity of a the hydride is limited to around the precipitate and extends towards the surface.
- The plasticity of the hydride exists even with a 0.08  $\mu\text{m}$  diameter precipitate. As the precipitate increases in diameter the amount of plastic work per  $\mu\text{m}$  of  $\text{UH}_3$  formed decreases.
- The thickness of the oxide-layer will have a significant influence on the transformation of sub-surface precipitates into growth centres. Thicker

oxides require the sub-surface precipitate to grow to a significant larger size before fracture occurs.

- A less stressed hydride will increase the likelihood of fracture of the hydride. This indicates the importance of the experimental technique introducing different stress layers, within the oxide and at what temperature the hydrides are produced experimentally.
- The three different grain orientations have the same tensile and compressive regions. However, there will be an energy penalty in the formation of precipitates within some orientations.
- The thicker the work-hardened layer the more energy that is required to form hydrides.

All of these factors together add further to the experimental evidence in Section 1 that the formation of sub-surface  $\text{UH}_3$  is an extremely complex process which has many factors influencing their development, and there is no dominating process.

## 7 Conclusions

This section summarises the main conclusions from the work which has been described in this thesis, this includes the results from the nano-indentation experiment and the COMSOL simulations. Each of the three aims discussed in Section 1 are described in more detail.

### 7.1 Nano-indentation

This innovative technique of constrained hydride growth within tin has enabled the measurement of the reduced modulus of  $\beta$ -UH<sub>3</sub> using nano-indentation for the first time. From these measurements it was possible to calculate the bulk modulus to be  $180 \pm 20$  GPa.

### 7.2 Stresses induced by the nucleation of UH<sub>3</sub>

A UH<sub>3</sub> precipitate has been modelled at six different depths from 0  $\mu\text{m}$  to 2  $\mu\text{m}$  and the stress and deformation were calculated on the oxide surface and around the precipitate. On the oxide surface there is a central region surrounded by a ring of high compressive stress. This central region is either under less compressive or increased tensile stress with the stress tending to tensile stress when the precipitate is closer to the surface. Outside of the ring of increased compressive stress, the stress reduces when moving away from the UH<sub>3</sub> precipitate and approaches the normal compressive stress in the oxide.

- Nucleation closer to the surface is more energetically favourable (by up

to 13%). This agrees with the experimental work which has found that the hydride forms at or close to the oxide surface.

- As the hydride is placed at a greater depth, the effect on the surface protrusion is to make the deformation peak lower and flatter.
- In anisotropic matrices streamers might be explained by the tensile region found beneath the precipitate.
- If the compressive region just below the U/UO<sub>2</sub> interface and to the side of the hydride is of a sufficient size and intensity it could limit other precipitate nucleation. If such a relationship were true, there may be a reduced probability of hydride sites nucleating close to one another (2 μm by this simulation result).
- This work proposes that sub-surface precipitates may develop by preferentially transforming tensile regions of the metal. This would produce precipitates of a horizontal ellipsoid shape which is in agreement with experimental observations.

### **7.3 Stress induced by different shaped hydrides and multiple hydride precipitates**

The shape of the precipitate was varied from vertical ellipsoid to horizontal ellipsoid to examine the influence this would have on the stress profile surrounding the precipitate, the total energy of the system and the deformation of the surface

- The stress profile of the vertical ellipsoidal and the horizontal ellipsoidal had similarities, however, the influence of the shape on the metal stress profile just beneath the surface and oxide layer were different. The total energy of the system suggested that the vertical ellipsoidal shapes were preferential nucleation shapes for the precipitates in an elasto-plastic system. Since these shapes are not seen experimentally [44] it could suggest that the growth of the  $\text{UH}_3$  precipitates is a contributing factor for their horizontal ellipsoidal shape.
- When the two precipitates are at a distance of greater than  $1.5 \mu\text{m}$  apart there is a compressive region near the surface between the hydrides which could slow down the diffusion of hydrogen into the bulk and limit their coalescence. However once that initial barrier has been breached (less than  $1.5 \mu\text{m}$ ) the further growth and amalgamation of the hydrides is encouraged due to a tensile region (instead of compressive) and the energy benefit.
- Finally the AFM data on the surface suggested that whilst multiple hydride sites beneath the surface might alter the surface protrusion such that if they are closer together  $\sim 3 \mu\text{m}$  in the bulk only one surface protrusion will be shown.

#### **7.4 Factors that could influence the hydride stress profile and the transformation into growth centres**

Many factors could influence the transition from sub-surface precipitates to growth centres: size of the precipitate, plasticity of the uranium, oxide thick-

ness, degree of pre-stressed oxide, grain orientation, and work hardened layer.

- The plastic deformation in the metal is greatest at the  $\text{UH}_3\text{-U}$  interface and extends towards the surface.
- Plastic deformation in the metal is apparent even with a  $0.08 \mu\text{m}$  diameter precipitate. As the precipitate increases in diameter the amount of plastic work per  $\mu\text{m}$  of  $\text{UH}_3$  formed decreases.
- The thickness of the oxide-layer will have a significant influence on the transformation of sub-surface precipitates into growth centres. Thicker oxides require the sub-surface precipitate to grow to a significant larger size before fracture occurs.
- A less compressively stressed oxide will increase the likelihood of fracture of the oxide. This indicates the importance of the experimental procedures introducing different stress layers in the metal. Additionally this balance of factors may be different under different experimental conditions (for example temperature).
- The three different grain orientations have very similar tensile and compressive regions. However, there is a relative energy penalty in the formation of precipitates within some orientations.
- The thicker the work-hardened layer the more energy that is required to form hydrides.

This work represents a substantial increase in knowledge about the stress mechanisms in a growing uranium hydride precipitate and the influence this could have on the hydrides future development.

All of these factors together add further to the experimental evidence in Section 1 that the formation of sub-surface UH<sub>3</sub> is an extremely complex process which has many factors influencing their development, and there is no dominating process.

## 8 Further work recommendations

There are some areas that could be developed in this work to strengthen the conclusions that have been made and these are described below.

### 8.1 Experimental

#### 8.1.1 Further nano-indentation studies on $\beta\text{-UH}_3$

Further nano-indentation experiments could be carried out using a spherical diamond tip. This would enable the experimental work to be paired with a simulation created at Cambridge University to identify more material properties for  $\beta\text{UH}_3$ . This pairing would be done by using a set routine of indents which could be directly related to a simulations, and this would allow the investigation of further material properties of  $\text{UH}_3$

#### 8.1.2 Flexure bending experiment $\text{UO}_2$

As discussed in Section 3 no flexure bending experiments were found for  $\text{UO}_2$ . This meant the accuracy of the anisotropic strain matrix within the oxide over-layer could not be fully determined and data by Chernia [77] was used in the model. Therefore it is proposed that a flexure bending experiment is carried out on a thin strip of uranium using a similar technique to Weirick/Parise to measure the bending stress due to  $\text{UO}_2$  formation.

### **8.1.3 Other material properties**

Develop further understanding on some of the parameters that are of more use to this work. Such as the tensile yield strength of the oxide and how it might vary with grain size. Furthermore, how the yield stress changes with stoichiometry and for different growth conditions.

## **8.2 Modelling**

### **8.2.1 Undulations in the metal/oxide interface**

As mentioned before in Section 1 the surface roughness of the uranium sample could have a significant effect on the stressed regions. The previous modelling work only found a variation as much as 1 GPa. Undulations have recently been modelled on  $\text{ZrO}_2$  by Platt [110], and his method could be developed for this work. Examining the possibility that stress is a cause for preferential formation at polishing sites would be valuable.

### **8.2.2 Diffusion**

Although it was beyond the scope of the work to include diffusion within the model it would be possible to examine the diffusion of the hydrogen through the uranium and oxide to examine the possibility of its effect on the hydride's growth. Using COMSOL multi physics it could be possible to couple these two processes together.

### **8.2.3 Inclusions and Grain boundaries**

As described in Section 1.5 there has been lots of experimental work on the influence of inclusions and grain boundaries on the hydride formation. This model could be extended to examine if as mentioned by Arkush [49] that stress is a cause for the formation of hydride at inclusions and if grain boundaries could influence the precipitates development.

### **8.2.4 Work hardened layer**

This work has only briefly modelled the hardening of the uranium surface. However, as mentioned before (Section 6) the work hardened layer also has a residual stress effect. This effect could be important to the hydrides development and therefore a detailed model should be run to understand this effect.

## References

- [1] S.B. Lyon. 3.19 - corrosion of uranium and its alloys\*. In Bob CottisMichael GrahamRobert LindsayStuart LyonTony Richardson-David ScantleburyHoward Stott, editor, *Shreir's Corrosion*, pages 2181 – 2191. Elsevier, Oxford, 2010.
- [2] P Chiotti. The HU system (hydrogen-uranium). *Journal of Phase Equilibria*, 1(2):99–106, 1980.
- [3] G Louis Powell. Uranium corrosion near ambient temperature. In *Uranium Processing and Properties*, pages 189–206. Springer, 2013.
- [4] W Bartscher. Actinides-hydrogen. *Solid State Phenomena*, 49:159–238, 1996.
- [5] M Brill, J Bloch, and MH Mintz. Experimental verification of the formal nucleation and growth rate equations—initial  $\text{UH}_3$  development on uranium surface. *Journal of alloys and compounds*, 266(1):180–185, 1998.
- [6] C. J. Beevers and G. T. Newman. Hydrogen embrittlement in uranium. *Journal of Nuclear Materials*, 23(1):10–18, 1967.
- [7] Mrs P. Adamson, S. Orman, and G. Picton. The effects of hydrogen on the tensile properties of uranium when tested in different environments. *Journal of Nuclear Materials*, 33(2):215–224, 1969.

- [8] NJ Harker, TB Scott, CP Jones, JR Petherbridge, and J Glascott. Altering the hydriding behaviour of uranium metal by induced oxide penetration around carbo-nitride inclusions. *Solid State Ionics*, 241:46–52, 2013.
- [9] J. F. Bingert, R. J. Hanrahan Jr, R. D. Field, and P. O. Dickerson. Microtextural investigation of hydrided  $\alpha$ -uranium. *Journal of Alloys and Compounds*, 365(12):138–148, 2003.
- [10] Christopher P Jones, Thomas B Scott, James R Petherbridge, and Joseph Glascott. A surface science study of the initial stages of hydrogen corrosion on uranium metal and the role played by grain microstructure. *Solid State Ionics*, 231:81–86, 2013.
- [11] R Arkush, M Brill, S Zalkind, MH Mintz, and N Shamir. The effect of  $N_2^+$  and  $C^+$  implantation on uranium hydride nucleation and growth kinetics. *Journal of alloys and compounds*, 330:472–475, 2002.
- [12] J. Bloch, F. Simca, M. Kroup, A. Stern, D. Shmariahu, M. H. Mintz, and Z. Hadari. The initial kinetics of uranium hydride formation studied by a hot-stage microscope technique. *Journal of the Less Common Metals*, 103(1):163–171, 1984.
- [13] G. M. Benamar, D. Schweke, G. Kimmel, and M. H. Mintz. Preferred hydride growth orientations on oxide-coated gadolinium surfaces. *Journal of Alloys and Compounds*, 520(0):98–104, 2012.

- [14] Y. Greenbaum, D. Barlam, M. H. Mintz, and R. Z. Shneck. The strain energy and shape evolution of hydrides precipitated at free surfaces of metals. *Journal of Alloys and Compounds*, 452(2):325–335, 2008.
- [15] Y Greenbaum, D Barlam, MH Mintz, and RZ Shneck. Elastic fields generated by a semi-spherical hydride particle on a free surface of a metal and their effect on its growth. *Journal of Alloys and Compounds*, 509(9):4025–4034, 2011.
- [16] H.C. Chu, S.K. Wu, K.F. Chien, and R.C. Kuo. Effect of radial hydrides on the axial and hoop mechanical properties of zircaloy-4 cladding. *Journal of Nuclear Materials*, 362(1):93 – 103, 2007.
- [17] J.V. Cathcart, R.E. Pawel, and G.F. Petersen. The oxidation properties of U-16.6 at. % Nb-5.6 at.% Zr and U-21 at.% Nb\*. *Oxidation of Metals*, 3(6):497–521, 1971.
- [18] Arie Bussiba, Henry Alush, and Yosef Katz. Corrosion/deformation interactions in uranium/water systems. 46(12):244–251, 1997.
- [19] R.W. Rice. The compressive strength of ceramics. In WurthW. Kriegel and III Palmour, Hayne, editors, *Ceramics in Severe Environments*, volume 5 of *Materials Science Research*, pages 195–229. Springer US, 1971.
- [20] Z Chernia, Y Ben-Eliyahu, G Kimmel, G Braun, and J Sariel. The initial stage of uranium oxidation: Mechanism of  $\text{UO}_2$  scale formation in the presence of a native lateral stress field. *The Journal of Physical Chemistry B*, 110(46):23041–23051, 2006.

- [21] RF Canon, JTA Roberts, and RJ Beals. Deformation of  $\text{UO}_2$  at high temperatures. *Journal of the American Ceramic Society*, 54(2):105–112, 1971.
- [22] AG Evans and RW Davidge. The strength and fracture of stoichiometric polycrystalline  $\text{UO}_2$ . *Journal of Nuclear Materials*, 33(3):249–260, 1969.
- [23] FP Knudsen, HS Parker, and MD Burdick. Flexural strength of specimens prepared from several uranium dioxide powders; its dependence on porosity and grain size and the influence of additions of titania. *Journal of the American Ceramic Society*, 43(12):641–647, 1960.
- [24] Joseph Bloch and Moshe H Mintz. Kinetics and mechanisms of metal hydrides formationa review. *Journal of alloys and compounds*, 253:529–541, 1997.
- [25] Marko Knezevic, Rodney J. McCabe, Carlos N. Tom, Ricardo A. Lebensohn, Shuh Rong Chen, Carl M. Cady, George T. Gray III, and Bogdan Mihaila. Modeling mechanical response and texture evolution of  $\alpha$ -uranium as a function of strain rate and temperature using polycrystal plasticity. *International Journal of Plasticity*, 43(0):70 – 84, 2013.
- [26] Afiya Chohollo. A literature review and statistical investigation of early hydride nucleation sites on depleted uranium. In *MRS Proceedings Spring 2012*. University of Manchester.

- [27] DA Carpenter, JL Pugh, and DF Teter. Control of grain boundaries in orthorhombic  $\alpha$ -uranium. *Microscopy and Microanalysis*, 11(S02):1792–1793, 2005.
- [28] Nuclear Decommissioning Authority. The ndas research and development strategy to underpin geological disposal on the united kingdoms higher activity radioactive wastes. Technical report, NDA Report NDA/RWMD/011-Issue 1, 2009.
- [29] Ingmar Grenthe, Hans Wanner, Isabelle Forest, et al. Chemical thermodynamics of uranium. 1992.
- [30] Calvin H Delegard and Andrew J Schmidt. *Uranium metal reaction behavior in water, sludge, and grout matrices*. Pacific Northwest National Laboratory, 2008.
- [31] F Le Guyadec, X Génin, JP Bayle, O Dugne, A Duhart-Barone, and C Ablitzer. Pyrophoric behaviour of uranium hydride and uranium powders. *Journal of Nuclear Materials*, 396(2):294–302, 2010.
- [32] CA Stitt, M Hart, NJ Harker, KR Hallam, J MacFarlane, A Banos, C Paraskevoulakos, E Butcher, C Padovani, and TB Scott. Nuclear waste viewed in a new light; a synchrotron study of uranium encapsulated in grout. *Journal of hazardous materials*, 285:221–227, 2015.
- [33] Jonathan S Morrell and Mark J Jackson. *Uranium Processing and Properties*. Springer, 2013.

- [34] Joseph E Burke and Cyril Stanley Smith. The formation of uranium hydride1. *Journal of the American Chemical Society*, 69(10):2500–2502, 1947.
- [35] B Abraham and H Flotow. The heats of formation of uranium hydride, uranium deuteride and uranium tritide at 25 °c. *Journal of the American Chemical Society*, 77(6):1446–1448, 1955.
- [36] Christopher D. Taylor, Turab Lookman, and R. Scott Lillard. Ab initio calculations of the uranium-hydrogen system: Thermodynamics, hydrogen saturation of  $\alpha$ -U and phase-transformation to  $\text{UH}_3$ . *Acta Materialia*, 58(3):1045–1055, 2010.
- [37] J. B. Condon. Alternative model for nonstoichiometry in uranium hydride. *Union Carbide Corporation*, pages 42–48, 1974.
- [38] C. Hampel. *Rare Metals Handbook*. Reinhold, London, 1961.
- [39] J. B. Wachtman Jr, M. L. Wheat, H. J. Anderson, and J. L. Bates. Elastic constants of single crystal  $\text{UO}_2$  at 25 °c. *Journal of Nuclear Materials*, 16(1):39–41, 1965.
- [40] I. Halevy, S. Salhov, S. Zalkind, M. Brill, and I. Yaar. High pressure study of  $\beta$ - $\text{UH}_3$  crystallographic and electronic structure. *Journal of Alloys and Compounds*, 370(12):59–64, 2004.
- [41] A. Padel and Ch De Novion. Constantes elastiques des carbures, nitrides et oxydes d'uranium et de plutonium. *Journal of Nuclear Materials*, 33(1):40–51, 1969.

- [42] R. Nicholas. Uranium and its alloys. *Nuclear Engineering*, 2(18):355–365, 1957.
- [43] Marlowe M.O. High temperature isothermal elastic moduli of UO<sub>2</sub>. *Journal of Nuclear Materials*, 33(2):242–244, 1969.
- [44] Yujuan Zhang, Baotian Wang, Yong Lu, Yu Yang, and Ping Zhang. Electronic, mechanical and thermodynamic properties of  $\alpha$  - UH<sub>3</sub>: A comparative study by using the LDA and LDA+U approaches. *Journal of Nuclear Materials*, 430(13):137 – 141, 2012.
- [45] J. Gittus. *Metallurgy of the Rarer Metals:Uranium*. Butterworths, London, 1963.
- [46] I. J. Fritz. Elastic properties of UO<sub>2</sub> at high pressure. *Journal of Applied Physics*, 47(10):4353–4358, 1976. Cited By (since 1996): 12 Export Date: 20 February 2012 Source: Scopus.
- [47] A Holden. *Physical Metallurgy of Uranium*. Addison-Wesley, Reading Massachusetts, 1958.
- [48] Christopher D Taylor and R Scott Lillard. Ab-initio calculations of the hydrogen–uranium system: Surface phenomena, absorption, transport and trapping. *Acta Materialia*, 57(16):4707–4715, 2009.
- [49] Kazuhiro Yamada, Shinsuke Yamanaka, Takashi Nakagawa, Masayoshi Uno, and Masahiro Katsura. Study of the thermodynamic properties of (U, Ce)O<sub>2</sub>. *Journal of Nuclear Materials*, 247(0):289–292, 1997.

- [50] Francis A Shunk, Max Hansen, and Kurt Anderko. *Constitution of binary alloys*. Number 2. McGraw-Hill, 1969.
- [51] Marko Knezevic, Laurent Capolungo, Carlos N Tomé, Ricardo A Lebensohn, David J Alexander, Bogdan Mihaila, and Rodney J McCabe. Anisotropic stress-strain response and microstructure evolution of textured  $\alpha$ -uranium. *Acta Materialia*, 60(2):702–715, 2012.
- [52] Toshimichi Tachibana, Hirotaka Furuya, and Masumichi Koizumi. Dependence on strain rate and temperature shown by yield stress of uranium dioxide. *Journal of Nuclear Science and Technology*, 13(9):497–502, 1976.
- [53] G. Dolling, R. A. Cowley, and A. D. B. Woods. The crystal dynamics of uranium dioxide. *Canadian Journal of Physics*, 43(8):1397–1413, 1965.
- [54] David F Teter, Robert J Hanrahan, and Christopher J Wetteland. Uranium hydride nucleation kinetics: effects of oxide thickness and vacuum outgassing. Technical report, Los Alamos National Lab., NM (US), 2001.
- [55] R. Harker. The influence of oxide thickness on the early stages of the massive uranium-hydrogen reaction. *Journal of Alloys and Compounds*, (426):106–117, 2006.
- [56] LW Owen and RA Scudamore. A microscope study of the initiation of the hydrogen-uranium reaction. *Corrosion Science*, 6(11):461–468, 1966.

- [57] Y. Ben-Eliyahu, M. Brill, and M. H. Mintz. Hydride nucleation and formation of hydride growth centers on oxidized metallic surfaces—kinetic theory. *The Journal of Chemical Physics*, 111(13):6053–6060, 1999.
- [58] T. B. Scott, G. C. Allen, I. Findlay, and J. Glascott. UD<sub>3</sub> formation on uranium: evidence for grain boundary precipitation. *Philosophical Magazine*, 87(2):177–187, 2006.
- [59] A Loui. The hydrogen corrosion of uranium: Identification of underlying causes and proposed mitigation strategies. *Lawrence Livermore National Lab# LLNL-TR-607653, Livermore*, 2012.
- [60] ME Kartal, FPE Dunne, and AJ Wilkinson. Determination of the complete microscale residual stress tensor at a subsurface carbide particle in a single-crystal superalloy from free-surface ebsd. *Acta Materialia*, 60(13):5300–5310, 2012.
- [61] R. Arkush, A. Venkert, M. Aizenshtein, S. Zalkind, D. Moreno, M. Brill, M. H. Mintz, and N. Shamir. Site related nucleation and growth of hydrides on uranium surfaces. *Journal of Alloys and Compounds*, 244(1-2):197–205, 1996.
- [62] WJ Siekhaus, PK Weber, ID Hutcheon, JEP Matzel, and W McLean. Hydrogen accumulation in and at the perimeter of U-C-N-O inclusions in uranium—a SIMS analysis. *Journal of Alloys and Compounds*, 2015.

- [63] G Benamar, D Schweke, J Bloch, T Livneh, and MH Mintz. The very initial stage of hydride formation on polycrystalline gadolinium. *Journal of Alloys and Compounds*, 477(1):188–192, 2009.
- [64] M Bloch, J. & Mintz. The kinetics of hydride formation in uranium. Technical report, 2001.
- [65] R. N. Singh, R. Kishore, T. K. Sinha, S. Banerjee, and B. P. Kashyap. Stress field estimation around a semi-constrained inclusion and its validation by interpreting hydride platelet orientation around a blister in a zr2.5nb alloy. *Materials Science and Engineering: A*, 339(12):17–28, 2003.
- [66] M.L. Vanderglas and Y.J. Kim. Stresses due to volumetric expansion of zirconium hydride inclusions. *International Journal of Pressure Vessels and Piping*, 22(3):177 – 196, 1986.
- [67] C.E. Ells. Hydride precipitates in zirconium alloys (a review). *Journal of Nuclear Materials*, 28(2):129 – 151, 1968.
- [68] Christopher A Schuh. Nanoindentation studies of materials. *Materials Today*, 9(5):32–40, 2006.
- [69] Warren C Oliver and Georges M Pharr. Measurement of hardness and elastic modulus by instrumented indentation: Advances in understanding and refinements to methodology. *Journal of materials research*, 19(01):3–20, 2004.

- [70] Ken Kurosaki, Yoshiyuki Saito, Hiroaki Muta, Masayoshi Uno, and Shinsuke Yamanaka. Nanoindentation studies of  $\text{UO}_2$  and (U, Ce)  $\text{O}_2$ . *Journal of alloys and compounds*, 381(1):240–244, 2004.
- [71] Masatoshi Kuroda, Daigo Setoyama, Masayoshi Uno, and Shinsuke Yamanaka. Nanoindentation studies of zirconium hydride. *Journal of alloys and compounds*, 368(1):211–214, 2004.
- [72] Dan Kelly. La-ur-10-00660. Technical report, LANL, 2010.
- [73] DA Treick, JH Carter, AI Snow, RR Baldwin, and AS Wilson. The uranium-tin system. Technical report, Iowa State Coll., Ames, 1945.
- [74] W. Bartscher, A. Boeuf, R. Caciuffo, J.M. Fournier, W.F. Kuhs, J. Rebizant, and F. Rustichelli. Neutron diffraction study of  $\alpha\text{-UD}_3$  and  $\alpha\text{-UH}_3$ . *Solid State Communications*, 53(4):423 – 426, 1985.
- [75] G.M. Pharr. Measurement of mechanical properties by ultra-low load indentation. *Materials Science and Engineering: A*, 253(12):151 – 159, 1998.
- [76] Chien-Jung Chiang, Steve Bull, Chris Winscom, and Andy Monkman. A nano-indentation study of the reduced elastic modulus of Alq<sub>3</sub> and NPB thin-film used in OLED devices. *Organic Electronics*, 11(3):450–455, 2010.
- [77] British Standard. Metallic materials instrumented indentation test for hardness and materials parameters part 4: Test method for metallic and non-metallic coatings.

- [78] SI Bulychev, VP Alekhin, M Kh Shorshorov, and AP Ternovskii. Mechanical properties of materials studied from kinetic diagrams of load versus depth of impression during microimpression. *Strength of Materials*, 8(9):1084–1089, 1976.
- [79] NB Pilling. R. e. bedworth. *J. Inst. Metals*, 29:577, 1923.
- [80] JR Kench and J Chamberlain. Effects of surface oxidation upon the tensile creep behavior of  $\alpha$ -uranium. *Journal of Nuclear Materials*, 28(1):61–72, 1968.
- [81] Yong-Soo Kim, Yong-Hwan Jeong, and Jeong-Nam Jang. Stress measurements during thin film zirconium oxide growth. *Journal of Nuclear Materials*, 412(2):217–220, 2011.
- [82] C. A. Colmenares. Oxidation mechanisms and catalytic properties of the actinides. *Progress in Solid State Chemistry*, 15(4):257–364, 1984.
- [83] Kenneth C Radford and GR Terwilliger. Compressive deformation of polycrystalline  $\text{UO}_2$ . *Journal of the American Ceramic Society*, 58(7-8):274–278, 1975.
- [84] MS Seltzer, AH Clauer, and BA Wilcox. The influence of stoichiometry on compression creep of uranium dioxide single crystals. *Journal of Nuclear Materials*, 44(1):43–56, 1972.
- [85] M Parise, O Sicardy, and G Cailletaud. Modelling of the mechanical behavior of the metal–oxide system during Zr alloy oxidation. *Journal of nuclear materials*, 256(1):35–46, 1998.

- [86] JV Cathcart. Stress effects and the oxidation of metals. *AIME, 345 East 47 th St., New York, N. Y. 1975, 372 p*, 1975.
- [87] RE Pawel and JV Cathcart. Flexure measurements on a U-Nb-Zr alloy during oxidation and temperature cycling. *Journal of The Electrochemical Society*, 118(11):1776–1782, 1971.
- [88] M. Parsley R. Gover P. Morrall I. Khan R. M. Harker, A. H. Chohollo. Xrd, ellipsometry and raman spectroscopy examination of uranium coupons exposed to low pressures of h2 at 80c in preparation. personal communication.
- [89] James Petherbridge. personal communication.
- [90] AG Evans and JW Hutchinson. On the mechanics of delamination and spalling in compressed films. *International Journal of Solids and Structures*, 20(5):455–466, 1984.
- [91] ASTM International. Standard test method for flexural strength of advanced ceramics at ambient temperature.
- [92] DG Westlake. Precipitation strengthening in crystals of zirconium-hydrogen alloys containing oxygen as an impurity. *Acta Metallurgica*, 12(12):1373–1380, 1964.
- [93] Jerome Chevalier, Laurent Gremillard, Anil V Virkar, and David R Clarke. The tetragonal-monoclinic transformation in zirconia: Lessons learned and future trends. *Journal of the American Ceramic Society*, 92(9):1901–1920, 2009.

- [94] R Mukherjee, TA Abinandanan, and MP Gururajan. Phase field study of precipitate growth: Effect of misfit strain and interface curvature. *Acta Materialia*, 57(13):3947–3954, 2009.
- [95] A Roatta and RE Bolmaro. An eshelby inclusion-based model for the study of stresses and plastic strain localization in metal matrix composites i: General formulation and its application to round particles. *Materials Science and Engineering: A*, 229(1):182–191, 1997.
- [96] P Stähle, RN Singh, and S Banerjee. Stresses of growing precipitates with large misfit strain. In *Int. Workshop on'Hydrogen Embrittlement of Metals-HEM08 MPH*, 2008.
- [97] R. E. Rundle. The hydrogen positions in uranium hydride by neutron diffraction1. *Journal of the American Chemical Society*, 73(9):4172–4174, 1951.
- [98] RJ McCabe, L Capolungo, PE Marshall, CM Cady, and CN Tomé. Deformation of wrought uranium: Experiments and modeling. *Acta Materialia*, 58(16):5447–5459, 2010.
- [99] R Hill. *The Mathematical Theory of Plasticity, The Oxford Engineering Science Series*. Oxford, 1950.
- [100] Olek C Zienkiewicz and Robert L Taylor. *The finite element method for solid and structural mechanics*. Butterworth-heinemann, 2005.
- [101] AB Comsol. Comsol multiphysics users guide. *Version: September, 2005*.

- [102] JE Dennis Jr and HHW Mei. Two new unconstrained optimization algorithms which use function and gradient values. *Journal of Optimization Theory and Applications*, 28(4):453–482, 1979.
- [103] O. Takakuwa, M. Nishikawa, and H. Soyama. Numerical simulation of the effects of residual stress on the concentration of hydrogen around a crack tip. *Surface and Coatings Technology*, 206(1112):2892 – 2898, 2012.
- [104] H.A Wriedt and R.A Oriani. Effect of tensile and compressive elastic stress on equilibrium hydrogen solubility in a solid. *Acta Metallurgica*, 18(7):753 – 760, 1970.
- [105] Martin Brierley, John Knowles, Neil Montgomery, and Michael Preuss. Microstructure of surface cerium hydride growth sites. *Journal of Vacuum Science & Technology A*, 32(3):031402, 2014.
- [106] JK Lee, YY Earmme, HI Aaronson, and KC Russell. Plastic relaxation of the transformation strain energy of a misfitting spherical precipitate: ideal plastic behavior. *Metallurgical transactions A*, 11(11):1837–1847, 1980.
- [107] A Willets. Personal communication, 2014.
- [108] Ioan D Marinescu, Eckart Uhlmann, and Toshiro Doi. *Handbook of lapping and polishing*. CrC Press, 2006.
- [109] M Daly. Personal communication, 2014.

- [110] Philip Platt. *Mechanical Degradation in Oxides Formed on Zirconium Alloys*. PhD thesis, The University of Manchester, 2014.
- [111] Lawrence J Weirick. Oxide stress effects on the oxidation of thorium. In *Stress Effects and the Oxidation of Metals: Proceedings of the Symposium*, page 299. Metallurgical Society of AIME, 1975.
- [112] Sigfred Peterson. Properties of thorium, its alloys and its compounds. *Oak Ridge National Laboratory: Vienna*, (16), 1965.
- [113] Edward J. Goon, John T. Mason, and Jr. Thomas R. P. Gibb. X-ray powder diffraction assembly for studies at elevated temperatures and high gas pressures. *Review of Scientific Instruments*, 28(5):342–344, 1957.
- [114] M.F.M. Batcha Ghafir, M.F.A. and V.R. Raghavan. Prediction of the thermal conductivity of metal hydrides the inverse problem. *International Journal of Hydrogen Energy*, 34:7125–7130, 2009.

## 9 Appendix A

### 9.1 Materials properties sensitivity analysis

A sensitivity analysis allows the quantification of the impact a certain parameter has on the overall outcome of the models stress calculations. There are four main material properties that COMSOL can use to calculate stress results, and they come in two pairs; Poisson ratio and Youngs modulus or shear modulus and bulk modulus. Since the available data for  $\beta$ -UH<sub>3</sub> is limited and experimental and simulated data is available only for the bulk modulus this method was chosen. It was necessary to complete an analysis on bulk modulus and shear modulus for each of the materials used.

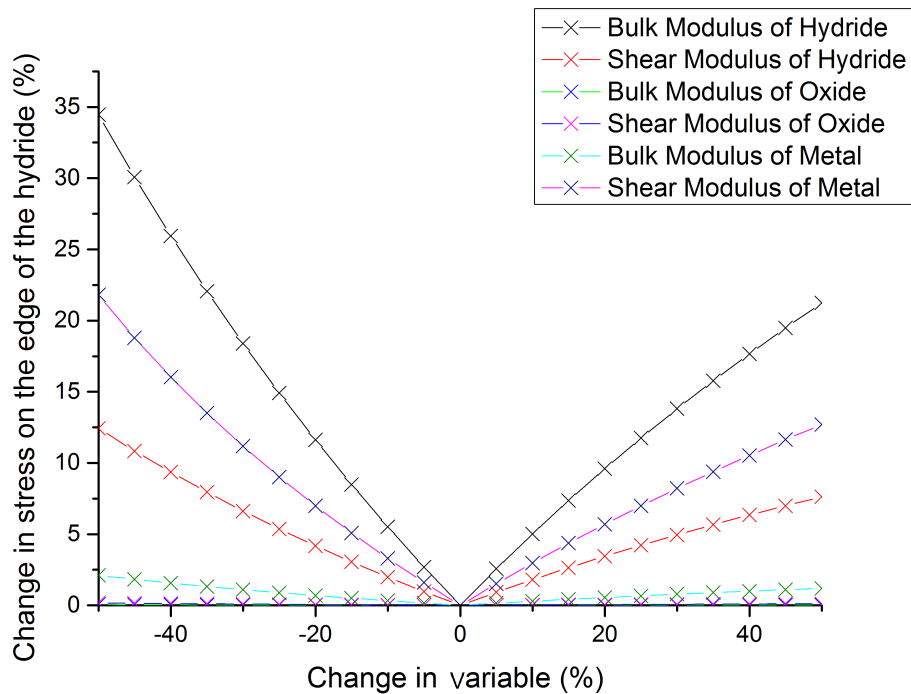


Figure 76: Sensitivity analysis of the six material properties that will be used for the simulations.

All but one of the properties was kept constant in this analysis. Then one variable was adjusted from  $\pm 50\%$  of its value. This was then repeated for each of the bulk modulus and shear modulus in the U,  $\text{UO}_2$  and  $\text{UH}_3$ . This analysis was completed through COMSOL on a uranium coupon with a nucleated precipitate at a depth of  $1 \mu\text{m}$  from the surface between the uranium and uranium dioxide.

Figure 76 shows the sensitivity analysis of the six material properties. The most important variable is the bulk modulus of the uranium hydride which varies by as much as 34% when the bulk modulus is at 50% of the average value. This is the variable with the least known accuracy with measurements between 33-144 GPa and so it would be extremely useful to have a more accurate parameter value. The shear modulus of the uranium is the next most important parameter, with a variation of 25%, however, as this value is more accurately known this does not pose a problem to modelling results. The last parameter that had a significant effect on the result was the shear modulus of the hydride with a variation of 15%. There was only one value available for this parameter so this was used.

## 10 Appendix B

### 10.1 Weirick Simulation

Finite element modelling results can be compared to experimental work to ensure they are realistic. Since there is no easily accessible uranium oxide experimental data it meant thorium oxide experiments carried out by Weirick [111] were chosen as a surrogate. Weirick grew a thorium oxide-layer on one side of a thorium coupon and calculated the thin film compressive stress by measuring the bending of the specimen. To be able to use this data as a verification method an example model of the flexure experiment had to be created in COMSOL and the strain was induced on the oxide surface.

Weirick used a block of thorium that had dimensions of (1.27, 5.09, 0.028) cm with aluminium sputtered on one side, this is shown in Figure 77.

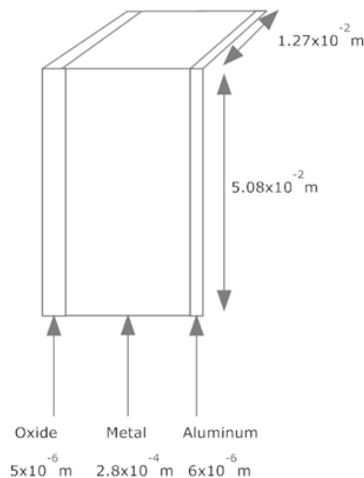


Figure 77: The experimental material dimensions used by Weirick.

The thorium specimen was placed in an oxygen filled atmosphere and the exposed thorium was oxidised. This oxidation causes the specimen to bend and the bending of the beam is then measured.

## 10.2 Simulation

The method Parise implemented to model the ZrO system was utilised and more details of this can be found in Parise's paper [82]. Three main assumptions have been made when modelling this experiment, these are as follows:

- Oxide is formed at the metal-oxide interface.
- There is a linear reaction rate.
- The only source of strain is from the volume changes during the reaction.

The Thorium data used is shown in Table 10.2.

	Youngs Modulus(GPa)	Poissons Ratio	Density(gcm <sup>-3</sup> )	Expansion on formation from metal $\frac{VolUH_3}{VolM}$
Thorium	79 [112]	0.27 [112]	11.7 [112]	n/a
Thorium Dioxide	137 [112]	0.17 [112]	10 [112]	1.166

A finite element model was created that gradually strained one side of the beam in a similar method described by Parise [82]. With the simulation results then used in the graph within Section 3.

## 11 Appendix C

### 11.1 Temperature Simulations

The hydrogen and uranium reaction within the coupon is exothermic ( $72.61 \text{ kJ mol}^{-1}$ [12] )and so will cause the temperature to increase. This temperature rise could then have many effects on the mechanisms of both the stress and structure of the materials. For example, although unlikely in this case, the metal could be subject to phase changes as a result of the temperature rise. In addition the lattice constants within the materials will be expected to increase with temperature which, in turn, could have a significant effect on the stresses within both the hydride and metal. For example Goon et al have shown the coefficient of linear thermal expansion is  $13.7 * 10^{-6} \text{ m}^2/\text{K}$  for uranium hydride [113]. This lattice expansion is the principal cause of macroscopic thermal expansion which could lead to changes in stress. Finally, hydrogen permeation itself is expected to be affected by changes in temperature as a result of modification of both diffusion and solubility.

### 11.2 Model

To consider an extreme case it was assumed that a precipitation site formed with a diameter of  $5 \mu\text{m}$  in a time of one second. Such a size and rate of growth is unlikely to exist over the conditions of interest in this study. For example, Harker and Chohollo observed a large number of precipitation sites of diameter  $0.5 \mu\text{m}$  formed over 30 seconds (  $80\text{C}$ ,  $10 \text{ mbar H}_2$  ) [15]. The amount of energy released from a  $5 \mu\text{m}$  diameter hydride precipitation site

was calculated to be  $1.72 \times 10^{-6}$  J.

With the calculation shown in below. First of all the number of moles in the hydride, N, found through Equation 24

$$N = V\rho \frac{1}{RMM} \quad (24)$$

where V is the total volume of the hydride,  $\rho$  is the density of the hydride and RMM is the realitive molecular mass. From this you can use Equation 25 to calculate the amount of energy released, Q

$$Q = N\Delta G \quad (25)$$

where  $\Delta G$  is the Gibbs formation energy.

For the simulation within COMSOL a heat source was placed throughout the hydride (to simulate the heat generated from hydride formation).

The value was calculated through the use of an Equation by Ghafir et al [114]. This Equation used previous thermal conductivity results from other hydriding metals to predict a result for uranium hydride. This calculation was based on the hydrogen pressure and hydride composition.

### 11.3 Results and discussion

The model as described ran without incident in a time of 2645 seconds. The temperature of the hydride nuclei increased from  $293.150^{\circ}\text{C}$  to  $293.159^{\circ}\text{C}$  over one seconds. The increase was linear over the 1 second. Two assumptions were made when reading the results from the model, these were. The maxi-

mum temperature of the hydride is assumed to be the centre of the hydride precipitation. This would be the case since this area would have the least opportunity to lose its energy via conduction. The maximum temperature of the metal is assumed to be at the hydride metal interface. The energy was applied by using a square wave (not typical Gaussian), the lines on the graph will be very straight. In Figure 78 below the temperature of the metal interface lags behind the hydride surface by a few milliseconds. Furthermore the maximum temperature of the hydride is above the maximum temperature of the metal. Finally after the 1250 ms point the hydride temperature (including the centre) is at an equal temperature to the metal.

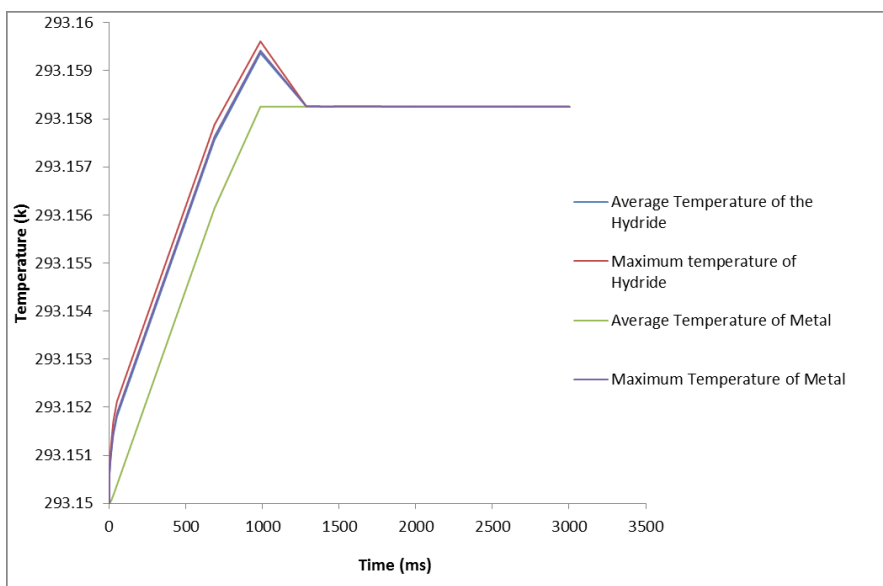


Figure 78: Temperature variation of the hydride/metal over 3 seconds

Since the maximum temperature increase seen in this example is 293.159°C for the hydride nuclei and 293.159°C for the nearby metal, it is unlikely

that the temperature produced by the nucleation (at least that produced by chemical effects) is enough to cause any significant changes to the material properties. In conclusion these temperature effects are considered irrelevant to the central models of this project.

## 12 Appendix D

### 12.1 Comparison to AFM data

To ensure that the simulations are realistic the model is compared to experimental data. Due to the lack of experimental data in this area a method has been developed that utilises Atomic Force Microscopy (AFM) data taken at AWE Aldermaston [15]. AFM measures the height of the surface and allows the estimation of the height of the hydride sites that we have chosen. A typical AFM data set which has been formatted in MATLAB graph is shown below in Figure 79:

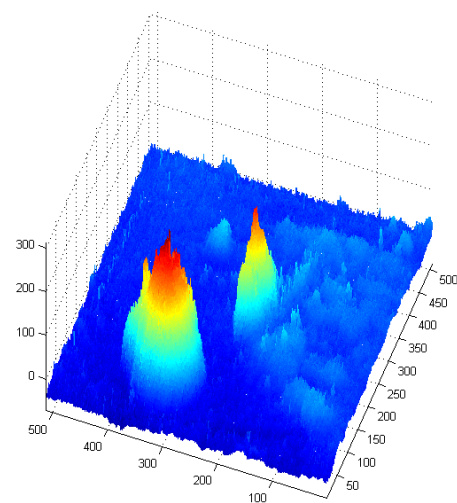


Figure 79: A mesh plot of the AFM data, two surface protrusions can be seen

The height and cross section is then measured through the centre of the protrusions through the hydride with surface protrusion from The Figure 79 having a maximum height of 250 nm and diameter of  $1.8 \mu\text{m}$ .

The size, shape, depth of the hydride and oxide thickness was varied across the results and a sensitivity analysis was completed with this data. It was found that the the depth of the hydride had the greatest effect on the height of the AFM data. Whilst the radius of the hydride effected the diameter of the surface protrusion. The thickness of the oxide had minimal effect on the height or radius of the protrusions. Finally the shape only had a significant effect on the radius of the protrusion on the surface, with more oblate hydrides having a larger influence.

A comparison between some of the experimental data and hydride sites modelled are shown in Figure 80. This shows that with this model comparable shaped surface protrusions could be created. With the shape of the hydride in the model closely following the shape of the protrusion. Therefore this gives some added confidence to the reliability of the model.

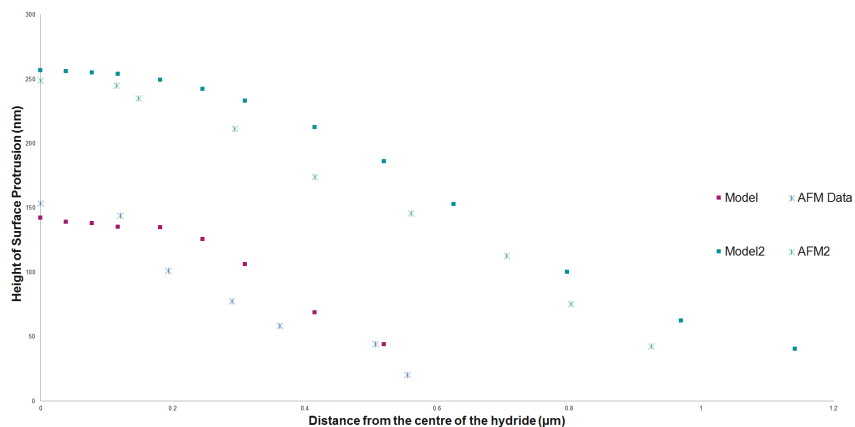


Figure 80: Comparison of the model results with experimental AFM results.